GREGG M. SINCLAIR LIBRARY
UNIVERSITY OF HAWAII

L

APPLIED SCIENTIFIC RESERACH

Section B

Volume IX Part 4/5

Appl. sci. Res. Section B, Vol. 9

SHEAR FLOW OF A CONDUCTING FLUID IN THE PRESENCE OF A MAGNETIC FIELD

by L. V. K. VISWANADHA SARMA

Indian Institute of Technology, Bombay, India

Summary

In this paper we have made a start in the study of the effect of uniform vorticity present in the free stream on the interaction of the flow and magnetic fields for the case of two-dimensional flow of an inviscid, incompressible perfectly conducting fluid. The exact non-linear equations for the stream function of the flow and the magnetic field function are obtained when the uniform applied magnetic field is parallel to the free-stream direction. These equations are linearized by assuming the perturbation from the undisturbed flow to be small. The flow past a sinusoidal wall is studied on the basis of these linearized equations. In the absence of shear the small perturbation theory shows that the flow field and magnetic field are irrotational for all values of m (the ratio of the fluid velocity to Alfvén velocity) except 1. The governing equations in the case $m = 1$ are obtained, starting from the non-linear equations. The flow past thin aerofoils can be studied on the basis of these equations. It is however observed that for a full description of the flow in this case a somewhat simplified non-linear equation (equation (5.3)) is to be solved.

§ 1. *Introduction.* We consider the steady two-dimensional rotational flow of an incompressible, inviscid, perfectly conducting fluid in the presence of a uniform magnetic field. The governing equations can be reduced to a single non-linear equation for the stream function ψ or alternatively for the ‚magnetic field function' ϕ. These equations are obtained in § 2. With the assumption of uniform flow conditions at infinity (namely, constant velocity U in the positive x-direction, constant ‚aligned' magnetic field H_0 and uniform shear) the ‚Oseen type' small perturbation flow equations are obtained in § 4. In the absence of shear, the flow field and the magnetic field governed by these small perturbation equations are irrotational (cf. Sears and Resler [1])) except when $m = 1$. (m is the ratio of the flow velocity U to the Alf'vén velocity $H_0/\sqrt{4\pi\rho}$.) In order to illustrate the effect of shear on the interaction of the flow field with the magnetic field, the flow past an infinite non-conducting sinusoidal wall is considered. It is found that the flow field and the magnetic field have a logarithmic singularity on the boundary as m approaches unity. The assumption of small disturbances thus breaks down near the boundary in this case. In view of the doubts expressed by Stewartson [2]) as regards the validity of the steady small perturbation theory, it is proposed to study the Oseen type unsteady flow past thin cylindrical obstacles. This study is deferred to a subsequent paper. In § 6 a brief discussion is given on the effect of shear when the uniform applied magnetic field is perpendicular to the undisturbed flow direction.

§ 2. *Governing equations.* Steady flow of an inviscid, incompressible conducting fluid is governed by the following equations (cf. Ref. 1)):

$$\boldsymbol{q}\cdot\nabla\boldsymbol{q} + \frac{1}{\rho}\nabla p = \frac{1}{4\pi\rho}(\boldsymbol{H}\cdot\nabla\boldsymbol{H} - \tfrac{1}{2}\nabla H^2), \tag{2.1}$$

$$\boldsymbol{q}\cdot\nabla\boldsymbol{H} - \boldsymbol{H}\cdot\nabla\boldsymbol{q} = \frac{1}{4\pi\sigma}\nabla^2\boldsymbol{H}. \tag{2.2}$$

Here $\boldsymbol{q}$ denotes the fluid velocity, $\boldsymbol{H}$ the magnetic field vector, p the pressure, ρ the density and σ the electrical conductivity of the fluid.

We consider the two-dimensional flow and introduce the flow field stream function ψ and the magnetic field function ϕ:

$$u = \frac{\partial\psi}{\partial y}, \quad v = -\frac{\partial\psi}{\partial x}, \tag{2.3}$$

$$h_x = \frac{\partial\phi}{\partial y}, \quad h_y = -\frac{\partial\phi}{\partial x}. \tag{2.4}$$

Here u, v are the velocity components and h_x, h_y are the magnetic field components along the x and y-directions. Now equations (2.1) and (2.2) take the forms

$$\frac{\partial\psi}{\partial x}\frac{\partial\Omega}{\partial y} - \frac{\partial\psi}{\partial y}\frac{\partial\Omega}{\partial x} = \frac{1}{4\pi\rho}\left(\frac{\partial\phi}{\partial x}\frac{\partial\xi}{\partial y} - \frac{\partial\phi}{\partial y}\frac{\partial\xi}{\partial x}\right) \tag{2.5}$$

and

$$\frac{\partial\psi}{\partial x}\frac{\partial\phi}{\partial y}-\frac{\partial\psi}{\partial y}\frac{\partial\phi}{\partial x}=\frac{\xi}{8\pi\sigma}, \tag{2.6}$$

where

$$\Omega=-\nabla^2\psi \text{ and } \xi=-\nabla^2\phi. \tag{2.7}$$

For a fluid of infinite conductivity (2.6) gives

$$\phi=f(\psi). \tag{2.8}$$

Equation (2.5) together with (2.8) gives

$$\frac{\partial\psi}{\partial x}\frac{\partial}{\partial y}\left(\Omega-\frac{f'(\psi)}{4\pi\rho}\xi\right)-\frac{\partial\psi}{\partial y}\frac{\partial}{\partial x}\left(\Omega-\frac{f'(\psi)}{4\pi\rho}\xi\right)=0, \tag{2.9}$$

where a dash denotes differentiation with respect to ψ. This means

$$\Omega-\frac{f'(\psi)}{4\pi\rho}\xi=g(\psi), \tag{2.10}$$

f and g denoting arbitrary functions. Eliminating ϕ from equations (2.8) and (2.10), we get

$$\left(\frac{f'^2}{4\pi\rho}-1\right)\nabla^2\psi+\frac{f'f''}{4\pi\rho}\left[\left(\frac{\partial\psi}{\partial x}\right)^2+\left(\frac{\partial\psi}{\partial y}\right)^2\right]=g(\psi). \tag{2.11}$$

We can also obtain the equation for ϕ by a similar procedure. In place of (2.8) we may now write

$$\psi=F(\phi), \tag{2.12}$$

and the equation corresponding to (2.10) is

$$F'(\phi)\,\Omega-\frac{\xi}{4\pi\rho}=G(\phi), \tag{2.13}$$

where a dash denotes differentiation with respect to ϕ, F and G being two more arbitrary functions. Elimination of ψ between (2.12) and (2.13) gives the equation for ϕ:

$$\left(\frac{1}{4\pi\rho}-F'^2\right)\nabla^2\phi-F'F''\left[\left(\frac{\partial\phi}{\partial x}\right)^2+\left(\frac{\partial\phi}{\partial y}\right)^2\right]=G(\phi). \tag{2.14}$$

§ 3. *The case of an aligned magnetic field.* We now proceed to specialize the equations (2.11) and (2.14) for the case where the undisturbed flow consists of uniform shear and a constant magnetic field H_0 parallel to the flow. If ψ_0 and ϕ_0 stand for the undisturbed values of ψ and ϕ respectively,

$$\psi_0 = Uy - \tfrac{1}{2}\omega y^2, \tag{3.1}$$

$$\phi_0 = H_0 y. \tag{3.2}$$

The forms of $f(\psi)$ and $g(\psi)$ in (2.8) and (2.10) can be now found, and (2.11) in the non-dimensional form becomes

$$(m^2 R \Psi^2 - \Psi)\, \nabla'^2 \Psi + \tfrac{1}{2}\left[\left(\frac{\partial \Psi}{\partial x'}\right)^2 + \left(\frac{\partial \Psi}{\partial y'}\right)^2\right] = 2m^2 R^2 \Psi^2, \tag{3.3}$$

where

$$x' = x/L, \quad y' = y/L,$$

$$m = U\Big/\left(\frac{H_0}{\sqrt{4\pi\rho}}\right), \quad R = \frac{\omega L}{U},$$

$$\Psi = \frac{1}{R} - \frac{2}{LU}\psi, \quad \nabla'^2 \equiv \frac{\partial^2}{\partial x'^2} + \frac{\partial^2}{\partial y'^2};$$

L being a characteristic length.

Similarly with the help of (3.1) and (3.2) the forms of $F(\phi)$ and $G(\phi)$ in (2.12) and (2.13) can be found, and (2.14) in the non-dimensional form becomes

$$\left(\Phi^2 - \frac{1}{m^2}\right) \nabla'^2 \Phi + \Phi\left[\left(\frac{\partial \Phi}{\partial x'}\right)^2 + \left(\frac{\partial \Phi}{\partial y'}\right)^2\right] = R^2 \Phi, \tag{3.4}$$

where $\Phi = 1 - (R/LH_0)\,\phi$. Equations (3.3) and (3.4) are non-linear. In the case of a strong applied magnetic field ($m \simeq 0$) these equations become linear. It is to be noted that the presence of shear makes these linear equations wave-equations (space form) which are otherwise harmonic. They are identical with those which may be obtained by ‚Stokes-type' linearization and can be used in the case of slow motion of bodies. Here not only the perturbation from the undisturbed flow but the undisturbed flow too may be assumed small. Secondly, we can adopt ‚Oseen-type' linearization for (3.3) and (3.4), in which the perturbation from the undisturbed flow only is assumed to be small. This is treated in the next section

§ 4. *Small perturbation theory.* We consider the small perturbation flow where the perturbation from the free stream values is assumed to be small. Now the linearized form of (3.3) is

$$(1 - Ry')^2[m^2(1 - Ry')^2 - 1] \nabla'^2\psi_1 - 2R(1 - Ry') \frac{\partial\psi_1}{\partial y'} - - 2R^2\psi_1 = 0, \quad (4.1)$$

where ψ_1 is the perturbation stream function. Changing the variables x', y' to X, Y by means of the substitution

$$mRx' = X, \quad m(1 - Ry') = Y,$$

(4.1) becomes

$$\nabla_1{}^2\psi_1 - \frac{2}{Y(1 - Y^2)} \frac{\partial\psi_1}{\partial Y} + \frac{2}{Y^2(1 - Y^2)} \psi_1 = 0, \qquad (4.2)$$

where $\nabla_1{}^2 \equiv \partial^2/\partial X^2 + \partial^2/\partial Y^2$. Putting $\psi_1 = Y\psi_2$, (4.2) becomes

$$\nabla_1{}^2\psi_2 - \frac{2Y}{1 - Y^2} \frac{\partial\psi_2}{\partial Y} = 0. \qquad (4.3)$$

The corresponding linearized form of (3.4) can be obtained in a similar way. It is

$$\nabla_1{}^2\phi_1 - \frac{2Y}{1 - Y^2} \frac{\partial\phi_1}{\partial Y} = 0, \qquad (4.4)$$

where ϕ_1 denotes the perturbed magnetic field function.

We note that ϕ_1 and ψ_2 satisfy the same equation; in the absence of shear, both the perturbation stream function and the perturbed magnetic field function satisfy the Laplace equation (cf. [1])). Equations (4.3) and (4.4) can be solved with appropriate boundary conditions. In order to study the effect of shear on the flow and magnetic fields qualitatively, we consider now the flow past an infinite, non-conducting sinusoidal wall.

In what follows we find it convenient to discard the non-dimensional forms of the equations. With

$$k = \omega/U, \ m = U\bigg/\left(\frac{H_0}{\sqrt{4\pi\rho}}\right), \quad \psi = m(1 - ky)\,\psi^*,$$

where ψ is the perturbed stream function, ψ^* satisfies the equation

$$\nabla^2\psi^* - \frac{2km^2(1 - ky)}{m^2(1 - ky)^2 - 1} \frac{\partial\psi^*}{\partial y} = 0. \qquad (4.5)$$

The perturbed magnetic field function ϕ satisfies the same equation. Let the contour of the insulating wall be defined by $y = \varepsilon \cos \lambda x$, where $\varepsilon\lambda$ is small. The boundary condition at the wall is taken in the usual form:

$$\left(\frac{\partial \psi}{\partial x}\right)_{(x,0)} = U\varepsilon\lambda \sin \lambda x. \tag{4.6}$$

The first-order solution for (4.5) with the boundary condition (4.6) is

$$\psi = \frac{-U\varepsilon}{\ln \dfrac{m-1}{m+1}} (1 - ky) \ln \frac{(m-1) - mky}{(m+1) - mky} e^{i\lambda(x+iy)}, \quad y > 0,$$

$$\psi = \frac{-U\varepsilon}{\ln \dfrac{m-1}{m+1}} (1 - ky) \ln \frac{(m-1) - mky}{(m+1) - mky} e^{i\lambda(x-iy)}, \quad y < 0 \tag{4.7}$$

The first-order solution for the perturbed magnetic field function ϕ may be written down, noting the fact that on the wall

$$h_y = \frac{H_0}{U} v, \tag{4.8}$$

where h_y is the y-component of the perturbed magnetic field and v is the y-component of the perturbed flow velocity. Thus we have

$$\phi = \frac{-H_0\varepsilon}{\ln \dfrac{m-1}{m+1}} \ln \frac{(m-1) - mky}{(m+1) - mky} e^{i\lambda(x+iy)}, \quad y > 0,$$

$$\phi = \frac{-H_0\varepsilon}{\ln \dfrac{m-1}{m+1}} \ln \frac{(m-1) - mky}{(m+1) - mky} e^{i\lambda(x-iy)}, \quad y < 0; \tag{4.9}$$

on the wall we have

$$\nabla^2\phi = \frac{2H_0\varepsilon km^2}{(m^2-1)} \left(\lambda + \frac{2mk}{m^2-1} \cdot \frac{1}{\ln \dfrac{m-1}{m+1}}\right) e^{i\lambda x}. \tag{4.10}$$

The pressure disturbance on the wall is found to be

$$-\rho U^2\varepsilon \left\{\lambda\left(1 - \frac{2}{m^2}\right) + k\left[1 + \frac{2m}{m^2-1} \cdot \frac{1}{\ln \dfrac{m-1}{m+1}}\right]\right\} e^{i\lambda x}. \tag{4.11}$$

From (4.7) and (4.9) it may be noted that the flow field and the magnetic field have a logarithmic singularity on the boundary as $m \to 1$. Also it appears that the effect of shear is different according as $m <$ or > 1.

§ 5. *The case* $m = 1$. Putting $m = 1$ in (3.4) and assuming that ϕ can be expanded in the form

$$\phi = \bar{\phi}_0 + R\bar{\phi}_1 + R^2\bar{\phi}_2 + \cdots. \tag{5.1}$$

for small R, we get the equation for $\bar{\phi}_0$ as

$$2\bar{\phi}_0 \nabla^2 \bar{\phi}_0 + \left[\left(\frac{\partial \bar{\phi}_0}{\partial x}\right)^2 + \left(\frac{\partial \bar{\phi}_0}{\partial y}\right)^2\right] = 1. \tag{5.2}$$

Putting $\bar{\phi}_0 = y + \phi_P$ where ϕ_P denotes the perturbed magnetic field function (now in non-dimensional form), ϕ_P satisfies the equation

$$2(y + \phi_P)\, \nabla^2 \phi_P + \left[\left(\frac{\partial \phi_P}{\partial x}\right)^2 + \left(\frac{\partial \phi_P}{\partial y}\right)^2 + 2\,\frac{\partial \phi_P}{\partial y}\right] = 0. \tag{5.3}$$

If we assume the perturbation to be small (Oseen-type linearization) and neglect the non-linear terms in (5.3), we get

$$\nabla^2 \phi_P + \frac{1}{y}\frac{\partial \phi_P}{\partial y} = 0. \tag{5.4}$$

Starting from (3.3) we obtain, by the same procedure, equations for the stream function ψ, identical with (5.1), (5.2), (5.3) and (5.4) above; the perturbed stream function ψ_P satisfies the equation

$$\nabla^2 \psi_P + \frac{1}{y}\frac{\partial \psi_P}{\partial y} = 0. \tag{5.5}$$

Thus for $m = 1$, the equations governing the rotational flow field and rotational magnetic field are (5.5) and (5.4) when the ‚Oseen-type' linearization is adopted; for other values of m, the flow field and the magnetic field are irrotational (cf. Sears and Resler [1]).

Returning to the problem of the flow past a sinusoidal wall, a formal solution of (5.4) may be written in the form

$$\begin{aligned} \phi_P &= A\, I_0(\lambda y)\, e^{i\lambda x}, \quad y < 0, \\ &= A\, K_0(\lambda y)\, e^{i\lambda x}, \quad y > 0, \end{aligned} \tag{5.6}$$

where I_0, K_0 are modified Bessel functions and A is constant. It is not possible to satisfy the conditions on the boundary with this form of the solution. Of course, the flow in the half plane bounded by the sinusoidal wall may be found on the basis of (5.4) and (5.5), and the solution satisfying all the boundary conditions can be obtained.

In a recent paper Stewartson $^{2)}$ has discussed the flow past a circular cylinder on the basis of ‚Stokes-type' linearized equations. In this case the flow field and magnetic field are found to have a logarithmic singularity at two points on the cylinder, namely $(0, \pm a)$ where a is the radius of the cylinder. Further the fluid inside the planes, which touch the cylinder and are parallel to the undisturbed magnetic field, moves with the cylinder as if solid; the fluid outside them is at rest. These features together with the remarks made above suggest that a complete solution for the problem in the case $m = 1$ is possible only on the basis of the non-linear equation (5.3). The situation is analogous to that encountered in the case of transsonic flow where the Mach number is in the neighbourhood of unity.

§ 6. *Applied magnetic field perpendicular to the undisturbed uniform flow.* We shall now obtain the ‚Oseen-type' linearized equations for the plane, steady flow in which the applied magnetic field H_0 is perpendicular to the undisturbed flow direction. Writing

$$\boldsymbol{q} = (U - \omega y + u,\ v),$$

$$\boldsymbol{H} = (h_x,\ H_0 + h_y),$$

where u, v are small compared to U, and h_x, h_y are small compared to H_0, we obtain from (2.1) and (2.2) the following linearized equations:

$$(U - \omega y)\frac{\partial u}{\partial x} - \omega v = -\frac{1}{\rho}\frac{\partial p}{\partial x} + \frac{1}{4\pi\rho} H_0\left(\frac{\partial h_x}{\partial y} - \frac{\partial h_y}{\partial x}\right), \qquad (6.1a)$$

$$(U - \omega y)\frac{\partial v}{\partial x} = -\frac{1}{\rho}\frac{\partial p}{\partial y}, \qquad (6.1b)$$

$$(U - \omega y)\frac{\partial hx}{\partial x} + \omega H_0 - H_0\frac{\partial u}{\partial y} + \omega hy = \frac{1}{4\pi\sigma}\nabla^2 h_x, \qquad (6.2a)$$

$$(U - \omega y)\frac{\partial hy}{\partial x} - H_0\frac{\partial v}{\partial y} = \frac{1}{4\pi\sigma}\nabla^2 h_y. \qquad (6.2h)$$

Putting

$$u = \frac{\partial \psi}{\partial y}, \quad v = -\frac{\partial \psi}{\partial x},$$

$$h_x = \frac{\partial \phi}{\partial y}, \quad h_y = -\frac{\partial \phi}{\partial x},$$

$$\Omega = -\nabla^2 \psi, \ \xi = -\nabla^2 \phi,$$

(6.1*a*, *b*) and (6.2*a*, *b*) become respectively

$$(U - \omega y)\frac{\partial \Omega}{\partial x} = \frac{H_0}{4\pi\rho}\frac{\partial \xi}{\partial y}, \tag{6.3}$$

$$(U - \omega y)\frac{\partial \xi}{\partial x} - H_0\frac{\partial \Omega}{\partial y} - \omega\frac{\partial h_y}{\partial y} = \frac{1}{4\pi\sigma}\nabla^2 \xi. \tag{6.4}$$

For a perfectly conducting fluid the right hand side in (6.4) is zero, and we get the following equations for Ω and ξ:

$$(1 - ky)^2\frac{\partial^2 \Omega}{\partial x^2} - \frac{1}{m^2}\frac{\partial^2 \Omega}{\partial y^2} - \frac{1}{m^2}\frac{k}{1 - ky}\frac{\partial \Omega}{\partial y} = = \frac{\omega}{H_0}\frac{1}{m^2}\left(\frac{\partial^2 h_y}{\partial y^2} + \frac{k}{1 - ky}\frac{\partial h_y}{\partial y}\right), \tag{6.5}$$

$$(1 - ky)^2\frac{\partial^2 \xi}{\partial x^2} - \frac{1}{m^2}\frac{\partial^2 \xi}{\partial y^2} - \frac{1}{m^2}\frac{k}{1 - ky}\frac{\partial \xi}{\partial y} = k(1 - ky)\frac{\partial^2 h_y}{\partial x \partial y}, \tag{6.6}$$

where

$$K = \frac{\omega}{U}, \quad m = U \Big/ \frac{H_0}{\sqrt{4\pi\rho}}.$$

Now changing the independent variable y to η by the substitution $(1 - ky)^2 = 2\eta$, equations (6.5) and (6.6) take the forms

$$m^2\frac{\partial^2 \Omega}{\partial x^2} - \frac{\partial^2 \Omega}{\partial \eta^2} = \frac{\omega}{H_0}k^2\frac{\partial^2 h_y}{\partial \eta^2}, \tag{6.7}$$

$$m^2\frac{\partial^2 \xi}{\partial x^2} - \frac{\partial^2 \xi}{\partial \eta^2} = -k^2 m^2\frac{\partial^2 hy}{\partial x \partial \eta}. \tag{6.8}$$

If ω is very small compared to H_0, the right hand side of (6.7) and (6.8) may be neglected, and the equations are then identical with the corresponding equations in the absence of shear (cf. [1])).

Received 14th January. 1961.

REFERENCES

1) Sears, W. R. and E. L. Resler, J. Fluid Mech. **5** (1959) 257.
2) Stewartson, K., J. Fluid Mech. **8** (1960) 82.

Appl. sci. Res. Section B, Vol. **9**

ON GENERALIZED INCOMPRESSIBLE COUETTE FLOW IN HYDROMAGNETICS

by J. P. AGARWAL

Department of Mathematics Indian Institute of Technology, Kharagpur, India

Summary

In this paper, the pressure-induced flow between two relatively moving plane walls has been discussed, both for non-porous and porous walls. For non-porous walls it is found that with the vanishing of the electric field ***E***, the increase in the strength of the magnetic field can cause separation near the stationary wall even when a slight adverse pressure gradient is applied. For the case of porous walls (with suction or injection) it is found that the magnetic field helps in delaying separation.

§ 1. *Introduction.* In the conventional hydrodynamics, Couette flow (both for incompressible and compressible fluids) has been the subject of many investigations. Reference can be made to Schlichting[1]), Illingworth[2]), Liepmann and Bleviss[3]). Extension to magneto-hydrodynamics of simple Couette flow when the walls are moving relative to each other, the fluid being incompressible, has been done by Lehnert[4]) and for compressible fluids by Liepmann[5]) and Bleviss[6]). However, the effect of the magnetic field on general Couette flow (which is the pressure-induced flow superposed on simple shear flow in classical hydrodynamics) does not seem to have received any attention. In this paper, we investigate such flow in the presence of a transverse magnetic field for the two cases of non-porous and porous walls respectively.

In § 2 the basic equations governing the steady flow of electrically conducting fluids are given. In § 3 we discuss the case of flow between two non-porous walls. In particular, we investigate the effect of the magnetic field on such flow in two cases: (i) when the electric field ***E*** is negligible and (ii) when ***E*** is not negligible. For case (i) it is found that with the increase in the strength of the magnetic field a slight adverse pressure-gradient can cause separation. However, when $\boldsymbol{E}$ is not negligible, separation is delayed by the presence of electromagnetic forces.

§ 4 deals with the case of flow between two porous walls. In this case the fluid velocity is shown to depend on the dimensionless suction velocity $\overline{V}_0$, the Reynolds number R, the magnetic Reynolds number R_m and the magnetic pressure number S'. Here S' is defined as the ratio (Alfvén velocity)^2/(suction velocity)^2. In order to find the effect of suction or injection on separation at the fixed wall, S' is taken to be unity. Unlike the non-magnetic case (of uniform injection by Lilley [7]) the effect of the magnetic field is to reduce the tendency of separation due to an adverse pressure-gradient. But for the case of uniform suction, a magnetic field has the effect of delaying separation.

§ 2. *Basic equations.* The steady motion of an incompressible viscous and electrically conducting fluid in the presence of a magnetic field is governed by the flolowing equations:
The Maxwell equations

$$\operatorname{curl} \boldsymbol{H} = \boldsymbol{J}, \tag{1}$$

$$\operatorname{curl} \boldsymbol{E} = 0, \tag{2}$$

$$\operatorname{div} \boldsymbol{B} = 0, \tag{3}$$

Ohm's law

$$\boldsymbol{J} = \sigma[\boldsymbol{E} + \boldsymbol{V} \times \boldsymbol{B}], \tag{4}$$

where

$$\boldsymbol{B} = \mu_m \boldsymbol{H}, \tag{5}$$

the continuity equation

$$\operatorname{div} \boldsymbol{V} = 0 \tag{6}$$

and the momentum equation

$$\rho[\boldsymbol{V}\cdot\operatorname{grad}]\, \boldsymbol{V} = -\operatorname{grad} p + \mu_v \nabla^2 \boldsymbol{V} + \boldsymbol{J} \times \boldsymbol{B}. \tag{7}$$

The various symbols used here have their usual meaning. μ_m is the magnetic permeability, σ the electrical conductivity and μ_v the viscosity of the fluid. All electromagnetic quantities are measured in the rationalized m.k.s. system.

§ 3. *Flow with non-porous walls.* The problem under consideration is shown schematically in fig. 1; B_0 is taken to be the applied magnetic field perpendicular to the plane of the walls. Assuming all the physical quantities (except pressure) to be functions of y alone and taking

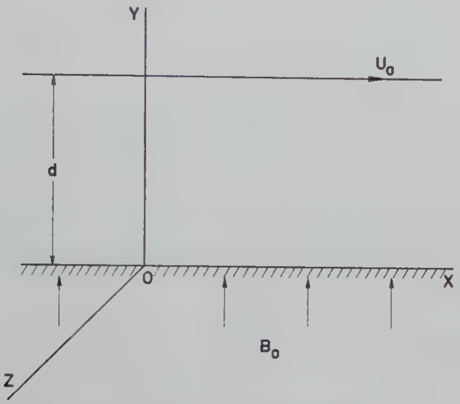

Fig. 1. Diagram showing directions of velocity U_0 and magnetic field B_0 in the coordinate system.

$$\boldsymbol{V} = u\boldsymbol{i}, \quad \boldsymbol{B} = B_x\boldsymbol{i} + B_y\boldsymbol{j}, \quad p = p(x, y),$$

we have from (1) to (5):

$$\left.\begin{aligned} B_y &= \text{constant} = B_0 \\ \boldsymbol{J} &= J_z\boldsymbol{k}, \\ J_z &= -\frac{\mathrm{d}H_x}{\mathrm{d}y} = \sigma[E_z + uB_0], \\ \boldsymbol{E} &= E_z\boldsymbol{k},\ E_z = \text{constant.} \end{aligned}\right\} \tag{8}$$

From (7)

$$-\frac{\partial p}{\partial x} + \mu_v \frac{\mathrm{d}^2 u}{\mathrm{d}y^2} - (E_z + uB_0)\,\sigma B_0 = 0, \tag{9}$$

$$-\frac{\partial p}{\partial y} - B_x \cdot \frac{\mathrm{d}H_x}{\mathrm{d}y} = 0. \tag{10}$$

Equation (10) gives $p + \frac{1}{2}\mu_m H_x{}^2 = \text{constant}$.

The fluid velocity u, determined from (9) and satisfying the boundary conditions

$$u = 0, \qquad y = 0,$$
$$u = u_0, \qquad y = d,$$

is given by

$$u = \left(U_0 - \frac{P - E_z B_0 \sigma}{k^2 \mu_v}\right) \frac{\sinh ky}{\sinh kd} - \\ - \frac{P - E_z B_0 \sigma}{k^2 \mu_v} \frac{\sinh k(d-y)}{\sinh kd} + \frac{P - E_z B_0 \sigma}{k^2 \mu_v}, \qquad (11)$$

where d, the distance between the walls, and U_0, the velocity of the moving wall will be taken as the characteristic length and velocity respectively, while

$$P \equiv -\frac{\partial p}{\partial x} = \text{const}, \quad k^2 = \frac{\sigma B_0{}^2}{\mu_v}.$$

Now writing $E_z = E_1 + E_2$, we have from (11)

$$u = \left\{ U_0 \frac{\sinh ky}{\sinh kd} + \frac{E_1 B_0 \sigma}{k^2 \mu_v} \left[\frac{\sinh ky}{\sinh kd} + \frac{\sinh k(d-y)}{\sinh kd} - 1 \right] \right\} \\ + \frac{P - E_2 B_0 \sigma}{k^2 \mu_v} \left[1 - \frac{\sinh ky}{\sinh kd} - \frac{\sinh k(d-y)}{\sinh kd} \right]$$

$$= u_1 + u_2,$$

where

$$u_1 = U_0 \frac{\sinh ky}{\sinh kd} + \frac{E_1 B_0 \sigma}{k^2 \mu_v} \left[\frac{\sinh ky}{\sinh kd} + \frac{\sinh k(d-y)}{\sinh kd} - 1 \right]$$

is the velocity for simple shear flow when $E_1 \neq 0$ and

$$u_2 = \frac{P - E_2 B_0 \sigma}{k^2 \mu_v} \left[1 - \frac{\sinh ky}{\sinh kd} - \frac{\sinh k(d-y)}{\sinh kd} \right]$$

is the velocity for flow under a constant pressure gradient P, when $E_2 \neq 0$.

We see that the flow under a constant pressure-gradient between two relatively moving walls in hydromagnetics is also the superposition of simple shear flow over pressure-induced flow (as is the case in the absence of a magnetic field).

Now from $E_z =$ constant and (11) it is evident that the velocity profile will depend on the value of E_z, the only component of the electric field, resulting in a number of solutions of the problem. Out of these various cases we have given below two. The first when E_z vanishes and the second when E_z does not vanish and is determined from the conditions imposed on the electric current or the magnetic field.

Case (i). $E_z = 0$. The physical situation that corresponds to the vanishing of the electric field has been discussed by Bleviss 6) for simple shear flow. However, in the problem under consideration if the conditions $B_x = 0$ at $y = d$ and $\mathrm{d}B_x/\mathrm{d}y = 0$ at $y = 0$ are imposed, we get $E_z = 0$ because $\mathrm{d}H_x/\mathrm{d}y = -\sigma[E_z + uB_0]$ and E_z is constant. Thus on putting $E_z = 0$ in (11) we have

$$u = U_0 \frac{\sinh ky}{\sinh kd} + \frac{P}{k^2\mu_v}\left[1 - \frac{\sinh ky}{\sinh kd} - \frac{\sinh k(d-y)}{\sinh kd}\right]. \quad (12)$$

Under the transformations

$$\bar{y} = \frac{y}{d}, \quad \bar{u} = \frac{u}{U_0}, \quad \bar{p} = p/\rho U_0^2, \quad P = \frac{\rho U_0^2}{d}\bar{P}$$

u given by (12) becomes

$$\bar{u} = \frac{\sinh M\bar{y}}{\sinh M} + \frac{\bar{P}R}{M^2}\left[1 - \frac{\sinh M\bar{y}}{\sinh M} - \frac{\sinh M(1-\bar{y})}{\sinh M}\right], \quad (12')$$

where $M = kd$ is the Hartmann number and $R = U_0 P d/\mu_v$ is the Reynolds number.

The condition for back-flow near the stationary wall is then given by $\mathrm{d}\bar{u}/\mathrm{d}\bar{y} \leqslant 0$ or

$$\bar{P}R \leqslant -M^2/(\cosh M - 1). \quad (13)$$

Now $M^2/(\cosh M - 1)$ is a monotonically decreasing function of M and has the maximum value 2 when $M \to 0$. Thus it becomes evident that an increase in the strength of the magnetic field has the effect of increasing the back-flow due to an adverse pressure gradient.

Case (ii). $E_z \neq 0$. Here we determine E_z by imposing conditions on the electric current and magnetic field and consider two cases according to the nature of the conditions.

(*a*) $\boldsymbol{E}$ is adjusted such that the total electric current

$$\int_{y=0}^{d} J_z \, dy$$

flowing between $y = 0$ and $y = d$ vanishes.

(*b*) Assuming that the magnetic field is zero on the stationary wall and increases monotonically so as to attain the maximum value at $y = d$, the conditions imposed are

$$B_x = 0 \quad \text{at} \quad y = 0; \ dB_x/dy = 0 \quad \text{at} \quad y = d.$$

Subject to the conditions of (*a*), $\bar{u}$ is given by

$$\bar{u} = \frac{\sinh M\bar{y}}{\sinh M} + \left[\tfrac{1}{2} + \frac{\bar{P}R}{2M}\,\frac{\sinh M}{\cosh M - 1}\right] \cdot \left[1 - \frac{\sinh M\bar{y}}{\sinh M} - \frac{\sinh M(1-\bar{y})}{\sinh M}\right]. \tag{14}$$

The condition for back-flow at $y = 0$ is

$$\bar{P}R \leqslant -M \coth \tfrac{1}{2}M. \tag{15}$$

$M \coth \frac{1}{2}M$ has the minimum value 2 when $M \to 0$ and increases with increasing M. Thus the increase in the strength of the magnetic field decreases the tendency of an adverse pressure-gradient to cause back-flow. Subject to the conditions of (*b*) $\bar{u}$ is given by

$$\bar{u} = \left[1 - \frac{\sinh M(1-\bar{y})}{\sinh M}\right] + \frac{\bar{P}R}{M^2}\left[1 - \frac{\sinh M\bar{y}}{\sinh M} - \frac{\sinh M(1-\bar{y})}{\sinh M}\right]. \tag{16}$$

The condition for back-flow at $y = 0$ in this case is

$$\bar{P}R \leqslant -M^2 \frac{\cosh M}{\cosh M - 1}. \tag{17}$$

The expression on the right hand side has the minimum value 2 when $M \to 0$ and increases with increasing M, leading to the same conclusions for the occurrence of back flow as in (*a*).

Hence from the results of cases (i) and (ii) we conclude that the vanishing of the electric field can bring about separation near the stationary wall when an adverse pressure gradient is applied in the presence of a magnetic field more easily than when $\boldsymbol{E}$ is non-vanishing.

Dimensionless shearing stresses on the stationary wall in the two cases are given by

(i)
$$\bar{\tau}_1 = M \operatorname{cosech} M + \frac{\bar{P}R}{M} \tanh \tfrac{1}{2}M, \tag{18}$$

(ii) (*a*)
$$\bar{\tau}_{2a} = \tfrac{1}{2}(M \coth \tfrac{1}{2}M + \bar{P}R), \tag{19}$$

(*b*)
$$\bar{\tau}_{2b} = \frac{\tanh \frac{1}{2}M}{M}\left(\bar{P}R + \frac{M^2 \cosh M}{\cosh M - 1}\right), \tag{20}$$

where $\bar{\tau} = d\bar{u}/d\bar{y}$. Tables I and II give the values of $\bar{\tau}_1$ and $\bar{\tau}_2$ for $\bar{P}R = +1, +2, -1, -2$ and for various values of M. From the tables it may be seen that while the viscous drag on the stationary wall decreases when $E_z = 0$, it increases with increasing magnetic field when $E_z \neq 0$.

TABLE I

Values of $\bar{\tau}_1$, when E_z vanishes				
$\bar{P}R$ / M	+1	+2	−1	−2
1	1.3130	1.7752	+0.3888	−0.0733
2	0.9322	1.3130	+0.1706	−0.2102
3	0.6012	0.9029	−0.0023	−0.3040
4	0.3876	0.6286	−0.0944	−0.3354

TABLE II(*a*)

Values of $\bar{\tau}_2$ when E_z does not vanish				
$\bar{P}R$ / M	+1	+2	−1	−2
1	1.5820	2.0820	0.5820	0.0820
2	1.8130	2.3130	0.8130	0.3130
3	2.1572	2.6572	1.1572	0.6574
4	2.5746	3.0746	1.5746	1.0746

TABLE II (*b*)

Values of $\bar{\tau}_2$ when E_z does not vanish				
$\bar{P}R$ / M	+1	+2	−1	−2
1	1.7752	2.2373	0.8509	0.3888
2	2.4554	2.8362	1.6938	1.3130
3	3.3166	3.6183	2.7132	2.4115
4	4.2440	4.4851	3.7620	3.5210

§ 4. *Flow with porous walls.* Here it is assumed that both walls are porous, and that uniformly distributed suction or injection is applied to the fixed surface defined by $y = 0$. Other assumptions are the same as in § 3. Let

$$\boldsymbol{V} = u\boldsymbol{i} + v\boldsymbol{j},\ \boldsymbol{B} = B_x\boldsymbol{i} + B_y\boldsymbol{j}.$$

From (1) to (6) we have

$$B_y = \text{constant} = B_0,\ v = \text{constant} = V_0.$$

V_0 is positive for injection and negative for suction.

$$\begin{aligned} \boldsymbol{J} &= J_z k, \\ J_z &= -\mathrm{d}H_x/\mathrm{d}y = \sigma[E_z + uB_0 - V_0 B_x], \\ E_z &= \text{constant}. \end{aligned} \tag{21}$$

Equation (7) gives

$$-\frac{\partial p}{\partial x} + \mu_v \frac{\mathrm{d}^2 u}{\mathrm{d}y^2} - B_0 J_z = \rho V_0 \frac{\mathrm{d}u}{\mathrm{d}y}, \tag{22}$$

$$-\frac{\partial p}{\partial y} + B_x J_z = 0. \tag{23}$$

From (21) and (23) we have

$$p + \tfrac{1}{2}\mu_m H_x^2 = \text{constant}. \tag{24}$$

Rewriting (22) we have

$$\mu_v \frac{\mathrm{d}^2 u}{\mathrm{d}y^2} - \rho V_0 \frac{\mathrm{d}u}{\mathrm{d}y} + B_0 \frac{\mathrm{d}H_x}{\mathrm{d}y} + P = 0, \tag{25}$$

where

$$P \equiv -\partial p/\partial x = \text{const}.$$

On using the transformations

$$H_x = H_0\bar{H},\ y = \mathrm{d}\bar{y},\ x = \mathrm{d}\bar{x},\ u = U_0\bar{u},\ V_0 = U_0\bar{V}_0,$$

we have from (21) and (25)

$$\frac{\mathrm{d}^3\bar{H}}{\mathrm{d}\bar{y}^3} - \bar{V}_0(R + R_m)\frac{\mathrm{d}^2\bar{H}}{\mathrm{d}\bar{y}^2} - (S - \bar{V}_0^2)\, RR_m \frac{\mathrm{d}\bar{H}}{\mathrm{d}\bar{y}} - \bar{P}RR_m = 0, \tag{26}$$

$$\bar{u} = \bar{V}_0\bar{H} - \frac{1}{R_m}\frac{\mathrm{d}\bar{H}}{\mathrm{d}\bar{y}} - \bar{E}, \tag{27}$$

where

$$R = \frac{U_0 \rho d}{\mu_v}, \quad R_m = U_0 \mu_m \sigma d, \quad S = \frac{\mu_m H_0{}^2}{\rho U_0{}^2} = \frac{a^2}{U_0{}^2}, \quad \bar{E} = \frac{E_z}{U_0 B_0},$$

$a(= \sqrt{\mu_m H_0{}^2/\rho})$ is the Alfvén velocity. Boundary conditions to be satisfied by $\bar{u}$ are

$$\bar{u} = 0 \quad \text{at} \quad \bar{y} = 0,$$
$$\bar{u} = +1 \quad \text{at} \quad \bar{y} = +1.$$

The boundary conditions to be satisfied by $\bar{H}$ will depend upon the orientation of the electric and magnetic fields. In the problem under consideration we use the condition $\bar{H} = 0$ on both the boundaries $\bar{y} = 0, 1$, which is also equivalent to the vanishing of $\bar{H}$ on either boundary together with the total electric current

$$\int_{y=0}^{d} J_z \, dy.$$

When $S' \neq 1$, $\bar{H}$ and $\bar{u}$ are given by

$$\bar{H} = A_2 (e^{\lambda_1 \bar{y}} - 1) + A_3 (e^{\lambda_2 \bar{y}} - 1) - \frac{\bar{P}}{\bar{V}_0{}^2 (S' - 1)} \bar{y}, \tag{28}$$

$$\bar{u} = \frac{1}{R_m} \Big[A_2 (R'_m - \lambda_1)(e^{\lambda_1 \bar{y}} - 1) + $$
$$+ A_3 (R'_m - \lambda_2)(e^{\lambda_2 \bar{y}} - 1) - \frac{\bar{P} R'_m}{\bar{V}_0{}^2 (S' - 1)} \bar{y} \Big], \tag{29}$$

where

$$A_2 = \frac{R_m - \dfrac{\bar{P}}{\bar{V}_0{}^2 (S' - 1)} \lambda_2}{(\lambda_1 - \lambda_2)(e^{\lambda_1} - 1)},$$

$$A_3 = - \frac{R_m - \dfrac{\bar{P}}{\bar{V}_0{}^2 (S' - 1)} \lambda_1}{(\lambda_1 - \lambda_2)(e^{\lambda_2} - 1)},$$

$$R' = R \bar{V}_0, \quad R'_m = R_m \bar{V}_0, \quad S' = S/\bar{V}_0{}^2,$$

and λ_1, λ_2 are the roots of

$$\lambda^2 - (R' + R'_m)\lambda - R' R'_m (S' - 1) = 0.$$

Separation at the fixed wall will occur when

$$(A_2\lambda_1 + A_3\lambda_2)\, R_m' - (A_2\lambda_1{}^2 + A_3\lambda_2{}^2) - \frac{\bar{P}R'_m}{\bar{V}_0{}^2(S'-1)} = 0. \tag{30}$$

when $S' = 0$, (29) and (30) reduce to

$$\bar{u} = \left(1 - \frac{\bar{P}}{\bar{V}_0}\right)\frac{(\mathrm{e}^{R'\bar{y}} - 1)}{\mathrm{e}^{R'} - 1} + \frac{\bar{P}}{\bar{V}_0}\,\bar{y} \tag{31}$$

and

$$\frac{\bar{P}}{\bar{V}_0}\,(\mathrm{e}^{R'} - 1 - R') + R = 0, \tag{32}$$

which are the results obtained by Lilley 7) in the absence of a magnetic field.

When $S' = 1$, (22) becomes

$$\frac{\mathrm{d}^3\bar{\bar{H}}}{\mathrm{d}\bar{y}^3} - \bar{V}_0(R + R_m)\,\frac{\mathrm{d}^2\bar{\bar{H}}}{\mathrm{d}\bar{y}^2} - \bar{P}RR_m = 0, \tag{33}$$

and $\bar{\bar{H}}$ and $\bar{u}$ are given by

$$\bar{\bar{H}} = A_2\bar{y} + A_3[\mathrm{e}^{(R'+R'_m)\bar{y}} - 1] - \frac{\bar{P}RR_m}{\bar{V}_0(R + R_m)}\,\frac{\bar{y}^2}{2}, \tag{34}$$

$$\bar{u} = \frac{1}{R_m}\left[A_2R_m'\bar{y} - A_3R'(\mathrm{e}^{(R'+R'_m)\bar{y}} - 1) + \frac{\bar{P}RR_m\,\bar{y}}{(R'+R_m')}\left(\frac{1 - R_m'\bar{y}}{2}\right)\right], \tag{35}$$

where

$$A_2 = \frac{\bar{P}RR_m}{R' + R'_m}\left(\frac{1}{2} - \frac{1}{R' + R'_m}\right) + \frac{R_m}{R' + R_m'},$$

$$A_3 = \frac{\dfrac{\bar{P}RR_m}{R' + R'_m} - R_m}{(R' + R_m')\,(\mathrm{e}^{R'+R_m'} - 1)}.$$

The condition for separation at the stationary wall is

$$\bar{P}R = -\frac{2(R' + R'_m)[R'(R' + R'_m) + R'_m(\mathrm{e}^{R'+R_m'} - 1)]}{(\mathrm{e}^{R'+R'_m} - 1)[R'_m(R' + R_m') + 2R'] - 2R'(R' + R'_m)}. \tag{36}$$

Tables III and IV give the values of the expression on the right-hand side of (36) when $R = 5$ and $S' = 1$ for positive and negative values of $\bar{V}_0$. Values of $\bar{P}R$ when $R_m = 0$ correspond to the case

TABLE III

Values of $\overline{P}R$ when $R = 5$ and $\overline{V}_0$ is positive

R_m / $\overline{V}_0$	0	0.1	0.3	0.5
0.1	−1.6810	−1.6819	−1.6836	−1.6853
0.3	−1.1354	−1.1437	−1.1602	−1.1765
0.5	−0.7198	−0.7433	−0.7891	−0.8334

TABLE IV

Values of $\overline{P}R$ when $R = 5$ and $\overline{V}_0$ is negative

R_m / $\overline{V}_0$	0	0.1	0.3	0.5
0.1	−2.3467	−2.3475	−2.3491	−2.3507
0.3	−3.1115	−3.1177	−3.1302	−3.1427
0.5	−3.9505	−3.9656	−3.9956	−4.0254

when $S' = 0$. An examination of the tables indicates that an increase in injection velocity will increase the tendency of separation due to an adverse pressure-gradient, while for suction the case is just the opposite. It may also be noted that the effect of an increase in R_m is the same as that of an increase in suction velocity.

§ 5. *Conclusions.* 1) For the case of two non-porous walls with the electric field $\boldsymbol{E}$ negligible, the effect of the increase in the strength of the magnetic field is (i) to increase the tendency of back-flow due to an adverse pressure gradient and (ii) to reduce the viscous drag. With $\boldsymbol{E}$ present these remarks are just reversed.

2) For the case of flow between two porous walls the usual effect of suction to delay separation is helped by the presence of a magnetic field, but the effect of injection is opposed by the electromagnetic forces.

Acknowledgement. The author wishes to express his thanks to Prof. B. R. Seth and Dr. M. K. Jain for their continual guidance and encouragement.

Received 17th March, 1961.

REFERENCES

1) Schlichting, H., Boundary Layer Theory, Pergamon Press Ltd., 1955.
2) Illingworth, C. R., Proc. Camb. Phil. Soc. **46** (1950) 469.
3) Liepmann, H. W. and Z. O. Bleviss, The effects of Dissociation and Ionization on compressible Couette flow, Douglas Aircraft Company, Inc., Report No. SM-19831, May, 1956.
4) Lehnert, B. O., Ark. Fys. **5** (1952) 69.
5) Liepmann, H. W., Plasma in a magnetic field, ed. R. K. M. Landshoff, Stanford Univ. Press., 1958, pp. 117–130.
6) Bleviss, Z. O., J. Aero/Space Sci. **25**(1958) 601.
7) Lilley, M., J. Aero/Space Sci. **26** (1959) 685.

ON THE CAPACITANCE OF A CUBE

by J. VAN BLADEL and K. MEI *)

Department of Electrical Engineering University of Wisconsin, U.S.A.

Summary

It is known that the capacitance of a metallic object can be obtained from a variational principle. The variational method is compared to Maxwell's method of subareas, and specific results for a metallic cube give an idea of the accuracy obtainable by each method.

The electrostatic capacitance of a conducting body can be found by solving the following integral equation:

$$\frac{1}{4\pi\varepsilon_0} \iint_S \frac{\eta(P)\, \mathrm{d}S_P}{|\bar{r}_P - \bar{r}_Q|} = V = 1 \tag{1}$$

for the surface charge density η which appears when the conductor is at unit potential. The capacitance is subsequently obtained as

$$C = \frac{Q}{V} = \iint_S \eta\, \mathrm{d}S.$$

In practice, an approximate solution of (1) can be accomplished by dividing S into N subareas, and assuming η to be constant over each subarea. The potential at any point Q now becomes a linear function of the η_i. We can determine the N unknown η_i by setting this potential equal to one at N points, one in each subarea for example. To that effect, it is convenient to choose one reference point P_i in each subarea ΔS_i, and to write

$$\frac{1}{4\pi\varepsilon_0} \sum_{i \neq j} \frac{\eta(P_i)\, \Delta S_i}{|\bar{r}_{P_i} - \bar{r}_{P_j}|} + \frac{1}{4\pi\varepsilon_0}\, \eta(P_j) \iint_{\Delta S_j} \frac{\mathrm{d}S}{|\bar{r} - \bar{r}_{P_j}|} = 1$$

---

*) Supported by a Wisconsin Alumni Research Association research grant.

for the N points P_j. Notice that the second term represents the potential to which ΔS_j is raised under the influence of its own charge, while the first term represents, in an approximate fashion, the contribution from the other subareas (the approximation clearly resides in assuming a constant distance $1/(|\bar{r}_{P_i} - \bar{r}_{P_j}|)$ throughout the subareas). The value of the capacitance obtained from this method, namely

$$C = \sum_{i=1}^{N} \eta(P_i)\, \Delta S_i,$$

improves as the number of subdivisions increases. Higgins and Reitan have applied the method to a large number of geometrical shapes [1–4]. In the present note, we investigate the possibility of obtaining better values of the capacitance without additional labour.

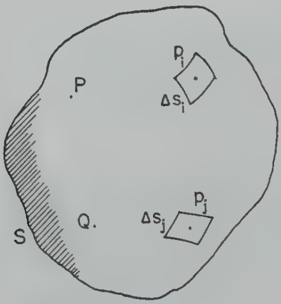

Fig. 1. Conducting body.

It is well-known [5], indeed, that the following functional

$$J(f) = \frac{\int_a^b f(x)\, \mathrm{d}x \int_a^b f(x')\, K(x|x')\, \mathrm{d}x'}{[\int_a^b f(x)\, g(x)\, \mathrm{d}x]^2}$$

is stationary with respect to small variations around the solution of the integral equation

$$\int_a^b f(x')\, K(x|x')\, \mathrm{d}x' = g(x),$$

the admissible function satisfying the auxiliary condition

$$\int_a^b f(x)\, g(x)\, \mathrm{d}x = 1.$$

Applied to the given electrostatic situation, this principle implies that the unknown function η, subject to the condition that the total charge $\int\int \eta\, \mathrm{d}S$ be equal to one, makes the expression

$$J(\eta) = \iint_S \eta(P)\, \mathrm{d}S_P \iint_S \frac{\eta(Q)\, \mathrm{d}S\,(Q)}{|\bar{r}_P - \bar{r}_Q|} \tag{2}$$

stationary, and the stationary value is equal to $4\pi\varepsilon_0/C$. This variational principle has been quoted in the literature [6]), and it is found thst expression (2) provides an upper bound for $4\pi\varepsilon_0/C$, i.e.

$$C \geqslant 4\pi\varepsilon_0/J(\eta)$$

for all admissible η, the equality being obtained for the "right" charge distribution. The authors were interested in checking the results yielded by the "brute force" and "variational methods" respectively. The method of subareas was applied in each case, that is, functions η of the type described above were used as trial functions for (2). The variational principle (2) then takes the form

$$J(\eta_1 \ldots \eta_N) = \sum_i \eta(P_i)\, \Delta S_i \left[\sum_{i \neq j} \frac{\eta(P_j)\, \Delta S_j}{|\bar{r}_{P_i} - \bar{r}_{P_j}|} + \eta(P_i) \iint_{\Delta S_i} \frac{\mathrm{d}S}{|\bar{r} - \bar{r}_{P_i}|} \right]$$

with the auxiliary relation

$$\sum_i \eta_i \Delta S_i = 1.$$

The last relation allows elimination of one η, and J becomes a function of $(N - 1)$ parameters only, the best values of which are found from

$$\frac{\partial J}{\partial \eta_1} = \frac{\partial J}{\partial \eta_2} = \ldots \frac{\partial J}{\partial \eta_{N-1}} = 0.$$

As a test case, the cube was chosen because of its geometric simplicity. Dividing the area as indicated in fig. 2, we find that symmetry sharply decreases the number N_i of independent values of η to be considered. For $n = 3$, for example, there are only 3 independent values of η, namely those in squares A, B and C. This represents an important simplification, since the number of simultaneous linear equations is equal to $N_i - 1$. Computations were performed on a high-speed digital computer. Table I gives the results for C in e.s.u., where a is the side of the cube in cm.

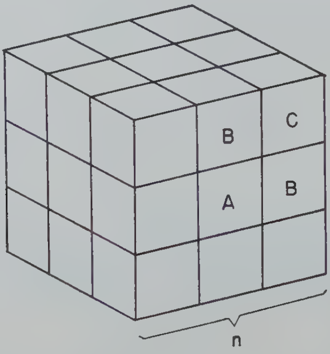

Fig. 2. Conducting cube divided into subareas.

TABLE I

	$n = 4$	$n = 6$
Higgins and Reitan [1]	$0.648a$	$0.655a$
Variational	$0.65091a$	$0.65565a$

The variational method provides a more rapid convergence.

Received 25th March, 1961.

REFERENCES

1) Reitan, D. K., and T. J. Higgins, J. Appl. Phys. **22** (1951) 223.
2) Higgins, T. J. and D. K. Reitan, Trans. Amer. Elect. Engrs **70** (1951) 926.
3) Reitan, D. K. and T. J. Higgins, Trans. Amer. Inst. Elect. Engrs. **75** (1956) 761.
4) Reitan, D. K. J. Appl. Phys. **30** (1959) 172.
5) See e.g., T. Kahan *et al*, Les Methodes d'Approximation variationnelles dans la théorie des collisions atomiques et dans la physique des piles nucléaires, Gauthier-Villars, Paris, 1956.
6) Pólya, G. and G. Szegö, Isoperimetric Inequalities in Mathematical Physics, Princeton University Press, 1951, p. 56.

Appl. sci. Res. Section B, Vol. 9

THE MAGNETOHYDRODYNAMIC PROBLEM OF AN OSCILLATING PLATE OF FINITE CONDUCTIVITY

by F. J. YOUNG and W. F. HUGHES

Carnegie Institute of Technology, Pittsburgh, U.S.A.

Summary

A detailed study is made of the oscillating and uniform motion of a conducting plate in a conducting fluid in the presence of an externally applied magnetic field normal to the plate. Limiting solutions are obtained for the case where the fluid is replaced by two semi-infinite solids. Attention is given to the boundary conditions and their limits for a perfectly conducting and non-conducting plate. It is found that the velocity profile in the fluid is rather closely bounded by the two limiting cases of perfectly conducting and non-conducting plates while the induced magnetic field profile differs markedly for the two extremes. Curves of sample profiles are shown.

§ 1. *Introduction.* The problem of a moving plate in a conducting fluid in the presence of a magnetic field has been extensively investigated for certain special cases. The impulsive motion or Rayleigh problem with a magnetic field applied normal to the plate has been discussed by Rossow [1]), Chang and Yen [2]), and Ludford [3]). However, all of these solutions are based on the assumption that the plate is either a perfect conductor or insulator. Recently Drake [4]) has investigated this problem for the impulsive motion of a plate of arbitrary conductivity. The problem of the motion of the plate when the magnetic field is alligned with the plate has been discussed by Carrier and Greenspan [5])[6]).

Another problem that has received attention recently is the oscillating motion of a plate in a conducting fluid with a magnetic field applied normal to the plate (fig. 1). A solution to this problem when the plate is an insulator or non-conductor was presented by Hide and Roberts [7]) in connection with certain geomagnetic problems, and the more general problem where the plate has an arbitrary conductivity was discussed by Axford[8]), but actual solutions were obtained only under the simplifying approximation of a perfectly conducting plate.

In the present work solutions are presented for the more general problem of the oscillating plate of arbitrary conductivity. The steady uniform motion of the plate and the motion of the plate between two semi-infinite solids are also studied. Detailed attention is given to the boundary conditions and their limits for the cases of perfectly conducting and non-conducting plates. It is found that the velocity profiles in the fluid are rather tightly bound by these two limiting cases, but that the induced magnetic field profiles differ markedly for the two limits.

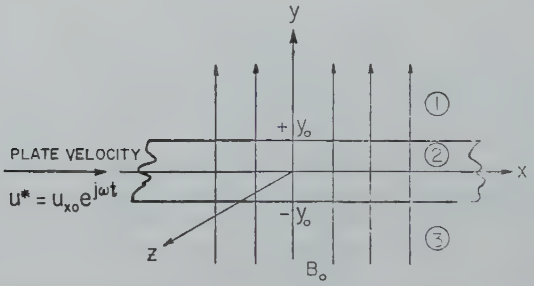

Fig. 1. Sketch of the oscillating plate showing the coordinate system.

The basic equations used here are Maxwell's equations and the equations of motion of the fluid. The relevant Maxwell's equations can be written (using R.M.K.S. units throughout), neglecting displacement currents and assuming non-magnetic media, and realising the space charge density is zero:

$$\nabla \times \boldsymbol{B}^* = \mu_0 \boldsymbol{J}^*, \tag{1}$$

$$\nabla \cdot \boldsymbol{B}^* = 0; \ \nabla \cdot \boldsymbol{D}^* = 0, \tag{2}$$

$$\nabla \times \boldsymbol{E}^* = -\frac{\partial \boldsymbol{B}^*}{\partial t}. \tag{3}$$

The simplified form of Ohm's law will be used:

$$\boldsymbol{J}^* = \sigma(\boldsymbol{E}^* + \boldsymbol{u}^* \times \boldsymbol{B}^*). \tag{4}$$

Here $\boldsymbol{J}^*$ is the current density, $\boldsymbol{u}^*$ the fluid velocity, $\boldsymbol{E}^*$ the electric field, $\boldsymbol{H}^*$ the magnetic field, $\boldsymbol{B}^*$ the magnetic induction, and σ the scalar conductivity. (The starred variables are used since the unstarred ones will be reserved for quantities defined later.)

The Navier-Stokes equation of motion can be written for an incompressible fluid

$$\rho \frac{\partial \boldsymbol{u}^*}{\partial t} = -\nabla P^* + \mu \nabla^2 \boldsymbol{u}^* + \boldsymbol{J}^* \times \boldsymbol{B}^*, \tag{5}$$

where P^* is the fluid pressure, μ the viscosity, and ρ the fluid density, and the equation of continuity for an incompressible fluid is

$$\nabla \cdot \boldsymbol{u}^* = 0. \tag{6}$$

§ 2. *Equations of the system.* The problem described can be solved by the application of Maxwell's equations, Ohm's law, and the fluid equations. Referring to fig. 1, by symmetry all partial derivatives of velocity and electromagnetic field quantities taken with respect to x or z vanish. Then from $\nabla \cdot \boldsymbol{B}^* = 0$ it follows that B_y^* is a function of time only and B_0 is a constant. The divergence equation for electric flux density (the space charge is zero) indicates that D_y^* is a function of time only which is taken to be zero because no y component of electric field is applied at $y = \pm\infty$. Similarly, the fluid being incompressible, the fluid equation of continuity indicates that u_y^* is zero. From the y component of $\nabla \times \boldsymbol{B}^* = \mu_0 \boldsymbol{J}^*$ it follows that $B_z^* = 0$ if $E_y^* = 0$ and $u_x^* \neq 0$. The z component of $\nabla \times \boldsymbol{E}^* = -\partial \boldsymbol{B}^*/\partial t$ indicates that E_x^* is a function of time only which can be assigned a value of zero. The twelve fundamental equations now reduce to

$$\frac{\partial E_z^*}{\partial y} = -\frac{\partial B_x^*}{\partial t}, \tag{7}$$

$$-\frac{\partial B_x^*}{\partial y} = \mu_0 \sigma (E_z^* + B_0 u_x^*), \tag{8}$$

$$\rho \frac{\partial u_x^*}{\partial t} = -\frac{\partial P^*}{\partial x} + \mu \frac{\partial^2 u_x^*}{\partial y^2} - \sigma B_0 E_z^* - \sigma B_0^2 u_x^*, \tag{9}$$

$$\frac{\partial P^*}{\partial y} = \sigma B_x^* (E_z^* + B_0 u_x^*), \tag{10}$$

$$\frac{\partial P^*}{\partial z} = 0. \tag{11}$$

In the problems under consideration here $\partial P^*/\partial x = 0$. To obtain a solution, (7), (8) and (9) must be solved simultaneously, an(d10) may be used to find $\partial P^*/\partial y$.

§ 3. *Boundary conditions.* Because the system of equations is fourth order in the variable y, as many as four boundary conditions may be needed. Obviously, $u_x^*(\infty) = 0$ and $u_x^*(\pm y_0) = u_{x0}^*$ if no slip occurs at the surfaces of the plate. In the literature there seems to have been some question about the boundary conditions applicable to the electromagnetic field quantities ^{2}) when the plate is a perfect conductor. However, for a plate of finite conductivity the tangential components of the magnetic and electric field are continuous at the boundaries or interface between two adjoining media. This is a continuity of field quantities as measured by a single observer (having an arbitrary velocity) and not a continuity of field quantities as measured by a local observer moving with the media at the point of measurement. These two statements are equivalent except, for instance, where the velocity is discontinuous at the interface and the validity of the above conclusions follows directly from the integral form of Maxwell's equations.

§ 4. *Plate oscillating between solids.* Regions 1 and 3 of fig. 1 are semi-infinite solids having conductivity σ_1, permitivity ε_0 and permeability μ_0. Region 2 is an infinite plate of thickness $2y_0$ having the properties σ_2, ε_0, and μ_0 and executing simple harmonic motion. In this case Maxwell's equations reduce to

$$\frac{\mathrm{d}E_z}{\mathrm{d}y} = -j\omega B_x, \quad -\infty < y < \infty, \tag{12}$$

$$-\frac{\mathrm{d}B_x}{\mathrm{d}y} = \mu_0\sigma(E_z + B_0U_x), \quad -y_0 \leq y \leq y_0, \tag{13a}$$

$$\frac{\mathrm{d}B_x}{\mathrm{d}y} = -\mu_0\sigma E_z, \quad |y| \geq y_0, \tag{13b}$$

assuming any field quantity $\boldsymbol{F}^* = \boldsymbol{F}\,\mathrm{e}^{j\omega t}$. In this problem two boundary conditions are needed at each boundary. They are $E_{z1}(y_0) = E_{z2}(y_0)$, $B_{x1}(y_0) = B_{x2}(y_0)$, $E_{z2}(-y_0) = E_{z3}(-y_0)$, and $B_{x2}(-y_0) = B_{x3}(-y_0)$. Here the integral subscripts denote the region being considered. The solutions which satisfy (12), (13*a*), (13*b*) and the boundary conditions are

$$E_{z1} = -\frac{\sqrt{\sigma_2/\sigma_1}\sinh y_0\sqrt{j\omega\mu_0\sigma_2}\, u_{x0}B_0\, \mathrm{e}^{-(y-y_0)\sqrt{j\omega\mu_0\sigma_1}}}{\cosh y_0\sqrt{j\omega\mu_0\sigma_2} + \sqrt{\sigma_2/\sigma_1}\sinh y_0\sqrt{j\omega\mu_0\sigma_2}}, \quad (14)$$

$$E_{z2} = \frac{\cosh y\sqrt{j\omega\mu_0\sigma_2} - \cosh y_0\sqrt{j\omega\mu_0\sigma_2} - \sqrt{\sigma_2/\sigma_1}\sinh y_0\sqrt{j\omega\mu_0\sigma_2}}{\cosh y_0\sqrt{j\omega\mu_0\sigma_2} + \sqrt{\sigma_2/\sigma_1}\sinh y_0\sqrt{j\omega\mu_0\sigma_2}}\, u_{x0}B_0, \quad (15)$$

$$E_{z3} = \frac{(-\sqrt{\sigma_2/\sigma_1}\sinh y_0\sqrt{j\omega\mu_0\sigma_2})\, u_{x0}B_0\, \mathrm{e}^{(y+y_0)\sqrt{j\omega\mu_0\sigma_1}}}{\cosh y_0\sqrt{j\omega\mu_0\sigma_2} + \sqrt{\sigma_2/\sigma_1}\sinh y_0\sqrt{j\omega\mu_0\sigma_2}}, \quad (16)$$

$$B_{x1} = \frac{(j\sqrt{j\mu_0\sigma_2/\omega}\sinh y_0\sqrt{j\omega\mu_0\sigma_2})\, u_{x0}B_0\, \mathrm{e}^{-(y-y_0)\sqrt{j\omega\mu_0\sigma_1}}}{\cosh y_0\sqrt{j\omega\mu_0\sigma_2} + \sqrt{\sigma_2/\sigma_1}\sinh y_0\sqrt{j\omega\mu_0\sigma_2}}, \quad (17)$$

$$B_{x2} = \frac{(j\sqrt{j\mu_0\sigma_2/\omega}\sinh y\sqrt{j\omega\mu_0\sigma_2})\, u_{x0}B_0}{\cosh y_0\sqrt{j\omega\mu_0\sigma_2} + \sqrt{\sigma_2/\sigma_1}\sinh y_0\sqrt{j\omega\mu_0\sigma_2}}, \quad (18)$$

$$B_{x3} = \frac{-(j\sqrt{j\mu_0\sigma_2/\omega}\sinh y_0\sqrt{j\omega\mu_0\sigma_2})\, u_{x0}B_0\, \mathrm{e}^{(y+y_0)\sqrt{j\omega\mu_0\sigma_2}}}{\cosh y_0\sqrt{j\omega\mu_0\sigma_2} + \sqrt{\sigma_2/\sigma_1}\sinh y_0\sqrt{j\omega\mu_0\sigma_2}}, \quad (19)$$

where u_{x0} is the amplitude of the plate velocity. It is of particular interest to examine $\mathrm{d}B_{x1}/\mathrm{d}y$ and $\mathrm{d}B_{x2}/\mathrm{d}y$:

$$\frac{\mathrm{d}B_{x1}}{\mathrm{d}y} = \frac{(\mu_0\sqrt{\sigma_1\sigma_2}\sinh y_0\sqrt{j\omega\mu_0\sigma_2})u_{x0}B_0\mathrm{e}^{-(y-y_0)\sqrt{j\omega\mu_0\sigma_1}}}{\cosh y_0\sqrt{j\omega\mu_0\sigma_2} + \sqrt{\sigma_2/\sigma_1}\sinh y_0\sqrt{j\omega\mu_0\sigma_2}}, \quad (20)$$

$$\frac{\mathrm{d}B_{x2}}{\mathrm{d}y} = \frac{-\mu_0\sigma_2 u_{x0}B_0\cosh y\sqrt{j\omega\mu_0\sigma_2}}{\cosh y_0\sqrt{j\omega\mu_0\sigma_2} + \sqrt{\sigma_2/\sigma_1}\sinh y_0\sqrt{j\omega\mu_0\sigma_2}}, \quad (21)$$

When $\sigma_2 \to \infty$, the oscillating sheet is a perfect conductor and

$$\lim_{\sigma_2\to\infty}\frac{\mathrm{d}B_{x1}}{\mathrm{d}y} = \mu_0\sigma_1 u_{x0}B_0\, \mathrm{e}^{-(y-y_0)\sqrt{j\omega\mu_0\sigma_1}}. \quad (22)$$

At the boundaries of media 1 and 3

$$\lim_{\sigma_2\to\infty}\frac{\mathrm{d}B_{x1}(y_0)}{\mathrm{d}y} = \mu_0\sigma_1 u_{x0}B_0, \quad (23)$$

and the current density is $-B_0u_{x0}\sigma_1$. This is the current density (in the *z* direction) that would exist (neglecting eddy currents).

in a medium of properties σ_1 and μ_0 if it moved through a uniform field B_0 with a velocity $-u_{x0}$. When σ_2 is large,

$$\frac{\mathrm{d}B_{x2}}{\mathrm{d}y} \simeq -B_0 u_{x0} \mu_0 \sqrt{\sigma_1 \sigma_2}\, \mathrm{e}^{-(y_0-y)\sqrt{j\omega\mu_0\sigma_2}}. \tag{24}$$

At $y = \pm y_0$, $\mathrm{d}B_{x2}/\mathrm{d}y = -\infty$ when σ_2 is infinite, whereas for $-y_0 < y < y_0$, $\mathrm{d}B_{x2}/\mathrm{d}y = 0$. Physically, there is an intense current sheet flowing on the surfaces of the moving conductor which shields the interior of medium 2 from induced magnetic fields. From (18) for very large σ_2

$$B_{x2} = j\sqrt{j}\, B_0 u_{x0} \sqrt{\mu_0\sigma_1/\omega}\, \mathrm{e}^{-(y_0-y)\sqrt{j\omega\mu_0\sigma_2}}. \tag{25}$$

At $y = \pm y_0$, B_{x2} jumps from a finite value to zero. The current sheets account for the discontinuity in the B field at the boundaries of region 2.

It is interesting to note that for $\sigma_2 = \infty$, $E_{z2} = -u_{x0}B_0$ for $-y_0 < y < y_0$, which makes $\mathrm{d}B_{x2}/\mathrm{d}y = 0$ by (13*a*). Thus, there is no current in region 2 other than the two infinite current sheets.

§ 5. *Plate moving with constant velocity in a fluid.* Assume the system is short circuited, so that $E_z^* = 0$. In the steady state there will be no time variations. Under these conditions (7) vanishes and (8) and (9) become

$$\frac{\mathrm{d}^2 u_{xi}^*}{\mathrm{d}y^2} - \frac{\sigma_i B_0^2}{\mu_0} u_{xi}^* = 0, \quad \text{for} \quad i = 1,3 \tag{26}$$

$$-\frac{\mathrm{d}B_{xi}^*}{\mathrm{d}y} = \mu_0 \sigma_i B_0 u_{xi}^*. \tag{27}$$

The boundary conditions are $u_{x1}^*(y_0) = u_{x3}^*(-y_0) = u_{x0}^*$, $B_{x1}(y_0) = B_{x2}(y_0)$ and $B_{x1}(-y_0) = B_{x2}(-y_0)$. The solutions to (25) and (26) which satisfy the boundary conditions are

$$u_{x1}^* = u_{x0}^*\, \mathrm{e}^{-(y-y_0)B_0\sqrt{\sigma_1/\mu_0}}, \tag{28}$$

$$u_{x2}^* = u_{x0}^*, \tag{29}$$

$$u_{x3}^* = u_{x0}^*\, \mathrm{e}^{(y+y_0)B_0\sqrt{\sigma_1/\mu_0}}, \tag{30}$$

$$B_{x1}^* = -\mu_0 u_{x0}^* \{\sqrt{\sigma_1\mu_0}\,[1 - \mathrm{e}^{-(y-y_0)B_0\sqrt{\sigma_1/\mu_0}}] + B_0\sigma_2 y_0\}, \tag{31}$$

$$B_{x2}^* = -\mu_0 u_{x0}^* B_0 \sigma_2 y, \tag{32}$$

$$B_{x3}^* = \mu_0 u_{x0}^* \{\sqrt{\sigma_1\mu_0}[1 - \mathrm{e}^{(y+y_0)B_0\sqrt{\sigma_1/\mu_0}}] - B_0\sigma_2 y_0\}. \tag{33}$$

Also of interest are

$$\frac{\mathrm{d}B_{x1}^*}{\mathrm{d}y} = -\mu_0 u_{x0}^* B_0 \sigma_1 \, \mathrm{e}^{-(y-y_0)B_0\sqrt{\sigma_1/\mu_0}}, \tag{34}$$

$$\frac{\mathrm{d}B_{x2}^*}{\mathrm{d}y} = -\mu_0 u_{x0}^* B_0 \sigma_2, \tag{35}$$

$$\frac{\mathrm{d}B_{x3}^*}{\mathrm{d}y} = -\mu_0 u_{x0}^* B_0 \sigma_1 \, \mathrm{e}^{(y+y_0)B_0\sqrt{\sigma_1/\mu_0}}. \tag{36}$$

In this problem, regardless of the conductivity of the plate, at the boundary

$$\frac{\mathrm{d}H_{xi}^*}{\mathrm{d}y} = -u_{x0}^* B_0 \sigma_1. \tag{37}$$

Then the current density in the fluid next to the boundary is $u_{x0}^* B_0 \sigma_1$, which is the current expected in a solid of properties σ_1 and μ_0 moving normal to a field B_0 with velocity u_{x0}^*. For an insulating plate $\mathrm{d}B_{x2}^*/\mathrm{d}y = 0$ only in the plate and (36) remains unchanged.

It is interesting to observe the behaviour of the magnetic flux density when σ_2 becomes large. The value of B_{xi}^* then grows very large, indicating that the magnetic field is frozen into the plate as one would expect.

§ 6. *Plate of finite conductivity oscillating in a fluid.* To simplify this problem, let $\bar{y} = y\sqrt{\omega/\nu}$, $\bar{B}_i = B_{xi}/B_0$, $\bar{E}_i = (E_{zi}/B_0)\,\mu_0\sigma_i\sqrt{\nu/\omega}$, $\bar{U}_i = \mu_0\sigma_i\sqrt{\nu/\omega}\,u_x$, $\pi_1 = \sigma_f B_0^2/\omega\rho$, $\pi_2 = \mu_0\sigma_f\nu$ and $\pi_3 = \sigma_f/\sigma_P$, where σ_f is the conductivity of the fluid and σ_P is the conductivity of the oscillating plate, while ν is the kinematic viscosity of the fluid. Equations (7), (8), and (9) become (assuming $\boldsymbol{F}^* = \boldsymbol{F}\,\mathrm{e}^{j\omega t}$):

$$\mathrm{d}\bar{E}_i/\mathrm{d}\bar{y} = -j\pi_{2i}\bar{B}_i, \tag{38}$$

where $\pi_{2i} = \mu_0\sigma_i\nu$

$$-\mathrm{d}\bar{B}_i/\mathrm{d}\bar{y} = \bar{E}_i + \bar{U}_i; \tag{39}$$

for $i = 1, 3$

$$j\bar{U}_i = \frac{\mathrm{d}^2\bar{U}_i}{\mathrm{d}\bar{y}^2} - \pi_{1i}(\bar{E}_i + \bar{U}_i), \tag{40}$$

where $\pi_{1i} = \sigma_i B_0{}^2/\omega\rho$. From (38)

$$\bar{B}_i = -\frac{1}{j\pi_{2i}} \frac{\mathrm{d}\bar{E}_i}{\mathrm{d}\bar{y}}.$$

Substituting this into (39) there results

$$\frac{1}{j\pi_{2i}} \frac{\mathrm{d}^2\bar{E}_i}{\mathrm{d}\bar{y}^2} = \bar{E}_i + \bar{U}_i. \tag{41}$$

From (40)

$$\bar{E}_i = \frac{1}{\pi_i}\left[\frac{\mathrm{d}^2\bar{U}_i}{\mathrm{d}\bar{y}^2} - (j + \pi_{1i})\,\bar{U}_i\right]. \tag{42}$$

From (42)

$$\frac{\mathrm{d}^2\bar{E}_i}{\mathrm{d}\bar{y}^2} = \frac{1}{\pi_{1i}}\left[\frac{\mathrm{d}^4\bar{U}_i}{\mathrm{d}\bar{y}^4} - (j + \pi_{1i})\,\frac{\mathrm{d}^2\bar{U}_i}{\mathrm{d}\bar{y}^2}\right]. \tag{43}$$

Substituting (42) and (43) into (41) and mutiplying by π_{1i} we obtain

$$\frac{\mathrm{d}^4\bar{U}_i}{\mathrm{d}\bar{y}^4} - \left[\pi_{1i} + j(1 + \pi_{2i})\right]\frac{\mathrm{d}^2\bar{U}_i}{\mathrm{d}\bar{y}^2} - \pi_{2i}\bar{U}_i = 0. \tag{44}$$

The solution to (44) is

$$\bar{U}_i = A_i\,\mathrm{e}^{-P_1\bar{y}} + B_i\,\mathrm{e}^{-P_2\bar{y}} + C_i\,\mathrm{e}^{P_1\bar{y}} + D_i\,\mathrm{e}^{P_2\bar{y}} \text{ for } i = 1, 3. \tag{45}$$

where A_i, B_i, C_i, and D_i are constants. Because the velocity must be zero at $\bar{y} = \infty$, $C_1 = D_1 = 0$ and $A_3 = B_3 = 0$. Here the roots are given by (noting that $\pi_{21} = \pi_{23} \equiv \pi_2$ and $\pi_{11} = \pi_{13} \equiv \pi_1$)

$$P = \sqrt{\frac{\pi_1 + j(1 + \pi_2) \pm \sqrt{\pi_1{}^2 - 1 + 2\pi_2 - \pi_2{}^2 + 2j\pi_1(1 + \pi_2)}}{2}}. \tag{46}$$

In appendix 1, P_1 and P_2 are put into a more useful form, and certain useful relationships are established. The solutions for the velocities are then

$$\bar{U}_1 = A_1\,\mathrm{e}^{-P_1\bar{y}} + B_1\,\mathrm{e}^{-P_2\bar{y}}, \tag{47}$$

$$\bar{U}_2 = \mu_0\sigma_P\sqrt{\nu/\omega}\,u_{x0}, \tag{48}$$

$$\bar{U}_3 = C_3\,\mathrm{e}^{P_1\bar{y}} + D_3\,\mathrm{e}^{P_2\bar{y}}. \tag{49}$$

From (42)

$$\bar{E}_1 = \frac{1}{\pi_1}(\gamma_1 A_1\,\mathrm{e}^{-P_1\bar{y}} + \gamma_2 B_1\,\mathrm{e}^{-P_2\bar{y}}), \tag{50}$$

$$\bar{E}_3 = \frac{1}{\pi_1}(\gamma_1 C_3\,\mathrm{e}^{P_1\bar{y}} + \gamma_2 D_3\,\mathrm{e}^{P_2\bar{y}}). \tag{51}$$

Here $\gamma_1 = P_1^2 - j - \pi_1$ and $\gamma_2 = P_2^2 - j - \pi_1$. In region 2,(41) becomes

$$\frac{d^2\bar{E}_2}{d\bar{y}^2} - j\pi_{22} = j\pi_{22}\bar{U}_{02}, \tag{52}$$

where $\bar{U}_{02} = \mu_0\sigma_P u_{x0}\sqrt{\nu/\omega}$. The solution to this equation is then

$$\bar{E}_3 = A_2 \cosh \bar{y}\sqrt{j\pi_{22}} + B_2 \sinh \bar{y}\sqrt{j\pi_{22}} - \bar{U}_{02}. \tag{53}$$

The magnetic inductions are easily found to be

$$\bar{B}_1 = \frac{1}{j\pi_1\pi_2}\left(P_1\gamma_1 A_1 e^{-P_1\bar{y}} + P_2\gamma_2 B_1 e^{-P_2\bar{y}}\right), \tag{54}$$

$$\bar{B}_2 = \frac{-1}{\sqrt{j\pi_{22}}}\left(A_2 \sinh \bar{y}\sqrt{j\pi_{22}} + B_2 \cosh \bar{y}\sqrt{j\pi_{22}}\right), \tag{55}$$

$$\bar{B}_3 = \frac{-1}{j\pi_1\pi_2}\left(P_1\gamma_1 C_3 e^{P_1\bar{y}} + P_2\gamma_2 D_3 e^{P_2\bar{y}}\right). \tag{56}$$

From Ampere's circuital law it is clear that $A_1 = C_3$ and $B_1 = D_3$. Then the E field is symmetric and $B_2 = 0$. The E fields become

$$\bar{E}_1 = \frac{1}{\pi_1}\left(\gamma_1 A_1 e^{-P_1\bar{y}} + \gamma_2 B_1 e^{-P_2\bar{y}}\right), \tag{57}$$

$$\bar{E}_2 = A_2 \cosh \bar{y}\sqrt{j\pi_{22}} - \bar{U}_{02}, \tag{58}$$

$$\bar{E}_3 = \frac{1}{\pi_1}\left(\gamma_1 A_1 e^{P_1\bar{y}} + \gamma_2 B_1 e^{P_2\bar{y}}\right). \tag{59}$$

The boundary conditions at $\bar{y} = \bar{y}_0 = y_0\sqrt{\omega/\nu}$ are $\bar{B}_1 = \bar{B}_2$, $\bar{E}_1/\sigma_f = \bar{E}_2/\sigma_P$, and $\bar{U}_1 = \bar{U}_{01}$, where $\bar{U}_{01} = \mu_0\sigma_f u_{x0}\sqrt{\nu/\omega}$. Then

$$\frac{1}{\pi_1\sigma_f}\left(\gamma_1 A_1 e^{-P_1\bar{y}_0} + \gamma_2 B_1 e^{-P_2\bar{y}_0}\right) = \frac{A_2}{\sigma_P}\cosh \bar{y}_0\sqrt{j\pi_{22}} - \frac{\bar{U}_{02}}{\sigma_P}, \tag{60}$$

$$\frac{1}{\pi_1\pi_2}\left(P_1\gamma_1 A_1 e^{-P_1\bar{y}_0} + P_2\gamma_2 B_1 e^{-P_1\bar{y}_0}\right) = -\sqrt{\frac{j}{\pi_{22}}}A_2 \sinh \bar{y}_0\sqrt{j\pi_{22}}. \tag{61}$$

Solving (60) and (61) simultaneously yields

$$A_1 = \frac{\begin{array}{l} A_2\pi_1(\pi_3 P_2 \cosh \bar{y}_0\sqrt{j\pi_{22}} + \\ \qquad + \pi_2\sqrt{j/\pi_{22}} \sinh \bar{y}_0\sqrt{j\pi_{22}}) - \pi_1\pi_3 P_2\bar{U}_{02} \end{array}}{(P_2 - P_1)\,\gamma_1 e^{-P_1\bar{y}_0}}, \tag{62}$$

$$B_1 = \frac{\begin{array}{l} -A_2\pi_1(\pi_2\sqrt{j/\pi_{22}}\sinh \bar{y}_0\sqrt{j\pi_{22}} + \\ \qquad\qquad + P_1\pi_3 \cosh \bar{y}\sqrt{j\pi_{22}}) + \pi_1\pi_3\, P_1\, \overline{U}_{02} \end{array}}{(P_2 - P_1)\,\gamma_2\, \mathrm{e}^{-P_2\bar{y}_0}}\,. \quad (63)$$

Also, because $\overline{U}_1(\bar{y}_0) = \pi_3\overline{U}_{01}$, by (47), (62) and (63)

$$A_2 = \frac{[(P_2 - P_1)\,\gamma_1\gamma_2 + \pi_1(P_2\gamma_2 - P_1\gamma_1)]\,\pi_3\overline{U}_{02}}{\begin{array}{l} \pi_1[(P_2\gamma_2 - P_1\gamma_1)\,\pi_3 \cosh \bar{y}_0\sqrt{j\pi_{22}} + \\ \qquad\qquad + \pi_2\sqrt{j/\pi_{22}}(\gamma_2 - \gamma_1)\sinh \bar{y}_0\sqrt{j\pi_{22}} \end{array}}\,. \quad (64)$$

Substitution of (64) into (62) and (63) yields

$$A_1 = \frac{\begin{array}{l} P_2\gamma_2\pi_3 \cosh \bar{y}_0\sqrt{j\pi_{22}} + \\ \qquad + (\gamma_2 + \pi_1)\,\pi_2\,\sqrt{j/\pi_{22}}\sinh \bar{y}_0\sqrt{j\pi_{22}} \end{array}}{\begin{array}{l} (P_2\gamma_2 - P_1\gamma_1)\,\pi_3 \cosh \bar{y}_0\sqrt{j\pi_{22}} + \\ \qquad + \pi_2\,\sqrt{j/\pi_{22}}\,(\gamma_2 - \gamma_1)\sinh \bar{y}_0\sqrt{j\pi_{22}} \end{array}}\,\pi_3\overline{U}_{02}\,\mathrm{e}^{P_1\bar{y}_0}, (65)$$

$$B_1 = \frac{\begin{array}{l} -\,[P_1\gamma_1\pi_3 \cosh \bar{y}_0\sqrt{j\pi_{22}} + \\ \qquad + (\gamma_1 + \pi_1)\,\pi_2\sqrt{j/\pi_{22}}\sinh \bar{y}_0\sqrt{j\pi_{22}}]\,\pi_3\overline{U}_{02}\,\mathrm{e}^{P_2\bar{y}_0} \end{array}}{\begin{array}{l} (P_2\gamma_2 - P_1\gamma_1)\,\pi_3 \cosh \bar{y}_0\sqrt{j\pi_{22}} + \\ \qquad + \pi_2\sqrt{j/\pi_{22}}\,(\gamma_2 - \gamma_1)\sinh \bar{y}_0\sqrt{j\pi_{22}} \end{array}}\,. \quad (66)$$

Equation (47) then becomes ,using (65) and (66),

$$\frac{\overline{U}_1}{\overline{U}_{01}} = \frac{\begin{array}{l} [P_2\gamma_2\pi_3\cosh\bar{y}_0\sqrt{j\pi_2/\pi_3} + (\gamma_2+\pi_1)\pi_2\sqrt{j\pi_3/\pi_2}\sinh\bar{y}_0\sqrt{j\pi_2/\pi_3}]\mathrm{e}^{-P_1(\bar{y}-\bar{y}_0)} - \\ [P_1\gamma_1\pi_3\cosh\bar{y}_0\sqrt{j\pi_2/\pi_3} + (\gamma_1+\pi_1)\pi_2\sqrt{j\pi_3/\pi_2}\sinh\bar{y}_0\sqrt{j\pi_2/\pi_3}]\mathrm{e}^{-P_2(\bar{y}-\bar{y}_0)} \end{array}}{\begin{array}{l} (P_2\gamma_2 - P_1\gamma_1)\,\pi_3 \cosh \bar{y}_0\sqrt{j\pi_2/\pi_3} + \\ \qquad\qquad + \pi_2\sqrt{j\pi_3/\pi_2}\,(\gamma_2 - \gamma_1)\sinh \bar{y}_0\sqrt{j\pi_2/\pi_3} \end{array}} \text{(6}$$

and (50) yields

$$\bar{E}_1 = \frac{\begin{array}{l} [P_2\gamma_2\pi_3\cosh\bar{y}_0\sqrt{j\pi_2/\pi_3} + (\gamma_2+\pi_1)\pi_2\sqrt{j\pi_3/\pi_2}\sinh\bar{y}_0\sqrt{j\pi_2/\pi_3}]\gamma_1\mathrm{e}^{-P_1(\bar{y}-\bar{y}_0)} - \\ [P_1\gamma_1\pi_3\cosh\bar{y}_0\sqrt{j\pi_2/\pi_2} + (\gamma_1+\pi_1)\pi_2\sqrt{j\pi_3/\pi_2}\sinh\bar{y}_0\sqrt{j\pi_2/\pi_3}]\,\gamma_2\,\cdot \\ \qquad\qquad\qquad\qquad\qquad\qquad\qquad\qquad \cdot\,\mathrm{e}^{-P_2(\bar{y}-\bar{y}_0)}\,\overline{U}_{01}/\pi_1 \end{array}}{(P_2\gamma_2 - P_1\gamma_1)\,\pi_3 \cosh \bar{y}_0\sqrt{j\pi_2/\pi_3} + \pi_2\sqrt{j\pi_3/\pi_2}(\gamma_2 - \gamma_1)\sinh \bar{y}_0\sqrt{j\pi_2/\pi_3}}\text{.(6}$$

Substitution of (64) into (58) gives

$$\bar{E}_2 = \frac{\begin{array}{l} [(P_2 - P_1)\,\gamma_1\gamma_2 + \pi_1(P_2\gamma_2 - P_1\gamma_1)]\cosh \bar{y}\,\sqrt{j\pi_2/\pi_3} - \\ \qquad\qquad - \pi_1(P_2\gamma_2 - P_1\gamma_1)\cosh \bar{y}_0\,\sqrt{j\pi_2/\pi_3} - \\ \qquad\qquad - \pi_1\,\sqrt{j\pi_2/\pi_3}\,(\gamma_2 - \gamma_1)\sinh \bar{y}_0\,\sqrt{j\pi_2/\pi_3} \end{array}}{(P_2\gamma_2 - P_1\gamma_1)\pi_3\cosh\bar{y}_0\sqrt{j\pi_2/\pi_3} + \pi_2\sqrt{j\pi_3/\pi_2}(\gamma_2 - \gamma_1)\sinh\bar{y}_0\sqrt{j\pi_2/\pi_3}}\,\frac{\overline{U}_{01}}{\pi_1}\text{. (6}$$

The magnetic flux density is given by

$${}_1 = \frac{\left\{\begin{aligned} & P_1\gamma_1 [P_2\gamma_2\pi_3 \cosh \bar{y}_0 \sqrt{j\pi_2/\pi_3} + \\ &\qquad + (\gamma_2 + \pi_1)\, \pi_2\sqrt{j\pi_3/\pi_2} \sinh \bar{y}_0 \sqrt{j\pi_2/\pi_3}\, \mathrm{e}^{-P_1(\bar{y}-\bar{y}_0)} \\ & - P_2\gamma_2 [P_1\gamma_1\pi_3 \cosh \bar{y}_0 \sqrt{j\pi_2/\pi_3} + \\ &\qquad + (\gamma_1 + \pi_1)\, \pi_2\sqrt{j\pi_3/\pi_2} \sinh \bar{y}_0 \sqrt{j\pi_2/\pi_3}]\, \mathrm{e}^{-P_2(\bar{y}-\bar{y}_0)} \end{aligned}\right\} \dfrac{\bar{U}_{01}}{j\pi_1\pi_2}}{\begin{aligned} & (P_2\gamma_2 - P_1\gamma_1)\, \pi_3 \cosh \bar{y}_0 \sqrt{j\pi_2/\pi_3} + \\ &\qquad + \pi_2 \sqrt{j\pi_3/\pi_2}\, (\gamma_2 - \gamma_1) \sinh \bar{y}_0 \sqrt{j\pi_2/\pi_3} \end{aligned}}, \quad (70)$$

$${}_2 = \frac{- \sqrt{j\pi_2/\pi_3}\, [(P_2 - P_1)\, \gamma_1\gamma_2 + \pi_1(P_2\gamma_2 - P_1\gamma_1)] \sinh \bar{y} \sqrt{j\pi_2/\pi_3}}{\begin{aligned} & j\pi_1\pi_2 [(P_2\gamma_2 - P_1\gamma_1)\pi_3 \cosh \bar{y}_0 \sqrt{j\pi_2/\pi_3} + \\ &\qquad + \pi_2 \sqrt{j\pi_3/\pi_2}\, (\gamma_1 - \gamma_2) \sinh \bar{y}_0 \sqrt{j\pi_2/\pi_3}] \end{aligned}} \pi_3\bar{U}_{01}. \quad (17)$$

It is interesting to inspect the velocity and field quantities when $\bar{y}_0 \to 0$. The velocity is

$$\underset{\bar{y}_0=0}{\bar{U}_1} = \frac{P_2\gamma_2\, \mathrm{e}^{-P_1\bar{y}} - P_1\gamma_1\, \mathrm{e}^{-P_2\bar{y}}}{P_2\gamma_2 - P_1\gamma_1} \bar{U}_{01}. \quad (72)$$

The fields are

$$\underset{\bar{y}_0=0}{\bar{E}_1} = \frac{- P_2\, \mathrm{e}^{-P_1\bar{y}} + P_1\, \mathrm{e}^{-P_2\bar{y}}}{P_2\gamma_2 - P_1\gamma_1} j\pi_2\bar{U}_{01}, \quad (73)$$

$$\underset{\bar{y}_0=0}{\bar{B}_1} = \frac{- \mathrm{e}^{-P_1\bar{y}} + \mathrm{e}^{-P_2\bar{y}}}{P_2\gamma_2 - P_1\gamma_1} j\sqrt{\pi_2}\, \bar{U}_{01}. \quad (74)$$

As would be expected, (72), (73) and (74) are not dependent upon the conductivity of the plate and can be shown to be the solutions which would be obtained if the plate served only to establish a boundary condition on the velocity at $\bar{y} = 0$. The other boundary conditions needed would be the continuity of the electric and magnetic fields at the boundary $\bar{y} = 0$. Instead of these conditions on the field quantities some workers use the condition $\mathrm{d}\bar{B}_1(\bar{y} = 0)/\mathrm{d}\bar{y} = 0$ as a boundary condition. In this problem

$$\underset{\bar{y}_0=0}{\frac{\mathrm{d}\bar{B}_1}{\mathrm{d}\bar{y}}} = \frac{- P_1\, \mathrm{e}^{-P_1\bar{y}} + P_2\, \mathrm{e}^{-P_2\bar{y}}}{P_2\gamma_2 - P_1\gamma_1} \, \frac{P_2P_1\gamma_2\gamma_1\bar{U}_{01}}{j\pi_1\pi_2}. \quad (75)$$

Using (98) and (100) of appendix 1,

$$\underset{\bar{y}_0=0}{\frac{\mathrm{d}\bar{B}_1(\bar{y} = 0)}{\mathrm{d}\bar{y}}} = - \frac{\bar{U}_{01}}{1 + \sqrt{\pi_2}} \quad (76)$$

and

$$\underset{\bar{y}_0=0}{\bar{E}_1(\bar{y}=0)} = -\frac{\pi_2 \bar{U}_{01}}{1+\sqrt{\pi_2}}. \tag{77}$$

In terms of unnormalized quantities (76) becomes

$$\underset{\bar{y}_0=0}{\frac{\mathrm{d}B_{x1}}{\mathrm{d}y}} = -\frac{\mu_0\sigma_1 u_{x0} B_0}{1+\sqrt{\mu_0\sigma_1\nu}}. \tag{78}$$

From (78) it is clear that $\mathrm{d}B_{x1}(\bar{y}_0 = 0)/\mathrm{d}y = 0$ is a good approximation in cases where the kinematic viscosity is very large as in interstellar space.

When the plate is of finite thickness and is a good insulator, $\pi_3 \to \infty$ and the velocity and fields in the fluids are given by (72), (73) and (74) if $\bar{y}$ is replaced by $\bar{y} - \bar{y}_0$. The electric field in the plate in terms of unnormalized quantities is

$$E_{z2}(y) = \frac{-\pi_2 B_0 u_{x0}}{\pi_2 + \sqrt{\pi_2}}, \tag{79}$$

which is the same as $\underset{\bar{y}_0=0}{\bar{E}_1(\bar{y}=0)}$ of (77) and the magnetic induction in the insulating plate is zero.

When the oscillating plate is a very good conductor, $\pi_3 \to 0$. Then making use of the relations of appendix 1

$$\lim_{\pi_3\to 0} \bar{U}_1 = \frac{(P_2^2 - j)\,\mathrm{e}^{-P_1(\bar{y}-\bar{y}_0)} - (P_1^2 - j)\,\mathrm{e}^{-P_2(\bar{y}-\bar{y}_0)}}{P_2^2 - P_1^2}\,\bar{U}_{01}, \tag{80}$$

$$\lim_{\pi_3\to 0} \bar{E}_1 = \frac{-P_2^2\,\mathrm{e}^{-P_1(\bar{y}-\bar{y}_0)} + P_1^2\,\mathrm{e}^{-P_2(\bar{y}-\bar{y}_0)}}{P_2^2 - P_1^2}\,\bar{U}_{01}, \tag{81}$$

$$\lim_{\pi_3\to 0} \bar{E}_2(\bar{y}) = -B_0 u_{x0}, \tag{82}$$

$$\lim_{\pi_3\to 0} \bar{B}_1 = \frac{-P_2\,\mathrm{e}^{-P_1(\bar{y}-\bar{y}_0)} + P_1\,\mathrm{e}^{-P_2(\bar{y}-\bar{y}_0)}}{(P_2^2 - P_1^2)\sqrt{\pi_2}}\,\bar{U}_{01} \tag{83}$$

When π_3 is very small,

$$\bar{B}_2 = \frac{[(\gamma_2+\pi_1)\,P_1\gamma_1 - (\gamma_1+\pi_1)\,P_2\gamma_2]\,\mathrm{e}^{-(\bar{y}_0-\bar{y})\sqrt{j\pi_2/\pi_3}}}{j\pi_1\pi_2(\gamma_2-\gamma_1)}\,\bar{U}_{01}. \tag{84}$$

By the relations of appendix 1 (84) becomes

$$\bar{B}_2 = \frac{-\bar{U}_{01}\,\mathrm{e}^{-(\bar{y}_0-\bar{y})\sqrt{j\pi_2/\pi_3}}}{\sqrt{\pi_2[\pi_1 + j(1+\sqrt{\pi_2})]}}\,. \tag{85}$$

When $\bar{y} \equiv \bar{y}_0$

$$\lim_{\pi_3\to 0} \bar{B}_2 = \frac{-\bar{U}_{01}}{\sqrt{\pi_2[\pi_1 + j(1+\sqrt{\pi_2})^2}}\,, \tag{86}$$

and for $\bar{y} < \bar{y}_0$, $\bar{B}_2 = 0$. In the perfect conductor there is a discontinuity in the magnetic field which must be accompanied by a current sheet at the place of discontinuity.

It is easy to show that

$$\frac{\mathrm{d}\bar{B}_1}{\mathrm{d}\bar{y}} = \frac{\left\{\begin{array}{l} -P_1{}^2\gamma_1\,[P_2\gamma_2\pi_3 \cosh \bar{y}_0 \sqrt{j\pi_2/\pi_3}\, + \\ \qquad +\,(\gamma_2+\pi_1)\,\pi_2 \sqrt{j\pi_3/\pi_2}\,\sinh \bar{y}_0 \sqrt{j\pi_2/\pi_3}]\;\mathrm{e}^{-P_1(\bar{y}-\bar{y}_0)} \\ +P_2{}^2\gamma_2\,[P_1\gamma_1\pi_3 \cosh \bar{y}_0 \sqrt{j\pi_2/\pi_3}\, + \\ \qquad +\,(\gamma_1+\pi_1)\,\pi_2 \sqrt{j\pi_3/\pi_2}\,\sinh \bar{y}_0 \sqrt{j\pi_2/\pi_3}]\;\mathrm{e}^{-P_2(\bar{y}-\bar{y}_0)} \end{array}\right\}}{\begin{array}{l}(P_2\gamma_2 - P_1\gamma_1)\,\pi_3 \cosh \bar{y}_0\sqrt{j\pi_2/\pi_3}\, + \\ \qquad\qquad +\,\pi_2 \sqrt{j\pi_3/\pi_2}\,(\gamma_2-\gamma_1)\,\sinh \bar{y}_0 \sqrt{j\pi_2/\pi_3}\end{array}}\;\frac{U_{01}}{j\pi_1\pi_2}, \tag{87}$$

$$\frac{\mathrm{d}\bar{B}_2}{\mathrm{d}\bar{y}} = \frac{-\bar{U}_0 \cosh \bar{y}\,\sqrt{j\pi_2/\pi_3}}{(1+\sqrt{\pi_2})\pi_3 \cosh \bar{y}_0 \sqrt{j\pi_2/\pi_3} - j\sqrt{j\pi_3[\pi_1 + j(1+\sqrt{\pi_2})]}\,\sinh \bar{y}_0 \sqrt{j\pi_2/\pi_3}}, \tag{88}$$

$$\frac{\mathrm{d}\bar{B}_1(\bar{y}_0)}{\mathrm{d}\bar{y}} = \frac{-\bar{U}_{01}.}{1+\sqrt{\pi_2} - j\sqrt{j/\pi_3\,[\pi_1 + j\,(1+\sqrt{\pi_2})^2]}\,\tanh \bar{y}_0 \sqrt{j\pi_2/\pi_3}}\,. \tag{89}$$

Clearly then

$$\lim_{\pi_3\to 0} \frac{\mathrm{d}\bar{B}_1(\bar{y}_0)}{\mathrm{d}\bar{y}} = 0 \tag{90}$$

(which is the condition Axford 8) used when $\pi_3 \ll 1$ in paramagnetic media) and when π_3 is small

$$\frac{\mathrm{d}\bar{B}_2}{\mathrm{d}\bar{y}} = \frac{\sqrt{j}\,\bar{U}_{01}\,\mathrm{e}^{-(\bar{y}_0-|\bar{y}|)\sqrt{j\pi_2/\pi_3}}}{\sqrt{\pi_3[\pi_1 + j(1+\sqrt{\pi_2})^2}}\,. \tag{91}$$

When

$$\bar{y} \equiv \pm\,\bar{y}_0,\ \lim_{\pi_3\to 0} \mathrm{d}\bar{B}_2/\mathrm{d}\bar{y} \to -\sqrt{j}\,\infty,$$

which indicates the presence of current sheets flowing on the surfaces of the oscillating plate. For $-\bar{y}_0 < \bar{y} < \bar{y}_0$, $\lim_{\pi_3 \to 0} \mathrm{d}\bar{B}_2/\mathrm{d}\bar{y} = 0$ and no current flows.

To illustrate the effect of plate conductivity on the velocity and magnetic field profiles figs. 2 and 3 are presented. For these calculations $\pi_2 = 0.1$, $\pi_1 = 0.1$, and $\omega = 36\,000\ \mathrm{s}^{-1}$. These constants are realizable in solar granulation. By (94) through (97) inclusive $\mathrm{Re}\, P_1 = 0.748$, $\mathrm{Im}\, P_1 = 0.6695$, $\mathrm{Re}\, P_2 = 0.21$ and $\mathrm{Im}\, P_2 = 0.235$. Plots of $|u_x/u_{x0}|$, $|\bar{B}_1/\bar{U}_{01}|$ and their phase angles versus $\bar{y}$ are given for $\pi_3 = 0$ and $\pi_3 = \infty$. The velocity profiles are compared to the classical profile when $B_0 = 0$.

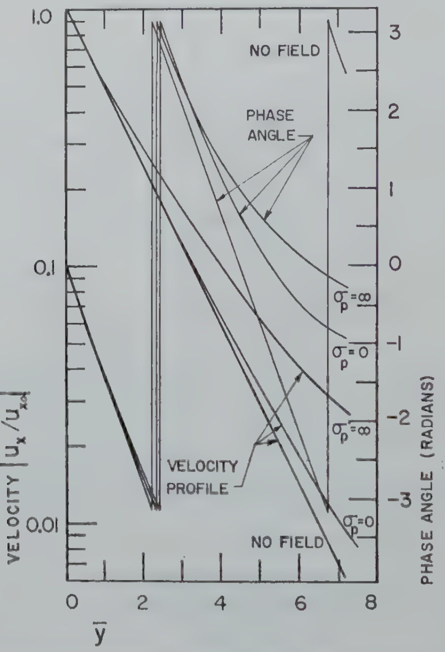

Fig. 2. Velocity profiles and phase angles for the oscillating plate.

§ 7. *Conclusions.* In the case of the perfectly conducting plate, oscillating between two conducting bodies, the plate drags the "frozen in" magnetic field along with it and causes a current to flow in the conducting bodies. The current is the same in magnitude and direction as would exist if the plate and magnetic field were fixed in space and the conducting bodies oscillated 180° out of phase with the original motion of the plate. The solution to the problem indicates that $\partial B_{x1}/\partial y \neq 0$ just outside the plate and that a current sheet flows in the surfaces of the plate. This current sheet allows the magnetic field to be discontinuous in the plate surface. In the interior $B_{x2} = 0$ as it must, so that infinite volume currents cannot flow.

When the plate moves with constant velocity through a conducting fluid, $\partial B_{x1}{}^*/\partial y|_{y0} = \mu_0 \sigma u_{x0} B_0$ in the fluid adjacent to the plate regardless of the plate conductivity.

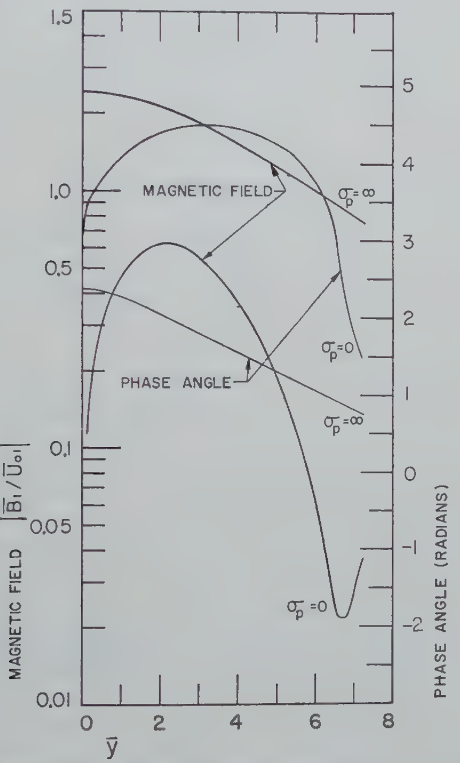

Fig. 3. Magnetic field profiles and phase angles for the oscillating plate.

For the case of a plate oscillating in a conducting fluid it is shown that the appropriate electrical boundary conditions are $dB_{x1}/dy|_{y0} =$ $= 0$ when the plate has infinite conductivity and $B_{x1}(y_0) = 0$ when the plate is an insulator. Current sheets in the surfaces of the perfect conducting plate which shield the interior of the plate from time varying magnetic fields have been discussed.

It is clear from figs 2 and 3 that the conductivity of the plate influences the velocity and magnetic field profiles. The effect is most pronounced for a plate of infinite conductivity. At large distances from the plate both the velocity and magnetic fields decay rather slowly. The decay is more rapid in the case of an insulating plate. For plates of finite conductivity it would seem that the velocity and magnetic field profiles fall between those of the above limiting cases. Such cases can be easily treated by the expressions derived here.

APPENDIX 1

Following Ludford's [3]) method (46) yields

$$P_1 = \tfrac{1}{2}[\sqrt{\pi_1 + j(1+\sqrt{\pi_2})^2} + \sqrt{\pi_1 + j(1-\sqrt{\pi_2})^2}], \quad (92)$$

$$P_2 = \tfrac{1}{2}[\sqrt{\pi_2 + j(1+\sqrt{\pi_2})^2} - \sqrt{\pi_1 + j(1-\sqrt{\pi_2})}], \quad (93)$$

$$\operatorname{Re} P_1 = \frac{1}{2\sqrt{2}}\left[\sqrt{\sqrt{\pi_1{}^2+(1+\sqrt{\pi_2})^4}+\pi_1}+\sqrt{\sqrt{\pi_1{}^2+(1-\sqrt{\pi_2})^4}+\pi_1}\right], \quad (94)$$

$$\operatorname{Im} P_1 = \frac{1}{2\sqrt{2}}\left[\sqrt{\sqrt{\pi_1{}^2+(1+\sqrt{\pi_2})^4}-\pi_1}+\sqrt{\sqrt{\pi_1{}^2+(1-\sqrt{\pi_2})^4}-\pi_1}\right], \quad (95)$$

$$\operatorname{Re} P_2 = \frac{1}{2\sqrt{2}}\left[\sqrt{\sqrt{\pi_1{}^2+(1+\sqrt{\pi_2})^4}+\pi_1}-\sqrt{\sqrt{\pi_1{}^2+(1-\sqrt{\pi_2})^4}+\pi_1}\right], \quad (96)$$

$$\operatorname{Im} P_2 = \frac{1}{2\sqrt{2}}\left[\sqrt{\sqrt{\pi_1{}^2+(1+\sqrt{\pi_2})^4}-\pi_1}-\sqrt{\sqrt{\pi_1{}^2+(1-\sqrt{\pi_2})^4}-\pi_1}\right], \quad (97)$$

and it can be shown that

$$P_1{}^2 P_2{}^2 = -\pi_2, \quad (98)$$

$$P_1{}^2 + P_2{}^2 = \pi_1 + j(1+\pi_2), \quad (99)$$

$$\gamma_1\gamma_2 = -j\pi_1\pi_2, \quad (100)$$

$$P_1\gamma_1 - P_2\gamma_2 = (P_1 - P_2)\, j(\pi_2 + \sqrt{\pi_2}), \quad (101)$$

$$P_1 - P_2 = \sqrt{\pi_1 + j(1-\sqrt{\pi_2})^2}. \quad (102)$$

Acknowledgement. The work underlying this paper was supported by a grant from the National Science Foundation.

Received 6th May, 1961.

REFERENCES

1) Rossow, V. J., Natl. Advisory Comm. Aeronaut., Tech. Note No. 3971, 1957.
2) Chang, C. C. and J. T. Yen, Phys. Fluids **2** (1959) 467.
3) Ludford, G. S. S., Arch. Rat. Mech. Anal. **3** (1959) 14.
4) Drake, D. G., Appl. Sci. Res. B **8** (1961) 467.
5) Greenspan, H. P., and G. F. Carrier, J. Fluid Mech. **6** (1959) 228.
6) Carrier, G. F. and H. P. Greenspan, J. Fluid Mech. **7** (1960) 22.
7) Hide, R. and P. H. Roberts, Rev. Mod. Phys. **32** (1960) 799.
8) Axford, W. I., J. Fluid Mech. **8** (1960) 97.

Appl. sci. Res. Section B, Vol. 9

ON THE EFFECT OF GRINDING UPON THE MAGNETIC PROPERTIES OF MAGNETITE AND ZINC FERRITE

G. W. VAN OOSTERHOUT and C. J. KLOMP

Natuurkundig Laboratorium N.V. Philips, Eindhoven, Netherlands

Summary

The dependence of the coercive force of magnetite upon grinding is investigated. The results of annealing experiments lead to the conclusion that the coercive force in this case is caused by stresses in the particles. This conclusion is supported by the results of similar experiments on ferrites having different combinations of crystalline anisotropy and magnetostriction. A semi-quantitative picture is given of the relation between H_c and the concentration of dislocations. The maximum concentration is estimated at 6×10^{14} m^{-2}. It is suggested that the results obtained here may be of use in the testing of grinding equipment and in investigations on grinding.

§ 1. *Introduction.* It is well known that the *coercive force* H_c of magnetite powders is strongly dependent upon their particle size. The literature on this topic has been reviewed by Wohlfarth [1]) in a recent paper. Increase of H_c of $NiMnO_3$ and $CoMnO_3$ on ballmilling has been described by Swoboda [2]). Similar effects have been found e.g. for MnBi by Guillaud [3]) and for MnAl by Koch *et al.*[4]).

A decrease of the *saturation magnetization* with particle size has been observed for iron and magnetite by Torkar, Scheikl and Egghart [5]). A similar phenomenon has been observed for $BaFe_{12}O_{19}$ by Torkar and Frederiksen [6]) and also for MnAl by Koch *et al.* [4]).

In Torkar's paper these effects are attributed to the increase of the volume of the supposedly non-magnetic surface-layer (Oberflächenraum) with decreasing particle size. As Wohlfarth remarks, this interpretation seems very doubtful in view of

Luborsky's [7]) results. Several other explanations are, however, possible:

1) For very small particles, superparamagnetism may occur, leading to a lowered saturation value if the maximum field-strength is too low. Of course this cannot account for an increased coercive force.

2) During the grinding process the particles can be deformed plastically. As a consequence some cations may be shifted to other lattice positions or get a different environment. According to Néel's theory [8]) this could lead to a change in saturation magnetization. This explanation has been suggested by Heister [9]) in the discussion of Torkar's paper. The lattice deformations could also account for the increase of H_c. If this last explanation holds, the possibility exists that the increase of the coercive force as well as the decrease of the saturation magnetization with decreasing particle size are *not particle-size effects at all.* They would then be due to very strong lattice deformations caused by cold-working during the grinding process. That the particle size also decreases, is a secondary effect.

Of course it is not denied that a real effect of particle size upon coercive force exists. But as far as we know at present, this does not occur for magnetite in the 10 micron size region, but much below 1 micron, at least for the non-elongated particles we are dealing with here. The purpose of this paper is to gather experimental evidence for this plastic deformation hypothesis and to show that the maximum coercive force obtained by grinding can be explained by it.

§ 2. *The change of the coercive force of magnetite on grinding.* Natural magnetite from Sweden having an initial $\mu_0 H_c$ *) of about 40×10^{-4} W/m² was ground in a 100 cm³ ballmill of the *rotating* type, made of steel and containing 3/16″ steel balls. Another sample of the same lot was ground in a 100 cm³ ballmill of the *vibrating* type, made of steel and containing 3/16″ "Stellite" balls. ("Stellite" is a non-magnetic alloy of Co–Cr–W–C). In all experiments the grinding medium was ethanol 96%. In these experiments the maximum particle size decreased from about 100 microns to less than 1 micron.

---

*) $\mu_0 = 1.256 \times 10^{-6}$ Vs/Am. M.K.S.-units are used throughout this paper. If the factor 10^{-4} in $\mu_0 H_c$ is dropped, the remaining figure represents the coercive force in Oersted.

For the coercive force measurements we used an apparatus described in a previous paper [10]). The samples consisted of an intimate mixture (1 : 1) of the magnetite to be investigated and urea. The latter served as a binding and lubricating agent. The mixture was moulded into small cylinders of 2 mm diameter and about 2 mm length.

The value of $\mu_0 H_c$ measured on the samples increases rapidly with grinding time in both cases and seems to go on to a saturation value of about 470×10^{-4} W/m². The results are reproduced graphically in fig. 1. From this it appears that H_c changes more rapidly in the vibrating mill than in the rotating one. This is in accordance with grinding experience from which we know that the vibrating mill has the stronger grinding action. Nevertheless the final value of H_c appears to be lower in the case of the vibrating mill. This is due to the higher temperature of the vibrating mill, accompanying the stronger grinding action, as will be explained in the next paragraph. It should be mentioned that we did not separate the powder into fractions of definite size-ranges before measuring H_c as Gottschalk [11]) and Torkar [5]) did. We measured H_c of the sample as it was obtained from the ball mill.

§ 3. *The effect of annealing on H_c of ground magnetite.* In order to investigate the presence of stresses in magnetite we performed a series of annealing experiments at different temperatures. The samples were heated in evacuated and sealed pyrex or quartz glass tubes to prevent oxidation of the magnetite. The first experiment was done with magnetite ground 19 hours, having a $\mu_0 H_c$ of 347×10^{-4} W/m². The sample was annealed at 500°C. The results are shown in table I. From sintering experience it is known that no sintering of magnetite occurs at this temperature. This has been checked for our powder by electron microscopy. The coercive force

TABLE I

Effect of annealing at 500°C on the coercive force of magnetite ground 19 hours in a vibrating mill

Annealing time (min)	0	10	23	60	120
$\mu_0 H_c$ (10^{-4} W/m²)	347	172	159	150	140

appears to change by more than a factor two without change in particle size. This shows clearly that the size of the particles is not the determining factor for H_c. In order to be completely certain that no sintering occurs we made a series of experiments at lower annealing temperatures. They showed that H_c changes even at 100°C. The results are given in table II.

TABLE II

Effect of annealing at different temperatures on the $\mu_0 H_c$ of magnetite, ground 120 h in a vibrating mill. The figures denote $\mu_0 H_c$ in 10^{-4} W/m^2.

Annealing temperature °C	Annealing time								
	0′	15′	30′	60′	120′	23 h	47 h	47 h	190 h
100	400	378		354		353			
200	400	288		266		267			
300	400	241		223		219	211	213	208
400	400	190	188	180	179				
500	400			130					
600	400			118					
700	400			110					
800	400			(sinters)					

A rather unexpected result was obtained from the following experiment. Natural magnetite, ground 120 h in a vibrating mill, having a $\mu_0 H_c$ of 400×10^{-4} W/m^2, was annealed in vacuo at 500°C. Grinding of this sample in a vibrating mill gave only a very slight increase of the coercive force as shown in table III. This result should be compared with that obtained after 18 h grinding in a vibration mill starting with a much coarser material and leading to a $\mu_0 H_c$ of about 350×10^{-4} W/m^2 (see fig. 1). This experiment shows that, contrary to common experience, a smaller particle size can lead to a lower H_c. A comparison of the X-ray powder diagrams of annealed and non-annealed samples clearly shows the effect of annealing upon line-width (table IV).

TABLE III

Effect of grinding upon the $\mu_0 H_c$ of magnetic ground 120 h and annealed at 500°C during 1 h

grinding time (h)	0	1 h	18 h
$\mu_0 H_c (10^{-4}$ W/m$^2)$	130	137	151

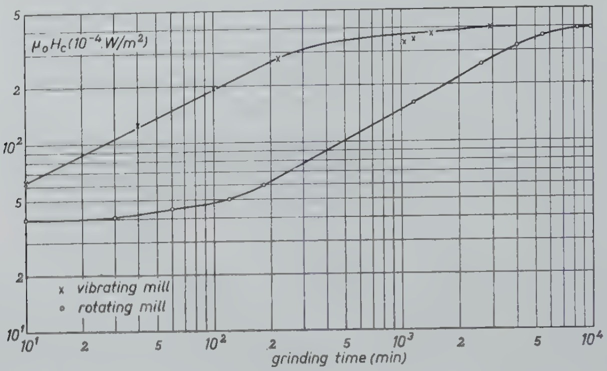

Fig. 1. Log-log plot of $\mu_0 H_0$ versus grinding time of natural magnetic from Sweden

TABLE IV

Effect of annealing on linewidth in X-ray powder diagrams of magnetite

hkl	Σh^2	line witdh (°θ)	
		annealed	not annealed
111	3	0.18	0.17
220	8	0.17	0.26
311	11	0.20	0.30
400	16	0.23	0.28
333, 511	27	0.26	0.40
440	32	0.32	0.45

§ 4. *The effect of grinding on the saturation of zinc ferrite.* As the effects of grinding on saturation magnetization are rather small and are easily obscured by the possible presence of superparamagnetism, we have not measured them for magnetite. Instead we have looked for a compound which would show the effect of cold working on saturation magnetization, if any, in an exaggerated form. Zinc ferrite $ZnFe_2O_4$ was supposed to be such a compound.

The saturation magnetization of well annealed zinc ferrite of stoichiometric composition is zero [13]). The sample which we prepared without special precautions had a saturation magnetization at room temperature of about 0.6% of that of Fe_3O_4. On grinding, the saturation magnetization increased to about 10% of that of Fe_3O_4. On annealing after grinding it decreased to practically its original value. In order to be certain that the increased saturation magnetization is not due to contamination with iron during the grinding process we ground the sample in a polyethylene ball mill containing 3/16″ "Stellite" balls. In separate experiments it was shown that TiO_2 and α–Fe_2O_3 *) did not give an increased saturation magnetization under the same conditions.

§ 5. *Discussion of the results.* Zinc ferrite and magnetite both have spinel structure. Therefore it is not too bold to assume that lattice imerpfections in both compounds will behave in a similar way. From the experiment on zinc ferrite we see that appreciable changes in the lattice may occur during the grinding process. Interchanging a number of zinc ions on tetrahedral sites will lead to a non-zero saturation magnetization according to Néel's theory. This in fact is the origin of the saturation moment of a quenched zinc ferrite [13]). It is not easy to understand, however, how such a shift may be induced by cold working. On the other hand it is known experimentally that cold working of magnetite leads to deformation twins on $\{111\}$ [14]). Gliding and deformation twinning of the spinel lattice have been investigated thoroughly from a purely geometrical point of view by Hornstra [15]). Unfortunately he did not investigate the cases where during the deformation a tetrahedral site changes into an octahedral site. This possibility was not excluded but was not investigated because it was thought unlikely. Analysis of the X-ray data for annealed and non-annealed ground magnetite suggests that the difference in line-width is probably due to strains in the particles. No indications have been found for deformation twinning on $\{111\}$ (cf. table IV). From the annealing experiments on magnetite it appears that we are dealing with rather unstable lattice defects that can be produced much more easily in large particles than in small ones. The instability is so great that annealing occurs even during the grinding process. Therefore the final coercive force is lower in the case where the temperature during grinding is higher (i.e. in the vibration mill).

On the other hand the coercive force of magnetite ground in a rotating mill (less intensive grinding action, therefore lower temperature) shows an aging phenomenon at room temperature. In a month $\mu_0 H_c$ decreases from 464×10^{-4} to 448×10^{-4} W/m², in another month to 447×10^{-4} W/m². It is not likely that twins would be so unstable. We suppose, therefore, that the main effect of grinding consists in an accumulation of dislocations in the particles, up to a maximum concentration determined by the temperature during the grinding process. This accumulation of dislocations makes the particles brittle, and they eventually break into smaller particles. When the particles are broken into small pieces after thorough grinding, they retain a high concentration of dislocations, but on annealing, the dislocations leave the crystal to a large extent. Grinding these small particles does not lead to the formation of new dislocations because the shearing action of the balls is less on small particles than on large ones.

---

*) The experiment with α–Fe_2O_3 was carried out at the suggestion of Dr. E. P. Wohlfarth (Imperial College, London) to see if it could be made ferromagnetic by grinding. This appeared not to be the case.

From the annealing experiments it is clear that crystalline anisotropy and shape anisotropy can only explain a small part of the observed H_c. The main part is thought to be due to stress anisotropy (or better, strain anisotropy). This assumption is supported by a comparison of the effect of annealing upon the coercive force of ground ferrites having different combinations of crystalline anisotropy and saturation magnetostriction.

TABLE V

The effect of annealing upon the coercive force of ground ferrites having different combinations of crystalline anisotropy (K_1) and magnetostriction (λ)

	K_1(J/m³)	λ	$10^4 \mu_0 H_c$	$10^4 \mu_0 H_c$ (after annealing)
Fe_3O_4	-110×10^2	$+40 \times 10^{-6}$	410	140
$NiFe_2O_4$	62×10^2	-26×10^{-6}	900	280
(Ni, Zn) ferrite	small	-5×10^{-6}	∼80	–
(Mn, Zn) (ferrite	small	-1×10^{-6}	∼80	–
(Ni, Cu, Co) ferrite	$\sim 2 \times 10^2$	-28×10^{-6}	770	120

From table V it appears that small λ and K_1 lead to a low H_c, and the data on (Ni, Cu, Co) ferrite show that small K can lead to a large value of H_c if λ is large. In order to explain the large coercive force we first remark that in this paper coercive force is neither an *average* value of some quantity as is usually assumed in the literature [16]) nor a *maximum* value [17]).

The coercive force we are using in this paper is the value of the external field – opposed to the field used to saturate the sample – needed to make the magnetization zero. In the situation of zero magnetization, one half of the magnetization is in one direction, the other half in the opposite one. Therefore the coercive force is that field strength at which one half of the magnetization has turned in the opposite direction. Assuming that the material is homogeneous with respect to the spontaneous magnetization, we have to explain why one half of the volume turns its magnetization below and the other half above H_c. Therefore we consider the material as being composed of a matrix of low coercive force material in which a heavily strained material is finely dispersed. Each dislocation is a "particle" of the heavily and inhomogeneously strained material. For a coercive force H_c one half of the volume of the material should have a stress $\sigma > H_c M_s/\lambda$ where M_s is the saturation magnetization and λ the saturation magnetostriction. Introducing the strain δ and Young's modulus E obeying $\sigma = E\delta$, we can say that one half of the material should have a strain $\delta > H_c M_s/\lambda E$ or $\delta > H_c/H_0$ with $H_0 = \lambda E/M_s$.

From dislocation theory [18]) it is known that at a distance r from the centre of a dislocation, which has a Burgers vector of length b, the strain is about $b/2\pi r$. If we have a dislocation density of $n m^{-2}$, the volume fraction having a strain $> \delta$ is about $n(b^2/4\pi\delta^2)$. This should be one half for $\delta = H_c/H_0$. Therefore $n = (2\pi/b^2)(H_c/H_0)^2$. Substituting the values for magnetite: $M_s = 0.6$ W/m^2, $\lambda = 40 \times \times 10^{-6}$, $E \approx 10^{11}$ N/m^2, $b = \frac{1}{2}a\sqrt{2}$ [15]) with $a = 8.3 \times 10^{-10}$ m and $\mu_0 H_c = 480 \times 10^{-4}$ W/m^2, we find $\mu_0 H_0 = 84.000 \times 10^{-4}$ W/m^2 and $n \approx 6 \times 10^{14}$ m^{-2}. This is the number of dislocations needed to explain the maximum observed H_c. It compares very well with the figure 10^{16}m^{-2} found in literature for the maximum concentration of dislocations in heavily strained metals.

It should be stressed that the role of dislocations in our explanation of H_c is essentially different from that in Kerstens' [19]) theory. In the latter theory they serve as obstacles to the motion of the Bloch walls even if their volume should be negligible. In our picture the effect of the dislocations depends essentially on their finite extension.

§ 6. *Conclusions.* From the results obtained in this paper it appears that the coercive force of magnetite powders is not a unique function of particle size, and it is made plausible that strains inside the grains are an important factor determining H_c.

In investigations on the dependence of coercive force on particle size the effect of these strains should be eliminated by annealing experiments. From the simple semi-quantitative picture given here it follows that the coercive force is proportional to the square root of the dislocation density. Assuming that this relation holds, we arrive at the simple result that for vibration milling the dislocation density is proportional to the grinding time. The results obtained here have a possible application in the field of research on grinding and in the testing of grinding equipment.

Acknowledgement. Finally it is a pleasure to thank Mr. J. Hornstra of this laboratory for his helpful discussions on dislocation theory and Dr. E. P. Wohlfarth, of Imperial College, London, for his valuable suggestions and for the opportunity he offered one of us to discuss part of the experimental work of this paper with a small group of interested people.

Received 29th March, 1961

REFERENCES

1) Wohlfarth, E. P., Adv. Physics **8** (1959) 87.
2) Swoboda, T. J., R. C. Toole and J. D. Vaughan, J. Phys. Chem. Solids **5** (1958) 293.
3) Guillaud, C., Thesis, Strassbourg 1943.
4) Koch, A. J. J., P. Hokkeling, M. G. van der Steeg and K. J. de Vos, J. Appl. Phys. **31** (1960) 75S.
5) Torkar, K., O. Scheikl and H. Egghart, Arch. Eisenhüttenw. **29** (1958) 139.
6) Torkar, K. and O. Frederiksen, Powder Met. 1959, No. 4 p. 105.
7) Luborsky, F. E., Phys. Rev. **109** (1958) 40.
8) Néel, L., Ann. Phys., Paris **3** (1948) 137.
9) Heister, W., see ref. 5).
10) Oosterhout, G. W. van, Appl. sci. Res. B **6** (1956) 101.
11) Gottschalk, V. H., Physics **6** (1935) 127.
12) Snoek, J. L., New developments in ferromagnetic materials, Amsterdam 1947.
13) Brockmann, F. C., Phys. Rev. **77** (1950) 841.
14) Grün, A., Neues Jb. Mineralogie 1918, p. 99.
15) Hornstra, J., J. Phys. Chem. Solids **15** (1960) 311.
16) Kersten, M., Grundlagen einer Theorie der ferromagnetischen Hysterese und der Koerzitivkraft, Leipzig 1944, p. 6.
17) Bozorth, R. M., Ferromagnetism, New York 1951, p. 824.
18) Cottrell, A. H., Dislocations and plastic flow in crystals, Oxford 1953.
19) Kersten, M., Z. angew. Phys. **8** (1956) 496.

Appl. sci. Res. Section B, Vol. 9

THE EFFECT OF MOISTURE ON THE DIELECTRIC CONSTANT OF HARDENED PORTLAND CEMENT PASTE

by G. P. DE LOOR

Physics Laboratory R.V.O.–T.N.O., Waalsdorp, The Hague, Netherlands

Summary

Measurements are reported of the dielectric constant of hardened portland cement paste as a function of water content between 0.1 and 10 MHz and at microwave frequencies at 3000, 3750, 7450 and 9375 MHz. The dielectric losses observed seem to be conductivity losses (capillary water, adsorbed water) at the lower frequencies, whereas at microwaves they seem to be due primarily to the relaxation of the free or capillary water in the pores.

§ 1. *Introduction.* Stimulated by a suggestion of the Institute T.N.O. for Building Materials and Building Structures in Delft – furtheron to be indicated as I.B.B.S. – a series of experiments was undertaken to determine the dielectric properties of hardened portland cement paste at microwave frequencies. To gain a deeper insight into the general dielectric behaviour of a cement as a function of the absorbed water a series of measurements between 0.1 and 10 MHz was also included. The present paper is a brief review of the results obtained.

§ 2. *The samples.* As the production process can influence the result, a brief description of the preparation of the samples used will be given first. Four disc-shaped samples (labelled A, B, C and D) were prepared by the I.B.B.S. of a portland cement A (of the ENCI) with water/cement ratios of 0.26 (A and B) 0.31 (D) and 0.36 (C). The data of the cement used were: chemical composition: C_3S 60.1%, C_2S 14.4%, C_3A 10.1%, C_4AF 8.6%, in which C stands for CaO, S for SiO_2, A for Al_2O_3 and F for Fe_2O_3; true density: 3.15 g/cm^3; specific surface (Blaine) 2980 cm^2/g; Vicat initial set 3 h, Vicat final set 4 h 50 min., 26.1% water.

The four samples were made in a closed mold in which they remained for one day and were further cured under water for one month (sample A for seven weeks). After this period the samples were dried in an oven for about ten days at a temperature of about a 100°C and put in a desiccator over P_2O_5 for another week and until the measurements. After these measurements they were left in the laboratory atmosphere ($t \sim 20$°C, relative humidity 50–70%), and their dielectric constant and the amount of absorbed moisture were determined at intervals. To obtain higher water contents the samples were wetted with distilled water. This procedure of drying and rewetting was repeated a few times. In the measurements reported the age of the samples is given. This is the time elapsed since their preparation.

The four samples were about 3.60 cm in diameter and 0.65 cm thick. They contained a hole at the centre to fit them into our coaxial measuring equipment. Their dielectric constant was determined between 0.1 and 10 MHz and at 3000 and 3750 MHz.

A fifth sample (sample E, w.c. ratio 0.24), smaller in size (~ 1.4 cm^3) was made in an open mold and cured in the laboratory atmosphere. Its dielectric constant was determined at 7450 and 9375 MHz.

§ 3. *Measuring equipment.* The dielectric constant of a lossy material can be written as [1]) $\tilde{\varepsilon} = \varepsilon' - j\varepsilon''$, with $\operatorname{tg} \delta = \varepsilon''/\varepsilon'$. The losses represented by ε'' or $\operatorname{tg} \delta$ are due to conductivity or relaxation phenomena.

Between 0.1 and 10 MHz the dielectric constant of the specimens was measured with the aid of a condenser consisting of two circular flat electrodes, 50 mm in diameter, whose capacity was determined with the specimen in position between the plates and with the specimen taken out, keeping the electrodes of the condenser at the same distance. The measurements were made with an apparatus based on the heterodyne-beat method. In the procedure described, difficulties arising from an unknown edge correction are avoided because the specimens are smaller in diameter than the electrodes and are confined to that part of the space between the electrodes where the field is parallel and uniform. To eliminate the influence of an air gap of unknown thickness between electrodes and sample secondary electrodes were painted on the specimens by means of a silver paint. The value of ε' was determined with an accuracy of about 0.5 to 1%, that of ε'' with an accuracy of 1 to 4%.

At 3000 and 3750 MHz the dielectric constant of the samples A, B, C and D was determined in a coaxial waveguide system. With the method described by Von Hippel [2][3]) the impedance of the sample was determined. For a further calculation of the dielectric constant the method of Benoit [4]) and Poley [5]) was used. The value of ε' can be determined with an accuracy of about 2%, that of ε'' with an accuracy of 4 to 5%, but occasionally larger deviations in ε'' occurred.

The same methods were applied at 7450 and 9375 MHz where a rectangular waveguide system was used.

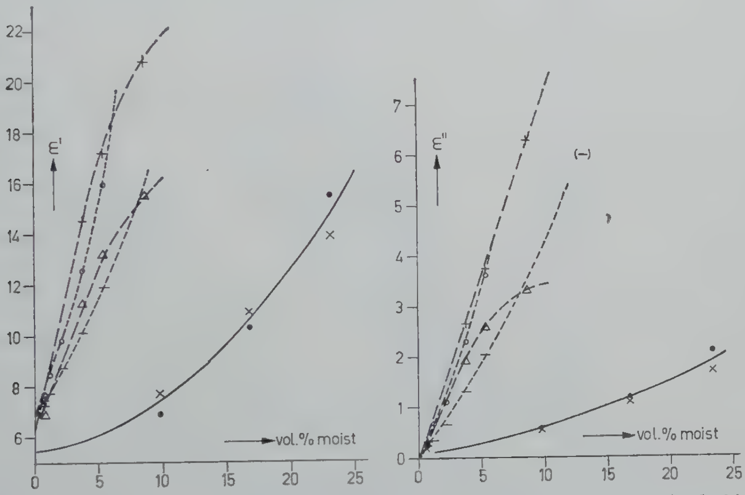

Fig. 1. Sample D. Dielectric constant *vs* moisture content (vol. %); ● 3000 MHz, × 3750 MHz, age 3 months; + 0.1 MHz, △ 1 MHz, age 2 months; ○ 0.1 MHz, — 1 MHz, age 1 year.

§ 4. *Measuring results.*

4.1. Measurements between 0.1 and 10 MHz. The measurements of the dry samples were very difficult to make, as the specimens rapidly absorbed moisture, which influenced the measured dielectric constant enormously, as soon as they were taken out of the desiccator. The measurements were therefore corrected as far as possible back to the moment the samples left the desiccator. Fig. 1 gives ε' and ε'' as a function of moisture content

v (volume percentage) for material D. Sample D is chosen as an example, because it gives results about equivalent to the average of the results for the specimens A, B, C and D together. The curves for the other samples thus have the same form.

When plotting the measurements just mentioned (fig. 1) as a function, not of v, but of the apparent density it appears that the curves for the several frequencies intersect at one specific density which is lower than the one assumed for the dry sample, (see fig 2).

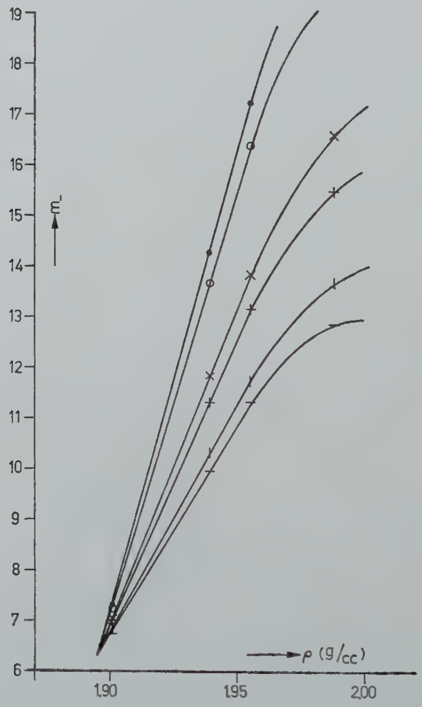

Fig. 2. Sample D. Dielectric constant *vs* apparent density. Age 2 months, ● 0.1, ○ 0.2, × 0.5, + 1, | 3, – 5 MHz.

Because of the rapid variation of the dielectric constant due to moisture absorption it was assumed that the samples were not absolutely dry during the measurement, even after correction, and that the density found for the intersection point is the actual density of the dry sample, dry meaning: the specimen has lost its evaporable water, but held its non-evaporable water ⁶). Using the dry density thus obtained the percentage of absorbed moisture (v: volume percentage, g: weight percentage) was determined. (fig. 2).

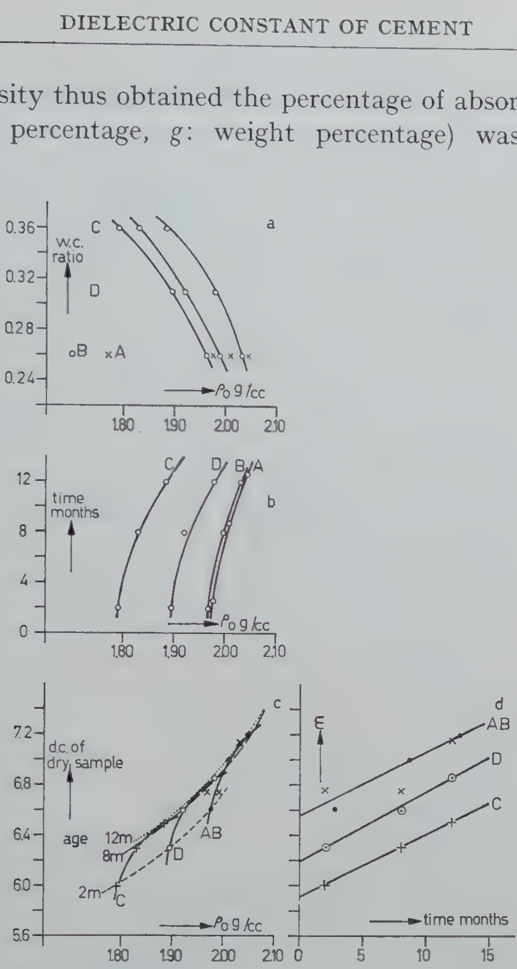

Fig. 3. Properties of the dry samples A, B, C and D.

In fig. 3 all the results for the dry material are compiled. The density and ε' were determined as described above. ε'' is small (< 0.05). Because of the continuing curing process the samples attained a higher density as a function of time.

Extrapolation and calculation – considering the material as a heterogeneous mixture of cement and air – gives [7]) for the dielectric constant of the bulk material: $\varepsilon \approx 10.5$, assuming the density ρ of this bulk material to be $\rho = 3.15$ g/cm^3.

4.2. Microwave measurements. Measurements were performed between 2500 and 3750 MHz. The measurements met with trouble because of sample fitting (shrinkage after drying, etc.) and other mechanical difficulties.

The results for the specimens A, B, C and D are most trustworthy at 3750 and 3000 MHz. For sample D they are introduced in fig. 1.

The waveguide measurements at X-band on sample E are also more reliable. They are reported in fig. 4.

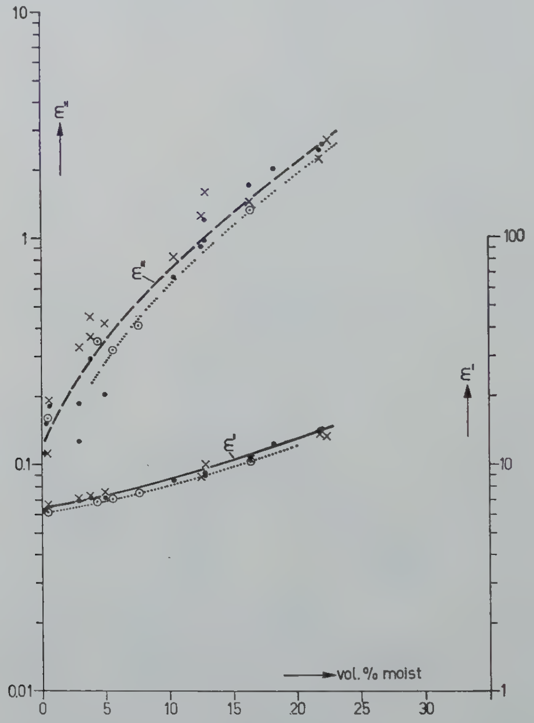

Fig. 4. Sample E. Dielectric constant *vs* moisture content (vol. %); ○ 9375 MHz, age 2 months; × 7450 MHz, ● 9375 MHz, age 8 months.

§ 5. *Discussion.*

5.1. Frequency range 0.1 to 10 MHz.

5.1.1. The thing which first catches the eye when looking at the curves of ε' and ε'' as a function of v in fig. 1 is the rapid increase of both ε' and ε'' in this frequency region as a function of moisture content for the lower values of v. For a younger sample (age 3 months) a change occurs in the curves between a volume percentage of moisture between 5 and 7. This is about the percentage at which the first layer of water molecules adsorbed on the pore walls is completely filled 6).

The increase of ε' and ε'' as a function of moisture content is less for higher frequencies, but the decrease of ε'' as a function of frequency for a cement with a fixed water content is less than can be expected from the conductivity of the sample as a whole. In that case $\varepsilon'' = 4\pi\sigma/\omega$, with σ the conductivity of the sample and ω the circular frequency. Making a plot $\varepsilon'' = f(\varepsilon')$ (Cole-Cole diagram) for this frequency region we obtain very flat curves; see fig. 5. Although it is not the author's intention to give a full description of the phenomena occurring in cement which may lead to an explanation of the shape of the curves of fig. 5 and of the slow decrease of ε'' as a function of frequency, some remarks can be made which may contribute to an elucidation of the macroscopic dielectric behaviour of cement. In the frequency range under discussion one has to take into account the following three effects:

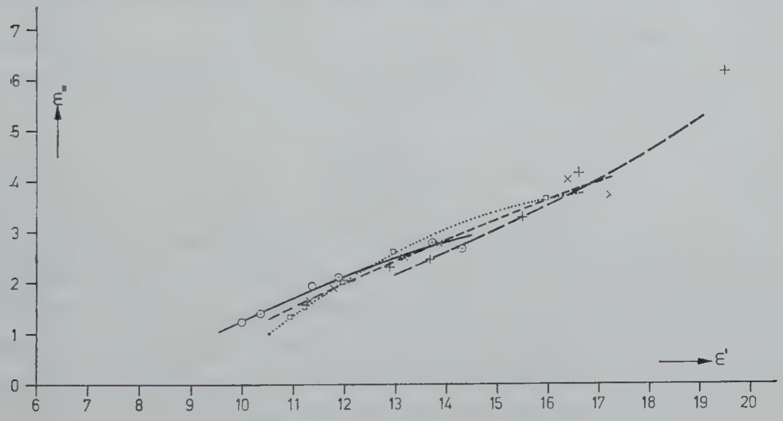

Fig. 5. Sample D. $\varepsilon'' = f(\varepsilon')$. ○ $g = 2.32\%$, × $g = 3.14\%$, + $g = 4.9\%$, age 2 months; □ $g = 2.72\%$ age 1 year.

5.1.1.1. The conductivity of the samples as a whole (direct conductivity through the water in the pores).

5.1.1.2. The Maxwell-Wagner losses. These losses occur in a heterogeneous mixture consisting of two materials having a different conductivity. It is a typical low-frequency phenomenon, but it can extend into the frequency region under discussion. Sillars 8) showed that the curves $\varepsilon' = f(\varepsilon'')$ become flattened when the inclusions have an ellipsoidal shape [9]). In a cement all kinds of shape occur. Hamon [10]) confirmed Sillars findings and showed also that for a dielectric consisting of non-conducting spheroidal particles with surface conducting layers no absorption maximum is found as a function of frequency. The dielectric loss is more or less proportional to $f^{-\alpha}$ (f = frequency) with $0 < \alpha < 1$. To this effect Nelson *et al* [11]) refer in order to explain the loss observed by them in magnesium hydroxide, which showed the above mentioned dependence upon frequency. In essence the above is the same as the following effect described by O'Konski.

5.1.1.3. O'Konski [12]) pointed at the fact that the electric phenomena associated with a surface layer can include a two-dimensional surface conductivity. Such a conductivity can occur in systems in which the mobilities of charge carriers are large along the surface but small normal to it. It seems reasonable to assume such phenomena to be present here. In our case this means that at low frequencies the pore, because of the adsorbed water layer, acts as a conducting inclusion (high conductivity along the pore walls). Assuming such an inclusion to be ellipsoidal in shape its polarization in the a-direction can be written as [1])[7])

$$\alpha_a = \frac{\varepsilon_c}{A_a} \frac{abc}{3}$$

with ε_c the dielectric constant of the bulk material (cement), A_a the depolarization factor of the inclusion in the a-direction and a, b and c the semi-axes of the ellipsoidal pore, whereas at high frequencies where the mobility of the charge carriers becomes too low to follow the alterations of the field

$$\alpha_a = \frac{1}{3} abc \, \frac{\varepsilon_c(1 - \varepsilon_c)}{\varepsilon_c + (1 - \varepsilon_c) A_a} .$$

For the intermediate region we calculated the polarizability for *spherical* inclusions with radius R and obtained

$$\alpha = \varepsilon_c R^3 \left(\frac{1 - \varepsilon_c}{1 + 2\varepsilon_c} + \frac{P}{Q} \right)$$

with $P/Q = k_1/(1 + j\omega\tau_1)$, where

$$k_1 = \frac{3\varepsilon_c}{1 + 2\varepsilon_c}, \quad \tau_1 = R \frac{1 + 2\varepsilon_c}{8\pi\Delta\sigma} ,$$

with Δ the layer thickness and σ its conductivity (in e.s.u.). Thus τ_1, the macroscopic relaxation time, is a function of pore size. Further calculations on spherical inclusions taught that a distribution of pore sizes flattens the Cole-Cole arc. The same can be expected for a distribution of eccentricities, assuming the pores to be ellipsoidal. Both are present in a cement.

When a cement ages, the pore shape and size change [6]). This must have some influence on the measuring results. Fig. 5 shows for sample D that there is a slight difference between the curves for a sample three months old and the same sample twelf months old.

The effects described above can ,at least qualitatively, explain the flat curves $\varepsilon' = f(\varepsilon'')$. On the other hand it may be necessary to take into account the possibility of water of an intermediate phase – intermediate between the bound water and the free water [13])[14]).

5.1.2. The influence of the water of crystallization can probably be excluded in the above discussion. Working at a frequency of 2 MHz Cheng [15]) demonstrated on a series of metallic sulphates, comparable to those occurring in cement and containing various amounts of water of crystallization, that the molecular polarization of the water in the salts is practically constant and only slightly higher than that of ice. This would mean that the relaxation frequency of the water of crystallization is shifted to much lower frequencies than under discussion here.

Another point in Cheng's measurements is that the dielectric constant of the salts decreased for a higher content of water of crystallization. This would mean that when hydratation proceeds, the dielectric constant of the dry bulk material – the specimen still holding its non-evaporable water [6]) – (now found to be $\sim$10.5) will decrease. Our measurements are not conclusive about this subject but suggest it: see fig. 3*c*. In this figure we plotted the dielectric constant of the dry cement as a function of the dry density. The increasing dry density of the cement and the changing of the pore to a more rounded shape [6]) as a function of time tend to increase the dielectric constant [7]) of the cement/air mixture. The inflexion of the curves $\varepsilon = f(\rho)$ for the samples A, B, C and D can now be ascribed to the lowering of the dielectric constant of the bulk cement because of the proceeding hydratation.

Further work in this field might be useful to get more information on the status of the hydratation process. The effect can be spoiled, however, because prolonged drying over P_2O_5 can result in some dehydration of the salts in hardened cement paste [6]). On the other hand it is not certain whether all the adsorbed water – tightly bound to a surface as it can be – is removed by the drying process used.

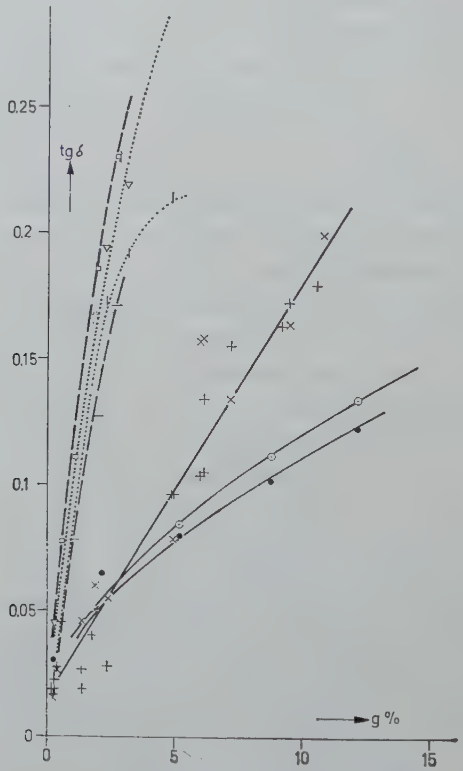

Fig. 6. Samples D and E. tg δ *vs* moisture content (weight %). Sample D: ▽ 0.1 MHz, | 1 MHz, age 2 months; □ 0.1 MHz, — 1 MHz, age 1 year; ● 3750 MHz, ○ 3000 MHz, age 3 months. Sample E: △ 9375 MHz, age 2 months; + 9375 MHz, × 7450 MHz, age 8 months.

5.2. Microwave frequencies. The results of the measurement in this frequency range are included in the figs 1 and 4. In fig. 6 all the measurements on the samples D and E are compiled by plotting tg $\delta = f(g)$, where g is the weight percentage of moisture in the dry sample. It is seen that tg δ first decreases as a function of frequency for all moisture contents and begins to increase again in the microwave region. This suggests that a new phenomenon starts in this region.

Water shows relaxation at microwave frequencies [16]), and ε'' plotted as a function of ε' gives a semi-circular arc [1]) (Cole Cole arc [17])). Ref. [7]) shows that the Cole-Cole plot of a heterogeneous mixture of which one of the components shows relaxation – with properties which can be plotted on a semi-circular Cole-Cole arc – also will be a semi-circle, or at least nearly so, with the relaxation time *) shifted to shorter times (higher frequencies). This, and a close study of all the available measurements led us to assume that each point measured in this frequency range lies on a semi-circle when plotting $\varepsilon'' = f(\varepsilon')$, each circle belonging to one fixed moisture content. Thus for each measurement the relaxation time was determined. The values found were of the same order as for water, with a tendency to be a little smaller. This is in agreement with ref. [7]) and also with the fact that inorganic ions in water tend to shorten its relaxation time [18]).

The above suggests that the free water (or capillary water, ref [6]), p. 252) is the primary cause of the losses shown by wet cement at microwave frequencies. Water in bound form (water of constitution [6]), adsorbed water) usually has a much longer relaxation time.

§ 6. *Conclusion.* It can be concluded that the dielectric losses in moist hardened cement paste are primarily conductivity losses – conductivity of the cement as a whole (capillary water) and the conductivity of interfaces (adsorbed water) – at frequencies between 0.1 and 10 MHz while at microwave frequencies the losses seem to be primarily due to the free water in the pores.

Acknowledgement. The author thanks the director of the Physics Laboratory R.V.O.–T.N.O. for his permission to publish this study. He is indebted to Mr P. C. Kreijger of the Institute T.N.O. for Building Materials and Building Structures for suggesting the problem and for his continued interest.

Received 10th May, 1961.

---

*) Relaxation time as determined from the frequency or wavelength belonging to the maximum of the Cole-Cole arc.

REFERENCES

1) Böttcher, C. J. F., Theory of electric polarisation, Elsevier, Amsterdam, 1952.
2) Roberts, S. and A. R. von Hippel, J. Appl. Phys. **17** (1946) 610.
3) Hippel, A. R. von, Dielectric materials and applications, Wiley, New York, 1952.
4) Benoit, J., Ann. Télécomm. **4** (1949) 27.
5) Poley, J. Ph., Appl. sci. Res. B **4** (1954) 173.
6) Powers, T. C., and T. L. Brownyard, Studies of the physical properties of hardened portland cement paste, Bulletin nr. 22 of the Portland Cement Association, Chicago, 1948. Reprinted from: J. Am. Concrete Inst., Oct. 1946 through April 1947, Proceedings, vol. 43, 1947.
7) Loor, G. P. de, Dielectric properties of heterogeneous mixtures, thesis Leiden 1956; ed. Excelsior, The Hague, 1956.
8) Sillars, R. W., J. Instn. Elect. Engrs **80** (1937) 378.
9) Wood, J. L., Brit. J. Appl. Phys. **10** (1959), 404.
10) Hamon, B. V., Austr. J. Phys. **6** (1953) 304.
11) Nelson, S. M., A.C.D. Newman, T. E. Tomlinson and L. E. Sutton, Trans. Faraday Soc. **55** (1959) 2186.
12) O'Konski, C. T., J. Chem. Phys. **23** (1955) 1559.
13) Palmer, L. S., Proc. Phys. Soc. B **65** (1952) 674.
14) Palmer, L. S., A. Cunliffe and J. M. Hough, Nature **170** (1952) 796
15) Cheng, C. K., Phil. Mag. **30** (1940) 505.
16) Poley, J. Ph., Appl. sci. Res. B **4** (1955) 337.
17) Cole, K. S., and R. H. Cole, J. Chem. Phys. **9** (1941) 341.
18) Haggis, G. H., J. B. Hasted and T. J. Buchanan, J. Chem. Phys. **20** (1952) 1452.

DESCRIPTION OF A 30 cm-H_2-BUBBLE CHAMBER

by J. REUSS, D. Z. TOET and B. VAN EIJNSBERGEN

Communication No. 332*a* from the Kamerlingh Onnes Laboratorium, Leiden, Nederland

Summary

A detailed description of a 30 cm-H_2-bubble chamber is given. The simple cooling system, the expansion mechanism, which transfers the work under tension, the use of a tomback-expansion-bellows at liquid hydrogen temperatures, and the illumination system are unconventional.

Introduction. Starting in 1957 a H_2-bubble chamber was constructed and has been tested in several runs. It is a chamber with one horizontal window on top, a bellows for expansion at the bottom, a total volume of 19 l and a useful volume of 14 l.

The following represents an account of the work done and the experience gained during the years of construction and tests.

In chapter I general bubble chamber problems will be discussed in order to prepare the background, against which the special features of our chamber should be seen. The sections will deal with the general technique, the formation of bubbles, the guiding principles for the design, the accuracy of track location and the possibilities of a H_2-bubble chamber.

In chapter II a detailed description of all aspects of our chamber design will be given, with exception of the optical system. The general design, the mechanical construction, the cooling system and the expansion system will be treated.

The description of the optical system of our chamber will cover a relatively large part of this account. We shall discuss a special way to avoid disturbing reflections in a one-window-chamber, following a suggestion of Courant [14]). In the sections of chapter III the components of our optical system, bubble and source images, the illumination system and experiences with the flash lamp will be described.

CHAPTER I

GENERAL PROPERTIES AND POSSIBILITIES OF H_2-BUBBLE CHAMBERS.

§ 1. *On the general technique.* In 1952 D. A. Glaser [1]) proposed the bubble chamber as a new instrument of high energy physics. It was designed to meet the urgent demand for visible detection of fast particles produced in all the many accelerators which have recently come into being. The general idea of a bubble chamber is very simple. A superheated liquid starts to boil when disturbances are present. Fast moving charged particles can create such disturbances.

In § 2 we shall give a short discussion on the formation of bubble tracks. At this point it is sufficient to state that a chain of bubbles appears shortly after a charged particle has passed through the superheated liquid.

The chamber remains sensitive for bubble formation for a certain time only, because the superheated condition is unstable. The intention is to get the liquid back into the sensitive state at each synchrotron pulse. The whole working cycle runs as follows: The chamber liquid has a certain temperature T_0 and is pressurized slightly above its vapor pressure. To get it into the superheated condition the pressure in the liquid is suddenly decreased below the vapor pressure belonging to T_0. This is done either by enlarging the liquid volume in the case wherein no vapor phase exists in the then entirely closed chamber volume, or by expanding the vapor above the liquid in the case wherein the chamber is pressurized under a vapor phase. Now bubbles appear if "evaporation nuclei" are present.

The difficulty is that in the expanded state the liquid always starts boiling spontaneously. This causes the chamber pressure to rise until equilibrium between the liquid and the gas which boils off is reached. Then several minutes of recompression are required to re-establish the begin-conditions, because all of the evaporated gas has to be reliquefied. In order to reduce this time, a fast recompression is used before spontaneous boiling really starts. In the case of a hydrogen chamber, the total time during which the liquid is off pressure lies normally between 20 and 40 ms. Within this time the beam of particles must arrive, the bubbles have to grow to a visible size, and the flash has to work to get photographs of what has happened in the chamber. The repetition rate of expansion is normally ten per minute.

A bubble chamber may be used as a detector of particle tracks when one is interested in reactions for which the chamber liquid itself is merely of secondary importance. In this case heavy liquids have the advantage of a high stopping power. Furthermore, molecules of high Z-numbers have a short mean free path for gamma rays. There exist, for example, xenon chambers with a mean free path of 6.4 cm for 100 MeV-gammas, which must be compared with a mean free path of 27 m in liquid hydrogen. In heavy liquids, however, multiple scattering effects are much more important than in liquid hydrogen. They impede accurate measurements of the curvature of tracks in a magnetic field, a quantity related to the particle momenta.

In general it can be said, that reactions producing gamma rays should be studied in heavy liquid chambers whereas in nearly all other cases liquid hydrogen chambers are preferable. A hydrogen chamber can also be filled with liquid deuterium. For the particles from an accelerator both hydrogen and deuterium contain target nuclei with a simple structure only, i.e. protons and deuterons respectively. In investigating the production of particles it is essential for later interpretation that the incoming particles react with such simple nuclei.

From the above it becomes clear that a bubble chamber is a measuring device very similar to the well-known Wilson chamber, with the advantage that the density of its liquid is much higher than the density of the gas which fills a cloud chamber. Thus the mean free path of a particle is considerably shortened. In a high pressure hydrogen cloud chamber working at 30 atm and room temperature, the mean free path for a hydrogen event is a factor 20 larger than in a hydrogen bubble chamber.

The general features of a hydrogen bubble chamber are summarized in the following table:

temperature	T_0	$= 27$°K
pressure before expansion	p_0	$= 5.5$ atm abs.
pressure drop during expansion	Δp	$= 3$ atm
relative volume change during expansion	$\Delta V/V$	$= 0.01$
average size of a bubble	d	$= 200\ \mu$
time of bubble-growth	Δt	$= 1$ ms
number of bubbles/cm on a typical track	n	$= 15\ \mathrm{cm}^{-1}$
total time chamber is off pressure	$\Delta\tau$	$= 25$ ms
repetition rate	ν	$= 1\ \mathrm{s}^{-1}$
density of hydrogen	ρ	$= 0.059\ \mathrm{g.cm}^{-3}$
density of protons	N	$= 3.5 \times 10^{22}\ \mathrm{cm}^{-3}$

§ 2. *Bubble formation.* The formation of bubbles is still an open field in physics, as well for theoreticians as for experimentalists. Some new problems arise if one tries to understand the appearance of tracks in a bubble chamber. The fundamental question is, what does the passing charged particle do to the liquid so that a chain of bubbles is formed along its path. A further question is, how do the bubbles behave, once they are formed. Here one can apply the methods and formulas of the theory on the kinetics of boiling.

Glaser was the first to attack the fundamental question. He suggested that the electrostatic forces of ions were mainly responsible for the formation of bubble tracks in superheated liquids. Ions are created along the path of a charged particle. This point of view is similar to the normal treatment of droplet formation in a Wilson chamber.

In a superheated liquid a spherical bubble of a radius $r_c = 2\sigma \cdot (p_v - p_h)^{-1}$ is stable; p_v denotes the pressure inside the bubble and p_h the hydrostatic pressure in the liquid. r_c is called the critical radius. It is assumed that p_v equals the vapor pressure of the liquid. In a bubble with $r = r_c$ the overpressure $p_v - p_h$ inside the bubble is balanced by the surface tension σ. The surface tension causes a bubble to collapse if r is smaller than r_c, the overpressure forces a bubble to grow if r is larger.

The presence of a cluster of charged particles inside a bubble changes the situation. The repulsive force of charges of equal sign forbids a total collapse. Also with no overpressure inside a bubble there is a critical radius, at which the surface tension balances the electrostatic forces. Bubbles with $r = r_c$ are in real equilibrium, as all smaller ones tend to grow and all larger ones start to contract. With overpressure this critical radius increases, until at a certain value of $p_v - p_h$ all bubbles become unstable and begin to grow. This value of $p_v - p_h$ depends on the number of charges n inside the bubble. Glaser derives for it $(n \geqslant 2)$ $p_v - p_h = 5.62 \cdot \sigma^{4/3} \cdot \cdot E^{1/3} \cdot n^{-2/3}$. Here E is the dielectric constant of the liquid; the surface tension σ is measured in dynes/cm and the pressure p_v and p_h in atm.

With this expression the working conditions of most chamber liquids have been successfully predicted, assuming $n = 6$. The fundamental question, however, is only shifted thus far and not answered.

The existence of a cluster of charges with equal sign seems rather improbable in a liquid. The situation is very different from what one encounters in a Wilson chamber. There the occurrence of a single charge in a droplet produces a surface charge on the liquid-vapor interface as a consequence of the different polarization in the two phases. Normally the dielectric constant of the liquid is larger than that of the vapor. Therefore the surface charge has the same sign as the single charge inside the droplet. When the droplet is contracting, work must be done to bring the surface charge and the single charge nearer to each other. Therefore the same happens as in the case of a charge cluster inside a bubble. All droplets containing one single charge grow to macroscopic size if the difference between the chamber pressure and the vapor pressure exceeds a critical value.

In bubble chambers the difference between the dielectric constant of the liquid and the vapor works the wrong way if it is not negligible. Therefore one is forced to assume several charges of equal sign in a bubble if the electrostatic forces are responsible for the formation of bubbles.

In the handbook article on bubble chambers [1]) Glaser himself presents a series of arguments which make the electrostatic approach doubtful. Instead of repeating these here we only mention the total failure of the theory in explaining the behaviour of xenon. Pure liquid xenon could not be sensitized by expansion; when however, 2% ethylene was added, bubbles could be observed [1]).

In 1958 F. Seitz published an investigation concerning the possible connection between radiation damage in semi-conductors and bubble formation [2]). He considered knock-on-electrons as responsible for the occurrence of hot spikes in both cases. These electrons give off their kinetic energy over very short distances. In a superheated liquid, bubbles will grow explosively during 10^{-10}–10^{-11} s, before this heat accumulation disappears by conduction. With a final radius larger than the critical one they will have consumed the surplus of thermal energy inside the hot spike. In hydrogen under normal working conditions of bubble chambers the critical radius is about 10^{-7} cm. Once grown so far, the overpressure inside a bubble tends to increase its size further.

Seitz gives some estimates in his paper showing the physical possibility of this explanation. Although the way in which the results are derived may be criticized, the underlying picture is generally accepted today.

The fact, that the behaviour of xenon finds a natural explanation favours this approach. Actually his experience with xenon led Glaser independently to the conception of rather the same mechanism of bubble formation. His guess that liquid xenon is a good scintillator is now confirmed experimentally. The xenon atoms which are excited by a fast ionizing particle will therefore loose their energy mainly by radiation. Addition of hydrocarbons or other quenching materials with many internal degrees of freedom brings about the possibility of converting the radiation energy into thermal energy. Thus also in liquid xenon a hot spike can be formed.

Experimentally little work has been done to clarify the situation. Feasibly strong electric fields would not influence the position of bubbles if they contained electrical charges. The flow resistance is too large and the time of growth too short for the bubbles to show displacements comparable to their diameters. Therefore, no indication can be expected from the application of electrical fields as to whether electrostatic forces play a role in bubble formation.

However, experiments have been performed with the aim of searching for a change in bubble density by action of an electrical field [3]). The magnitude of the used field of 15 kV/cm was supposed to be high enough to extract electrons out of a hot spike before a bubble assumes its critical size. Thereby recombination should be delayed. No measurable effect was found. It may be concluded, that either the heat of recombination is of minor influence on the formation of bubbles or that the recombination time is considerably shorter than 10^{-11} s, the time a bubble needs to grow to its critical size.

§ 3. *Guiding principles for the design of a hydrogen bubble chamber.* In this section we want to discuss some general points which determine the design of a bubble chamber by their relative importance.

The chamber volume must be illuminated and photographed to record what happens when a beam of particles is shot through. Use is made of the light scattering on the bubbles which mark the paths of the fast particles.

This scattering is mainly due to refraction effects. In principle both, bright field and dark field illumination are possible for photographing the bubbles. In the first case the camera has to be placed in the path of the direct light, so that a decrease in light intensity can be seen. In the second case the camera receives the light which is scattered on a bubble, and the direct light is kept away. In practice the dark field illumination is generally preferred because of its better contrast.

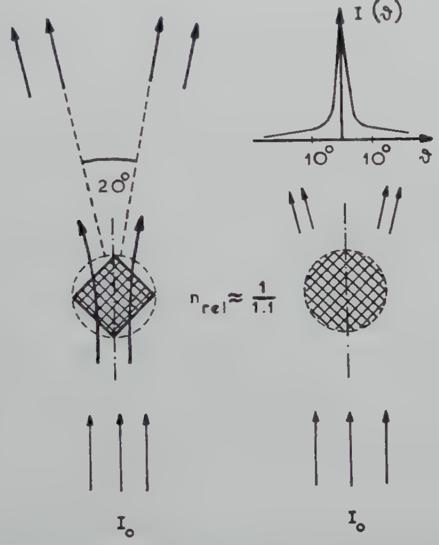

Fig. 1. Light scattering by bubbles. On the left a bubble is replaced by a double cone. n_{rel} is the refractive index between gaseous and liquid hydrogen at working conditions.

The distribution of the scattered light imposes some restrictions on a designer. By the following argument, one can get an idea of what the angular distribution looks like. Let us roughly approximate a bubble by a transparent double cone with its axis parallel to the incident light, as shown in fig. 1. A section through the cone axis should be a square with $\sqrt{2}$ times the bubble radius. Parallel light which falls on this double cone leaves it after being twice refracted at a fixed angle to the cone axis. This angle is a function of the relative refraction index between the double cone and its exterior. Assuming a value of 1.1 corresponding to the refractive index between a bubble and the bulk liquid hydrogen, we find the very small scattering angle of 10°. Instead of the fixed scattering angle, a refined treatment gives an angular distribution, which is sharply peaked in the forward direction. About 12% of the scattered light is found within a cone of 6° halfangle from the forward direction, i.e. in 0.3% of the total angle 4π. For a more detailed discussion see chapter III and the literature given there.

This means that one has to provide for the possibility of photographing the bubbles at a very small angle from the direction of the direct light. The scattered light intensity varies strongly with this angle as one works on the steep flanks of a sharply peaked distribution function. Therefore, the cameras should receive light of the same scattering angle from every point of the chamber, otherwise a strong variation of contrast is found. A scattering angle of ca. 6° is typical of existing hydrogen bubble chambers.

There seem to be two solutions for these optical requirements:

1. The chamber is illuminated by diffuse light. By an ingenious arrangement of a mask and a lens system, Block *et al.*[4]) succeeded in keeping the direct light away from the cameras. A description of this method is given in chapter III. Its essential point is that light of nearly all scattering angles in the forward direction comes through the irises of the cameras and that bubbles appear equally bright in all parts of the chamber, therefore.

2. The direct light is focussed into the center of the circle, on which the camera lenses lie, see for example [5]). The bubbles are photographed therefore, in a slightly converging light beam. In practical cases the angle at which light is scattered into the cameras can thus be kept constant within ca. 10%. A certain non-uniformity of contrast is caused by this small variation. The high efficiency in the use of light makes the second method very attractive.

In both cases the chamber must have two windows on opposite sides or one window and a reflecting system. The light falls straight through the chamber or is reflected at the rear and leaves the chamber at the point of entry. Actually a window has to occupy the most of one chamber side so that the unilluminated regions are kept small.

Cold seals between a glass window and a metallic flange were unheard of before bubble chambers appeared. These seals have to remain good through several cool-down and warm-up periods. Nowadays, quite a number of satisfying solutions are in use, ranging from inflatable stainless steel tubes with adjustable inside pressure [6]) to simple metallic "O"-rings where the clamping flanges must possess some elasticity to account for different thermal expansions, see also § 7. To secure the tightness of the seal and to have a simple control of the remaining leak rate, double seals are normally applied with a pump-out line in between.

There is another particular connected with the requirements of illumination and photography. As the particle momenta are displayed in the curvature of the tracks by action of a magnetic field, and as this curvature has to be easily detectable on the photographs, the direction of the magnetic field must be perpendicular to the windows. For a designer this means that the chamber walls parallel to the field direction should be most closely surrounded by the magnet coils. The use of pole pieces interferes with the necessity that the windows remain accessible for both illumination and photography. Constructions with one pole piece have been realized, see for example [6]).

From a cryogenic point of view a bubble chamber is a rather unsatisfying instrument if not equipped with its own refrigeration system. The whole heat input would be compensated for by evaporating of the coolant, i.e. liquid hydrogen. The cooling capacity of the returning gas however, would remain unused. The amount of heat the gas can absorb is nearly eight times its heat of vaporization. A reversible cooling system would consume 6190 J to cool 1 g of H_2 at the constant pressure of 1 atm from 300°K down to 20.4°K and another 6220 J to liquefy it. Consequently if the evaporating gas is simply blown off the same refrigeration can be effected at the cost of twice the power which would be consumed in the case where the cooling capacity of the evaporating gas is utilized. In all practical cases this difference in power consumption is considerably greater due to the irreversible character of the various processes, which take place in a refrigerator or liquefier.

Furthermore, it is advantageous to work with a closed refrigeration system if long runs are performed whereby 20–30°K are maintained inside the chamber during several weeks or longer. In a closed system, heat exchangers and expansion devices can easily be kept free of moisture for these long periods.

On the other hand, to build a refrigeration plant which could absorb heat at the temperature of liquid hydrogen takes so much time that the final decision depends on the hydrogen consumption and the liquefying facilities already existing. One should accept a less efficient external system, if a large enough one is already in being, or if one should have to be built for other purposes.

The bubble chamber must be surrounded by radiation shields to decrease the static heat loss. Normally hydrogen chambers with a volume of 10 to 20 l have a static heat loss corresponding to an evaporation of 1 to 3 l of liquid hydrogen per hour.

As for the dynamic heat loss, we have to discuss liquid expansion and gas expansion separately. What happens in the case of liquid expansion is demonstrated in fig. 2. During expansion a change of the chamber volume of about 1% causes the pressure to drop from 5.5 atm to 3 atm. This pressure drop is due to the elastic expansion of the bulk liquid, as no vapor phase exists in the entirely closed chamber volume. The expanded chamber is at the point *B* of the diagram and has to return to point *A*. There are two limiting possibilities: either so fast a recompression is used that the returning line in the diagram almost coincides with the line from *A* to *B*, or recompression begins so slowly that the chamber is fully pressurized by spontaneous boiling, beforehand. Then the returning line goes via *C*. In both cases the curves enclose an area equal to the mechanical work which is delivered to the chamber during one expansion cycle. In the worst case (*A*–*B*–*C*–*A*) this area corresponds to the

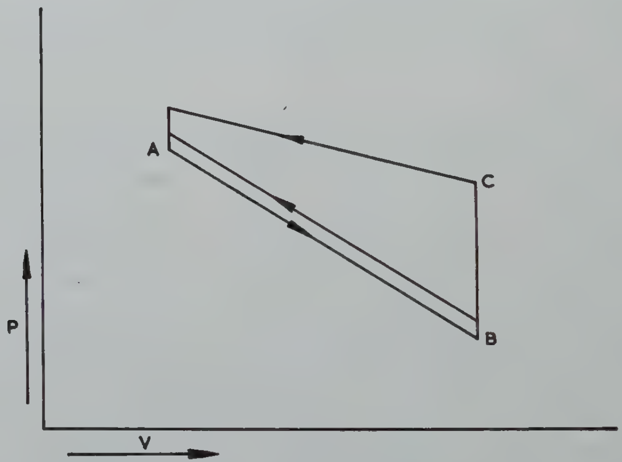

Fig. 2. Schematic *P*–*V*-cycle for liquid expansion, (*A*–*B*–*A*) fast recompression, (*A*–*B*–*C*–*A*) slow recompression.

heat of vaporization of ca. 0.05 l of hydrogen/h per liter of chamber, assuming one expansion every 5 seconds. In all practical cases the time between expansion and compression is made as short as possible, of course, so that the heat loss per expansion cycle is kept at a minimum.

A piston system is installed on top of some chambers; it is in contact with the chamber liquid and provides for the necessary volume change. Others are expanded by means of a bellows. Both bellows and piston are driven from the outside.

In the case of piston expansion the liquid level stands above the piston. Therefore, during an expansion no gas enters the chamber through the small leak along the cylinder wall. One drawback is that the liquid on top of a piston splashes during the expansion stroke causing heat losses which exceed the theoretical value given above. From the data of existing chambers, one can derive the average value of dynamic heat loss corresponding to the heat of vaporization of 0.1 l of hydrogen/h per liter of chamber, assuming one expansion every 5 seconds [7]). The use of a piston limits the freedom of design, as the piston must always be mounted on top of the chamber because of the unavoidable leakage along the cylinder wall.

The bellows system does not show these disadvantages. There is no reason why the theoretical value of dynamic heat loss should not be found in practice, or why the bellows should not be mounted wherever desirable. But here the finite lifetime of a bellows is the problematic point. So far bellows have not been used in large chambers. In smaller chambers mainly stainless steel bellows are applied, both of the welded and of the unwelded type. Volume changes of a few hundred cm^3 are achieved.

Liquid expansion is superior to gas expansion, if one wants to minimize the dynamic heat loss and tries to work with the shortest possible expansion-recompression cycle. On the other hand, all essential parts like the bellows or the cylinder and the piston are mounted in a position where repairing is impossible without warming up the whole chamber and thus interrupting a run for a rather long time.

The great advantage of gas expansion is its simplicity and the possibility to mount all essential parts where they can easily be replaced during a run. In gas expansion, the cold vapor above the liquid is expanded into a buffer volume at room temperature, then

TABLE I

Data of existing or designed bubble chambers

Place	Dimensions	Year of Com-pletion	Useful Volume l	Total Volume l	Window	Ex S
Saclay	35 cm Ø	1960			2 vertical	pis
Saclay	50 cm Ø	1960			2 vertical	pis
Saclay	80 × 30 × 30 cm^3	1961			2 vertical	pis
Liverpool	25 cm Ø	1960	3		2 vertical	bel
Birmingham	9″ Ø ; 4″ deep	1960	3,4	5,5	2 horizontal	bel
Imperial Coll. London	40 cm Ø 15 cm deep	1960			2 vertical	va
British National Project	150 × 50 × 45 cm^3	1962			2 vertical	va
Bologna	18 cm Ø 12 cm deep	1959	2,5	3	2 vertical	bel
Leiden	30 cm Ø 20 cm deep	1961	14	19	1 horizontal	bel
Cern	32 cm Ø 15 cm deep	1960	9,5	13,4	2 vertical	pis
Cern	200 × 60 × 50 cm^3	1963		1000	2 vertical	
Berkeley	10″ Ø	1956	8		2 horizontal	va
Berkeley	15″ Ø	1958	20	40	1 horizontal	va
Berkeley	72″ × 20″ × 15″	1959	300	500	1 horizontal	va
Berkeley	25″ Ø ; 15″ deep	1962			2 horizontal	pis
Columbia	12″ Ø	1957			2 vertical	bel
Brookhaven	14″ Ø ; 8″ deep	1959			2 vertical	pis
Brookhaven	20″ × 9″ × 10″	1959	28	60	2 vertical	pis
Brookhaven	80″ × 25″ × 28″	1961	900	1700	1 vertical	pis
Chicago	23 cm Ø ; 15 cm deep	1960	6		2 vertical	bel
MIT	40″ Ø	1962	500	600	1 vertical	pis
Wisconsin	30″ Ø ; 15″ deep	1962			2 vertical	pis

TABLE I (*continued*)

Data of existing or designed bubble chambers				
Place	Number of Cameras	Film Size mm	Magnetic Field kG	Particular Properties
	3	35	17	
	3	35	17	
	3	35	19	
ool	2	35	8	stainless steel bellows of 8″ free length
gham			22	pulsed magn. field. Coils aircooled. stainless steel bellows 4″ Ø; 5″ long
al Coll. n	3		18	
National t'	3	35	12	illumination system which allows photography at 2° scattering angle
a	3	35	15	welded stainless steel bellows
	3	35	(12)	tomback bellows 210 cm Ø; simple mirror
	3	35	15	
		50	15	closed H_2-refrigeration system utilizing turbines for expansion
ey	2	35	12	diffuse illumination with venetian blind system; one pole piece
ey	4	35	10	retrodirective reflecting system (coat hanger); one pole piece
ey	3	50	18	coat hanger; tilted window
ey	3			the upper window serves as a piston
bia	3	35	13,4	max. repetition rate 2/s; welded stainless steel bellows
aven	3	35	17,5	
aven	4	35	17	magnet coils inside vacuum tank; chamber body made of an Al-forging
aven	4	35	17	simple mirror; one pole piece
o	3	35	20	chamber for stopping particles
	4	35	20	closed He-refrigeration system
sin		70	30	3–4 megawatts magnet power

recompressed, cooled down to liquid nitrogen temperature and finally used to pressurize the liquid volume again. During the pressure drop the liquid rises somewhat in the expansion line, starts to evaporate until a cold surface layer is formed, and is pressed back by the recompression. Here the dynamic heat loss is determined by the amount of gas which evaporates from the liquid at 25°K during the expansion and has to be reliquefied when it comes back during recompression at a temperature of about 80°K. The problem is how to avoid drastic splashing in the expansion line. Because of expansion speed, and in order to keep the level differences of the liquid small, this line leads through a very wide pipe which makes it nearly impossible to avoid sensible heat losses by splashing. The average loss derived from existing chamber data is 0.5 l of hydrogen/h per liter of chamber, assuming one expansion every 5 seconds [7]).

At the end of this section we present a table of hydrogen chambers already working or under construction in Europe and the U.S.A. Small chambers with diameters less than 10 cm are omitted.

The *useful volume* is the illuminated volume, where tracks can be photographed. The *total volume* gives the liters of liquid hydrogen in the chamber not counting reservoirs. Under *windows* their number and position is given. The information under *expansion system, magnetic field, number of cameras* and *film size* needs no further comment.

The construction of the Leiden bubble chamber was started early in 1957. At that time the technique of hydrogen chambers showed two lines of development. 1) The Berkeley group under Prof. L. Alvarez favoured gas expansion and horizontal windows. Several chambers of increasing size had been built or designed. 2) The group under Prof. J. Steinberger at Columbia University preferred liquid expansion with a bellows system and vertical windows. Later on Shutt and Adair of Brookhaven perfected this chamber type introducing a piston system instead of the bellows.

Most ideas for more recent chamber designs are derived from these two "schools". Except for the expansion system our chamber resembles the Berkeley 15″-chamber. Both of them were designed independently at about the same time. For expansion a bellows is placed at the bottom of our chamber.

§ 4. *Accuracy of track location.* In the following the total resolution in space which can be achieved with a hydrogen bubble chamber will be discussed. Further, how far secondary effects like convective movements of the chamber liquid influence the accuracy of track location will be investigated.

Each bubble needs some time to grow from its critical dimension to a visible size. As mentioned in § 2 the critical radius is about 10^{-7} cm. The term visible size cannot be well defined, as it depends on the light intensity with which the chamber is illuminated. The time of bubble-growth is kept so small that the actual size of a bubble at the moment of photography does not influence the space resolution, i.e. the dimensions of the image of a bubble on the film are entirely determined by the emulsion properties and diffraction effects. A further decrease of the bubble-growth time would merely produce worse contrast, because less light per bubble is scattered.

In normal bubble chamber work, the resolving power attained with a depth of focus of about 25 cm is 50 bubbles/cm. In hydrogen the bubbles are allowed to grow for 1 ms or less. The real bubble diameter is kept well below 200 μ.

Assuming that the track center can be located within 1/10 of the width, one finds a minimum uncertainty of position equal to $2 \cdot 10^{-3}$ cm. Some slight improvement may be brought about by the use of an annular diaphragm, as the British Bubble Chamber Team proposes [8]). The depth of focus increases if the center region of an iris is covered by a disc and its diameter correspondingly enlarged so that the same amount of light is transmitted. Therefore it should be possible to work with a smaller effective stop using an annular diaphragm and yet achieve the same depth of focus. Diffraction effects should become small enough so that the resolution would be limited mainly by the properties of the emulsion.

During the time the bubbles grow to visible size, tracks may be distorted due to the convective movements in the chamber liquid and to the liquid flow started by the expansions. As long as the distortions are systematic it is possible to correct for them. Here we only are interested in irregular distortions which may reduce the accuracy of locating the actual track.

There will be no convection in the chamber if the thermal insulation is ideal. However, with a heat input due to radiation, expansion etc. convection is essential for maintaining a uniform temperature in the liquid, because liquid hydrogen is such a poor conductor. The influence on the track quality remains small if the time for bubble-growth is small.

After an expansion the forced movement of the liquid does not cease immediately, as the decay time of a vortex is of the order of 10 minutes [9]). To avoid difficulties due to this, the chamber has to be expanded as homogeneously as possible, and again the time of bubble-growth must be small.

Few new restrictions on the track quality will arise, if this time is about 1 ms and the chamber has been carefully designed with respect to these effects. Measurements by the CERN-group show that under optimal conditions the unsystematic deviations from the systematically smoothed tracks are smaller than $3 \cdot 10^{-3}$ cm [10]). The setting error of the measuring device IEP in this investigation was $(2.4–2.7) \cdot 10^{-3}$ cm. Therefore this result means that the locating of particle tracks is not seriously, if at all, affected by distortions.

The above considerations show that it should be possible to construct a hydrogen bubble chamber which allows a track definition within $2 \cdot 10^{-3}$ cm.

§ 5. *Possibilities of a hydrogen bubble chamber.* In this section we will examine what information can be extracted from bubble chamber photographs. The first part deals with directly observable charged particles, the determination of their momenta, their ranges etc. In the second part the identification of uncharged particles will be touched upon.

Charged particles mark their way through the liquid by a chain of bubbles. Momenta can be determined by bending the tracks in a magnetic field and measuring their curvature. The relation between momentum and curvature is $p \cos \delta = nKrB$, where $K = 0.3$ cm^{-1} kG^{-1} MeV/c, r = radius of curvature in cm measured on the parallel orthogonal projection of a track into a plane perpendicular to B, n = charge of the passing particle in units of the electron charge, B = magnetic field in kG, p = momentum in MeV/c and δ = angle between the track and a plane perpendicular to B. If multiple scattering is neglected a maximum momentum of 15 GeV/c can be detected on a track of a length $L = 10$ cm in a field of 12 kG, corresponding to a radius of curvature $r_l = 40$ m. For higher momenta the curvature disappears in the minimum track width which has been discussed in the preceeding section. The maximum detectable momentum is proportional to L^2.

Multiple scattering, however, impairs this result at least for particles with small energies. For protons and pions the apparent radius of curvature r_{sc} due to multiple scattering in liquid hydrogen is given as a function of energy in table II. A track length of 10 cm is assumed. As $r_{sc} \sim L^{\frac{1}{2}}$ one easily finds r_{sc} for other values of L.

TABLE II

Track properties of protons and pions

Ranges are given for liquid hydrogen. r_m is the radius of curvature as consequence of a magnetic field. Multiple scattering causes a curvature of tracks with the average radius $\pm r_{sc}$

kinetic energy MeV	range proton cm	$B \cdot r_m$ proton kG·m	r_{sc} proton m	range pion cm	$B \cdot r_m$ pion kG·m	r_{sc} pion m
10	1	4.60	1.66	4	1.80	1.79
50	17	10.50	7.82	75	4.30	7.25
100	65	14.80	14.80	200	6.50	13.10
500	850	36.30	60.20	1700	20.80	36.70
1000	3000	56.50	104.00	3500	37.70	81.30
5000		195.00	381.00		172.20	340.00

The radius r_{sc} must be compared with the magnetic radius r_m which follows from the values Br_m in table II. Because r_{sc} indicates a curvature in an arbitrary direction due to a large number of uncorrelated small angle scattering processes, the magnetic radius r_m can only be measured if it is smaller than r_{sc}. The relative error in the momentum measurements can be estimated as follows: $\Delta p/p = r_m/r_0$, with $r_0^{-2} = r_l^{-2} + r_{sc}^{-2}$.

To identify a particle it is necessary to know a second independent parameter besides the particle momentum. Ranges are normally too large to be measured as an inspection of table II shows. There is the possibility of counting the number of bubbles per unit track length or, rather, measuring the mean gap length between them. These quantities are related to the number of δ-rays per unit track length. Before advantage can be taken of these measurements, empirical relations with energy and restmass have to be established [11]). For relativistic particles no variation of the mean gap length with momentum has been found in liquid hydrogen. Therefore this sort of measurement yields information only in the low energy range.

Uncharged particles do not leave a track in a bubble chamber. Nevertheless track chambers are indispensable when unstable uncharged particles are studied, as for example the K^0, Λ^0 and Σ^0. Production and decay processes of these particles involve at least two outgoing reaction products, whose kinematics must be known simultaneously. For example, the following reaction is possible: $\pi^- + p \rightarrow \Lambda^0 + K^0$. Both secondaries are invisible and have to be identified by their decay products. Let us assume the following decay modes $\Lambda^0 \rightarrow p + \pi^-$ and $K^0 \rightarrow \pi^- + \pi^+$. The analysis of such an event starts from the end. The momenta of the invisible particles are determined from the momenta of their charged decay products. Then the mass of the uncharged particles is determined by checking energy conservation. For this the energy of the incoming particle must be known. One hopes that all but one possibility can be rejected, so that finally a clear picture of the event arises.

Complicated reactions like this one cannot be studied in counter experiments. The only way to study a reasonable number of events of this kind is by the use of a track chamber in a high energy beam from an accelerator.

Table III contains all known particles with exception of the antiproton, antineutron and antilambda. It is meant to give a clue about the needed dimensions of a track chamber, if decay processes of one of the unstable particles should be observed. The *decay length* L_0 for $\beta^2 = (v/c)^2 = \frac{1}{2}$ is given.

In table III the particles are divided into four groups: 1. stable particles; 2. long lived unstable ones whose decay can only be observed in bubble chambers when they are captured or come to rest there; 3. the particles with a medium life time, which decay after a reasonable track length unless their total energy exceeds their rest energy by many orders of magnitude; 4. the short lived particles which decay at their "point of origin" within the accuracy of a bubble chamber, at all feasible energies at least.

We conclude this section with two remarks mainly concerning our 30 cm bubble chamber:

A secondary, produced in the center region of our chamber, has a track length of about 10 cm before it leaves the chamber. A mean free path of 10 cm corresponds to a cross-section of $3 \cdot 10^{-24}$ cm^2 in liquid hydrogen. A cross-section of this large size never occurs in high energetic collisions with protons, and therefore an interaction of a secondary cannot be observed.

TABLE III

Characteristic figures for the decay of elementary particles
L_0 must be multiplied by the dimensionless quantity pc/m_0c^2 to obtain the actual decay-length L for a particle of rest mass m_0 and momentum p

type of particle	decay products of a possible mode	reduced decay-length L_0 cm	kinetic energy when $L = 10$ cm MeV	approx. rest energy MeV
stable particles				
γ	—	∞	—	0
$\nu, \bar{\nu}$	—	∞	—	0
e^+, e^-	—	∞	—	0.51
p	—	∞	—	938
particles with long lifetime				
μ^+, μ^-	$e + 2\nu$	6.6×10^4	0	106
π^+, π^-	$\mu + \nu$	7.7×10^2	0	140
θ_2^0	3π	1.8×10^3	0	498
K^+, K^-	3π, 2π, etc.	3.7×10^2	0	494
n	$p + e + \nu$	3.0×10^{13}	0	939
particles with medium lifetime				
θ_1^0	2π	3.0	1210	498
Λ^0	$N + \pi$	7.5	740	1115
Σ^+	$N + \pi$	2.4	4150	1189
Σ^-	$N + \pi$	4.8	1550	1196
Ξ^-	$\Lambda^0 + \pi$	4.0	2250	1318
particles with short lifetime				
π^0	2γ	5.7×10^{-6}	2.4×10^8	135
Σ^0	$\Lambda^0 + \gamma$	< 0.3	$> 4 \times 10^3$	1191

Assuming a cross-section of 10^{-28} cm^2 there will be one event on 3 km track. In our chamber we will work with ca. 10 incident particles, having a usable track of 2 m/photo. Therefore a cross-section of 10^{-28} cm^2 will mean one event per $1.5 \cdot 10^3$ photos. The chamber has to work 2h to take these $1.5 \cdot 10^3$ photos. Six man-days are necessary merely to scan them. If 100 events are wanted it takes considerably more than two man-years for their complete evaluation. Consequently a cross-section of 10^{-28} cm^2 can be regarded as the minimum for our bubble chamber without preselection of events.

Chapter II

CHAMBER CONSTRUCTION AND PERFORMANCE.

§ 6. *General design.* The general design of the Leiden bubble chamber is founded on the following arguments.

1. We wanted to build a helpful tool for high energy physics, intending to do experiments at the 1 GeV proton accelerator in Delft. We decided to construct a chamber with a diameter of 30 cm and a depth of 20 cm. When we started the construction in 1957, a 30 cm chamber was quite a big one. Its usable volume of 14 l was – and still is – thought to be sufficient for most of the experiments that can be done at a 1 GeV accelerator.

2. As we wished to reduce the danger of window failure we have been led to a construction with one window. This implies the use of a mirror system. The flash lamp then doubly illuminates the chamber: once directly and once after the light is reflected by the mirror. A bubble scatters the light in forward direction, and is therefore seen by a camera once directly and once in the mirror. Consequently two images of each track appear on the film. The second image is seen behind the mirror. On the film it appears unsharp as it is normally out of focus for the cameras. In our experience it has been possible to set the focus of the cameras so that the second track image disappeared in the background, unless the corresponding tracks were formed in the vicinity of the mirror.

3. The most controversial question was whether to put the window horizontal or vertical. Both propositions have a number of advantages and disadvantages. Again our main argument was to achieve a maximum of safety. A horizontal window was chosen as it allows a construction where the chamber hangs in a sort of cryostat. This cryostat or vacuum tank can be used as a hydrogen reservoir or can be kept at a rough vacuum; in both cases it works like a cold buffer volume into which the pressurized hydrogen can expand in case of window failure. If the vacuum tank is built to withstand the pressure shock, such a system is rather safe.

We keep the vacuum tank, which of course is high vacuum insulated from outside, at a pressure of 10^{-1}–10^{-2} mm Hg. This gives another advantage: the cold seal between the window and the metallic chamber body need not be high vacuum tight, as the thermal insulation does not depend on it. What leaks out of the chamber into the cryostat space must be replaced by condensation, this being the limiting factor for the tolerable leakage rate in our case.

Furthermore the horizontal window construction makes it easier to get a beam through the chamber, whatever its energy. Trouble namely can be caused by the magnetic stray field outside the chamber which bends the beam out of its original direction. As long as this happens in a horizontal plane by action of a vertical field, it only influences the position of the chamber. But if the beam is bent out of the horizontal plane by action of a horizontal field a compensating magnet has to be used. Otherwise the mean beam direction inside the chamber will be inclined with respect to the horizontal plane, demanding the chamber to be tilted. Such an unpleasant horizontal stray field happens to be connected with the use of vertical windows.

One must be very careful to avoid a temperature gradient in the hydrogen volume, if one has a chamber with a horizontal window on top. Most of the heat leakages come from above. The chamber is open to thermal radiation from the warm top flanges there (see fig. 3), and the suspension and pipe connections conduct heat to the upper part of the chamber. Futhermore all bubbles rise a little bit during the expansion time, giving back the heat of vaporization to the chamber liquid at a place somewhat higher than where originally taken from. Therefore it is possible that the temperature increases in an upward direction. A temperature gradient occurs easily, especially just below the horizontal window where no convection can take place. If the top layer is only slightly warmer there will arise no difficulty unless spontaneous boiling disturbs the view of the cameras. However, it is still true that there will be a higher sensitivity for bubble formation. Also, the speed of bubble growth will be larger there, but it only means that tracks in this top layer must not be used for bubble counting. In chambers with vertical windows a tendency to build a warm top layer exists, too, but here this top layer belongs to the unilluminated and unused volume. Normally the expansion system is mounted on top of this type of chamber. Its moving parts cause an irregular flow there, which helps to prevent a temperature gradient.

In our experience, perhaps, the most serious argument against a horizontal window is that dirt tends to settle on the optical components. Inside the chamber frozen out impurities fall on the mirror and disturb the dark background, and outside abrasion products of the mechanical connections to the expansion system partly terminate on the window.

4. Liquid expansion was chosen because of the possible high repetition rate. Furthermore it should give fewer unsystematic track distortions. The simplest way to fit liquid expansion to our general design idea was to make the bottom of the chamber movable by means of a bellows. The chamber can expand by its own pressure and can be recompressed moving back the chamber bottom with help of a mechanical system.

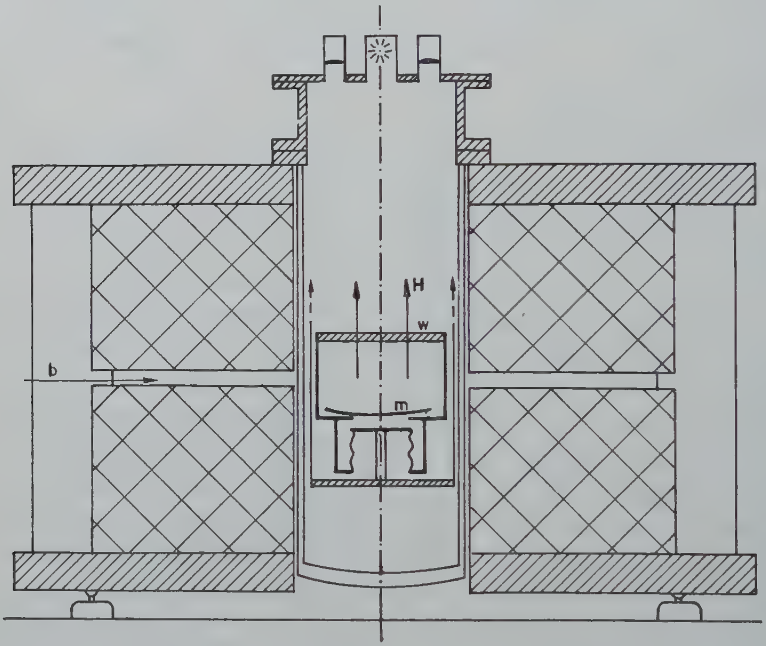

Fig. 3. The chamber construction. *b* means beam direction, *m* mirror, *w* window and *H* magnetic field. The true height of the magnet is ca. 1 m.

5. The magnetic field which serves for the detection of particle momenta is created by two coils around the vacuum tank. The chamber is accessible to the beam through a small space between the coils. Using an iron yoke to concentrate the back flux, the forces between the coils are compensated for a great deal and the central field is increased. Operators are protected by the magnetic structure. We plan to work with a total field of 12 kG. The power consumption

of the magnet is anticipated to be 450 kW at this field strength.

These five arguments give account of the general how's and why's in our construction. In fig. 3 the actual design is summarized.

Here we should like to comment on one point, in which our chamber probably differs from all the others, which are existing. The Leiden chamber had to be built inside the normal laboratory routine and it should possess such a simplicity that it could be run by one physicist with some technical help. At the end of the construction we can state that the chamber has been built in four years at the cost of 45,000.— Dutch Guilders excluding the cost of the magnet and salaries, using four years of a full time physicist, three years of part time students, four years of a young technician. Large profit was taken, of course, from the stock of experience in all sorts of techniques which is on hand in the Kamerlingh Onnes Laboratory.

§ 7. *Mechanical construction.* The body of our chamber is made of stainless steel type 304. Some parts are machined from forged flanges and are not as unmagnetic as the rest. All joints are argon arc welded.

The major parts of the construction were built in the workshop of the "Veluwsche Machinefabriek" in Epe (Netherlands), in close collaboration with Mr. E. S. Prins of our institute.

The chamber consists of five stainless steel cylinders and flanges as shown in fig. 4. They are clamped together with "O"-ring seals in between them. We have chosen this design to ensure a cheap construction and an easy operation when the mirror, the bellows or the window must be replaced. The cylinder enclosing the illuminated volume can be exchanged. We shall have built some spare cylinders with different beam windows to meet various experimental requirements.

The glass is mounted excentrically on the upper flange. In this way one has enough space on one side of the top flange to connect all necessary tubes like the filling line, the evaporation line etc. to the chamber.

The "O"-rings are made of drawn copper wire with a rectangular cross-section. The annular sealing surfaces have a width of 2 mm and are covered with a thin indium film. The variation in height, especially where the two ends of the copper profile are silver soldered to form a ring, amounts to 0.10 mm. We could leave these

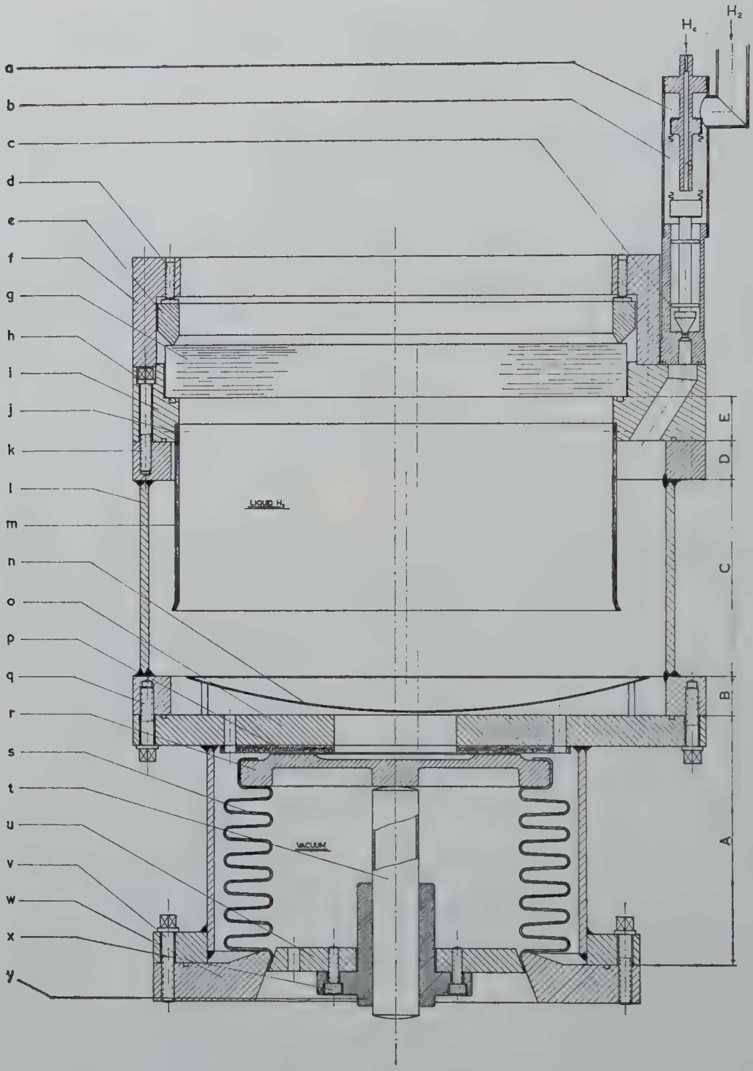

Fig. 4. The chamber body. (Scale 1 : 5).
One H_2-line is visible, which enters the chamber from above via a bellows valve and ends in the chamber behind the copper cylinder.

A = 162 mm
B = 25 mm
C = 130 mm
D = 25 mm
E = 27 mm

a	one of the two bellows valves, which are operated by helium gas; under working conditions these valves allow one to disconnect the filling line and the evaporation line from the chamber.
b	two-ply stainless steel bellows, 20 convolutions and 42 mm length.
c	metallic sealing: brass cone against stainless steel; the approximate leakage is 10 cm^3/s under working conditions at 1 atm pressure head across the valve.
d	36 Allen screws M6 which provide the needed sealing force for the glass to metal seal *h* between *g* and *i*.
e	a massive copper ring distributes the sealing force homogeneously over *h*.
f	"L"-shaped flange works like an elastic strip under a bending moment. It is fixed on *i* by 24 screws M8 located between the 24 screws indicated by *k*.
g	window of tempered BK 7 glass, 300 mm in diameter and 35 mm thick.
h	"O"-ring of annealed copper which is covered by a thin indium film.
i	excentric flange where all connections to the chamber enter; the smallest inner diameter is 280 mm.
j	indicates the position of 4 M3 screws, which fix *m* on *i*.
k	24 M8 screws, which provide the needed sealing force for the metal to metal seal between *i* and *l*; the seal consists of an "O"-ring similar to *h*.
l	cylinder with flanges which encloses the illuminated chamber volume; 320 mm and 336 mm are the smallest and the largest inner diameters, 370 the largest outer diameter, 5 mm the wall thickness.
m	copper cylinder inside the chamber which serves to minimize temperature differences and track distortions; its wall thickness is 1 mm.
n	chromium plated brass mirror of 300 mm diameter with a radius of curvature of 1209 mm.
o	flange at the bottom of the illuminated volume; several holes provide the connection to the expansion bellows *s*.
p	leather ring, which serves as shock absorber; the air driven piston on the other side of the expansion system outside the vaccuum tank is stopped by a rubber shock absorber, before *r* hits *p*.
q	24 M8 screws, which provide the needed sealing force for the sealing between *o* and *l*; the seal consists of an "O"-ring similar to *h*.
r	movable chamber bottom, drawn in a position when the chamber is pressurized; it is made of brass and soft soldered to the bellows *s*.
s	tomback bellows (80% Cu, 20% Zn), 2 mm wall thickness, 6 convolutions and 295 cm^2 average surface.
t	stainless steel plunger, which transmits the force, needed for the recompression, to the movable chamber bottom *r*; its wall thickness is 1.5 mm.
u	stainless steel flange, which is soft soldered to *s* and *w*; simultaneously it is kept in position by stainless steel strips fixed on *w*. These strips are not drawn; the small hole on the left is the only connection between the space inside the bellows *s* and the vacuum tank.
v	24 M8 screws, which provide the needed sealing force for the "O"-ring seal between *o* and *w*; the "O"-ring is similar to *h*.
w	stainless steel flange, which closes the chamber from below; its outer diameter is 315 mm.
x	6 M6 screws, which fix *y* on *u*.
y	brass cylinder guides the plunger *t*.

sealings untouched for several runs without finding untolerable leaks developing.

The glass window is sealed to the chamber body in a very similar way. As can be seen in fig. 4 the glass is held down to its sealing by a massive ring of copper. The contact surface between this ring and the glass has an annular shape of about 2 mm width. Its position is just opposite of the sealing surface on the other side of the glass. The copper ring serves to equilibrize the sealing force over the whole contact surface and to partially compensate for the difference in thermal contraction between glass and stainless steel. The sealing force is created and transmitted to the copper ring by means of 36 Allen screws M6, placed at a distance from each other of about 25 mm.

The "L"-shaped stainless steel flange, which surrounds the copper ring, acts as an elastic strip under a bending moment. It helps to avoid a fatal increase of the sealing force due to the different thermal contraction of the glass-, stainless steel- and copper parts, when the chamber is cooled down.

During our first runs we worked with windows of untempered optical glass. Although we changed over to tempered glass it is perhaps worthwhile to describe this early experience.

Peak values of stress occur where the metallic "O"-ring touches the glass. These may not surpass the breaking stress of glass which is 450 kg/cm^2 (untempered) and 2,000 kg/cm^2 (tempered) at room temperature [12]). The breaking stress times the sealing surface gives the maximum force f with which the glass may be clamped to the chamber body. Our window has a diameter of 30 cm and the diameter of the sealing surface is 29 cm. Therefore we find the limit values for f: $f = 41\, d$ t (untempered) and $f = 182\, d$ t (tempered). d is the width of the annular sealing surface in cm.

It is necessary that f exceeds the force with which the pressurized hydrogen in the chamber acts in the opposite direction on the window, i.e. ca. 4t. Under working conditions we have 6 atm abs. inside the chamber and vacuum outside. Consequently d must be larger than 0.1 cm in case untempered glass is used.

We had chosen, therefore, a copper "O"-ring with a square cross-section, $d = 0.2$ cm. The manufacturing tolerances of this glass to metal seal had to be very stringent. A variation in height of 0.1 mm was fatal for untempered glass.

With a carefully built "O"-ring of square cross-section we cooled down the chamber to liquid hydrogen temperature and everything worked fine. The untempered glass seemed to stand the test. But when we inspected the window thoroughly a week later we discovered a lot of barely visible radial cracks at every place where the "O"-ring had touched the glass.

With tempered glass a square cross-section of the "O"-ring is unnecessary as our above estimate suggests and experience shows. d must be larger than 0.02 cm. The manufacturing tolerances of an "O"-ring with a circular cross-section are less stringent. In its position under pressure it is deformed into an oval shape, so that small differences of height are smoothed out. This deformation is possible because the yield strength of annealed copper (800 kg/cm^2) is smaller than the breaking strength of tempered glass (2,000 kg/cm^2) at room temperature. The "O"-ring surface is covered with a thin indium film to improve the sealing.

The total leakage between the chamber and the outside cryostat normally does not exceed 0.5 l NTP per hour at a pressure difference of 1 atm. Four "O"-ring seals with a diameter of about 30 cm each and several small ones contribute to this rate. During the cool-down period thermal stresses deform the sealing flanges so that 100 l NTP/h may escape for a time.

Inside the chamber a 1 mm thick copper cylinder is mounted, which surrounds the illuminated volume. It prevents a temperature gradient in the liquid volume and helps to get a uniform flow pattern during the expansion. Between this copper cylinder and the chamber walls a cooling spiral and some thermometers are located. Also the filling line and the evaporation line end there.

The whole chamber is suspended by three stainless steel tubes from the top flange of the vacuum tank. All pipes (filling-, evaporation- and condensing-line, inlet and outlet of the cooling spirals, gas- and vapor pressure- thermometer) and four thermocouples are connected to the chamber from above as in normal cryostat technique.

The vacuum tank is built from two thin-walled stainless steel cylinders with curved bottoms leaving space for a high vacuum insulation in between. It has heavy iron flanges on top, from which the chamber is suspended and which support the optical components.

The magnet is planned to surround the vacuum tank which will hang in the top flange of the iron yoke, as shown in fig. 3.

§ 8. *Cooling system.* The cooling system of our chamber is shown in fig. 5. 3 m of a spiraled $\frac{1}{4}''$ copper tube run through the liquid in the upper part of the chamber, figuring as an evaporator. Parallel to it and for the same purpose 1 m of $\frac{3}{4}''$ copper tube is mounted in direct contact with the upper flange. This line has its own return tube so that the flow through it can be regulated separately.

In these tubes liquid hydrogen is evaporated at a temperature of 20°K. It is fed into the evaporators directly from a hydrogen storage vessel, in which the pressure is kept at 1.2 atm abs. The returning gas is blown into atmosphere or sent back into a gasometer. It passes through a valve at room temperature by which the amount of evaporating refrigerant is regulated by hand.

The evaporator which is in direct contact with the upper flange is only used after the whole chamber has nearly reached a temperature of about 30°K. Otherwise one would produce thermal stresses which could be fatal for the window. During the cool-down period we observed maximum temperature differences of about 10°K over the upper flange.

Normally the chamber is filled with liquid hydrogen from a storage vessel. The liquid is filtered through a piece of milk filter. It is necessary to condense the last liters into the chamber, because the evaporation line leaves the chamber a little bit below the glass window. We mounted a condensing line, which is in thermal contact with the cooling system. Like in a counterflow heat exchanger the hydrogen gas is cooled by the gas stream coming from the evaporator and is condensed at 5 atm. Thus we have the alternative possibility to fill the chamber entirely by condensing.

In principle our chamber represents a closed and entirely filled liquid volume at working conditions. Temperature and pressure can be regulated by the amount of coolant which is allowed to evaporate. Two bellows valves which are operated by helium gas and placed on the upper flange serve as safety outlets when the pressure rises too much, see fig. 4.

In practice we found it convenient to regulate the chamber pressure independently from the temperature. The leakage through the bellows valve, which disconnects the condensing line from the chamber, amounts to some cm^3/s at a pressure difference of 1 atm. We pressurize the chamber liquid above its vapor pressure by applying a controlled pressure to the condensing line with the cold bellows valve closed. The leakage transmits this overpressure to the chamber but does not influence the pressure drop during the 20 ms of expansion.

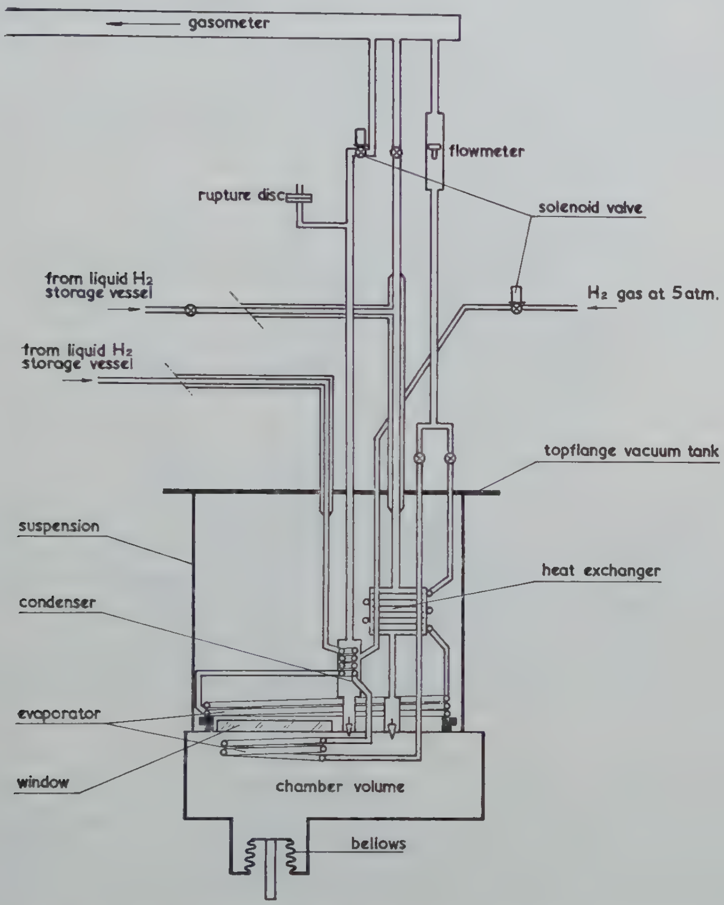

Fig. 5. The flow diagram. The right part of the chamber is far out of scale. The chamber is nearly symmetrical to an axis through the middle of the window as can be seen from fig. 4. The vacuum tank around the chamber is omitted.

At the beginning of a hydrogen run the temperature of the chamber has to be lowered as far as possible before liquid hydrogen is introduced into the cooling system. For this purpose we circulate liquid nitrogen through the evaporator inside the chamber until a mean temperature of about 120°K is reached.

A nitrogen cooled shield surrounds the whole chamber with the exception of the window side. It serves to lower the radiative heat input. The shield is placed in the high vacuum space of the vacuum tank and is fed by a N_2-storage vessel. No nitrogen reservoirs are mounted inside the chamber structure to simplify the construction and to keep the dimensions of the magnet at minimum.

In the following we give some figures which are a digest of the experience with our cooling system.

cooling down 300°K–120°K	
time	9 h
consumption liquid nitrogen	150 *l*
cooling down 120°K–25°K	
and filling time	7 h
consumption liquid hydrogen	150 *l*
working conditions	
consumption liquid nitrogen	4 *l*/h
consumption liquid hydrogen	10 *l*/h

We do not claim to have the most efficient cooling system but the most simple one we could think of. It can be regarded as a special advantage, that the total amount of liquid hydrogen present inside the chamber structure is kept at an absolute minimum. We avoided the use of all sorts of reservoirs. When the hydrogen storage vessel must be changed, the working conditions are disturbed for some minutes only.

§ 9. *Expansion system.* In our chamber the liquid hydrogen is expanded by means of a bellows which provides the possibility to enlarge the entirely closed chamber volume, as can be seen in fig. 4. The bellows was purchased from IWK Karlsruhe with the following specifications:

average cross-section	295 cm^2
material	tomback (80% Cu, 20% Zn)
number of convolutions	6
wall thickness	2 mm
maximum external working pressure	5 atm
maximum stroke	+11,4 mm; −5,7 mm
spring constant	220 kg/cm

From these numbers follows that the maximum change of volume is equal to 500 cm³. This means $\Delta V/V = 2.7\%$, as our total hydrogen volume amounts to 19 l. Experience showed that even a volume change of less than 1% at 27°K is sufficient to obtain tracks.

At 27°K hydrogen has a vapor pressure of ca. 5 atm. We kept the pressure in the chamber slightly above the vapor pressure so that no vapor phase could exist there. Consequently the above given maximum external working pressure is exceeded under working conditions. We took this risk considering that the yield strength of tomback increases when the temperature is lowered.

At room temperature our bellows has performed more than 10^4 expansions with a stroke of 6 mm and a pressure of about 4.5 atm. At ca. 30°K we had the bellows work with a stroke of 6–8 mm and a pressure of 6 atm for more than $1.5 \cdot 10^4$ expansions. No sign of an inelastic deformation has been found.

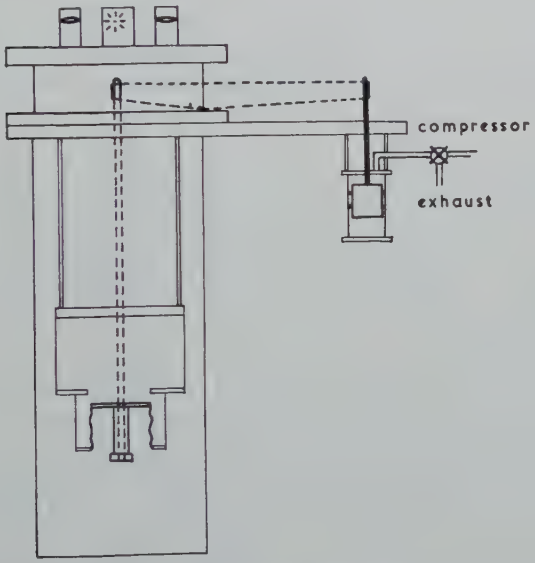

Fig. 6. The expansion system. The two rods and the double lever, which connect the bellows to the piston, are given by broken lines, because they are not cut by the section-plane.

It is advantageous to use a bellows with a large diameter if the chamber expands by its own pressure. The force F with which the hydrogen acts on the movable chamber bottom becomes high and the needed stroke S small. The expansion time τ is diminished by both effects. The mass M of the mechanical system, however, increases with the cross-section of the bellows and consequently the expansion time τ lengthens again. Considering the three effects together the expansion time shortens if the bellows cross-section is enlarged. It is $\tau^2 = cMSF_{av}^{-1}$ which is roughly proportional to the inverse of the bellows cross-section. The dimensionless quantity c has a value $1.57 < c < 2$. F_{av} means the average force the liquid exerts on the expansion system during the time τ. With $M = 20$ kg, $S = 1$ cm and $F_{\mathrm{av}} = 300$ cm^2. 2.5 atm we get $\tau = 7$ ms.

The connections between the chamber and the bellows are made by crimping, clamping and soft soldering in such a way that the soft soldering does not have to stand any stresses. As can be seen from fig. 4 no pressure shock can reach the vacuum tank in case of failure of the bellows. The connection between the space inside the bellows and the vacuum tank goes through the small hole in the soldered flange at the bottom of the bellows (see fig. 4 *u*).

The chamber bottom which is made movable by virtue of the bellows is kept in position by a mechanical system. The construction is sketched in fig. 6. An air driven piston outside the vacuum tank counterbalances the force on the chamber bottom exerted by the hydrogen. The rods connecting the piston and the bellows with the lever, transfer the work under tension. The total effective mass of all moving parts of this system is ca. 22 kg if the whole system is thought to be located at the side of the short leverarm. The ratio of the leverarms is 1 : 2.

Pressurized air is admitted to the piston by two Barksdale-3 way-$\frac{3}{4}''$-valves (24 VDC, type 103963 and 103964). It took us a long time to find an arrangement for these valves, which ensures a reliable working of the pneumatic system. This arrangement is given in fig. 7. The magnetic coils of both valves are energized until the expansion starts. The whole expansion cycle consists of four steps. The first two, 0–1 and 1–2, are responsible for expansion and recompression. The current in one of the valves is switched off each time. The last two steps serve to re-establish the begin condition: the current is switched on again without consequences for the pneumatic system. Without the constriction in the narrow line from the compressor to the second valve the pilot of the first valve does not work properly at the fourth step 3–0. As switching element the germanium power transistor 2N268 is used, which is protected against voltage peaks V_{ec} higher than 33 V by the Zener power diode ZL33.

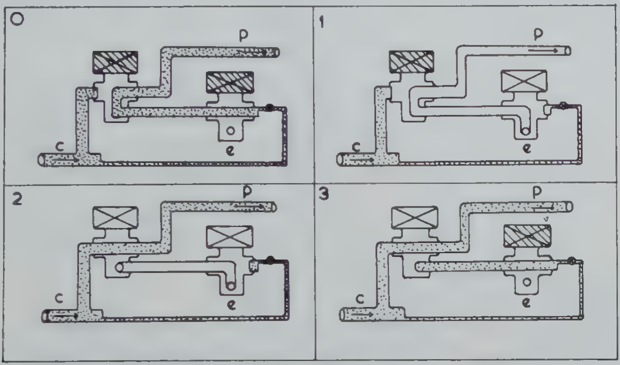

Fig. 7. The expansion valves during the working cycle. The hatched coils are energized, the dotted tubes are pressurized. *c* means the line from the compressor, *p* the line to the piston and *e* the exhaust.

The trigger system works as follows: the master pulse is fed into a monostable multivibrator. The time, the quasistable state lasts, is variable between 5 and 100 ms. The block pulse coming from this multivibrator passes a diode so that only the end of the pulse is transmitted. In this way a simple trigger delay is achieved. Next the signal goes to another monostable multivibrator. Here the duration of the quasistable state can be adjusted between 50 and 800 ms. The output is a negative block pulse, which undergoes a current amplification and sign inversion before it is sent onto the base of the 2N268 switching transistor. For details see fig. 8. Each Barksdale valve is triggered independently, so that the just described circuit is needed twice.

The time the bellows needs to perform an expansion of the chamber volume with a stroke of 6 mm is measured equal to 8 ms, if the chamber is at 6 atm. The total time of expansion and recompression can easily be varied by adjusting the independent delays of the Barksdale valves .We found a minimum duration of 20 ms, when the stroke is 6 mm, the chamber pressure 6 atm and the piston pressure 9 atm. The limitation of expansion speed is given by the opening of the Barksdale valves. To minimize the

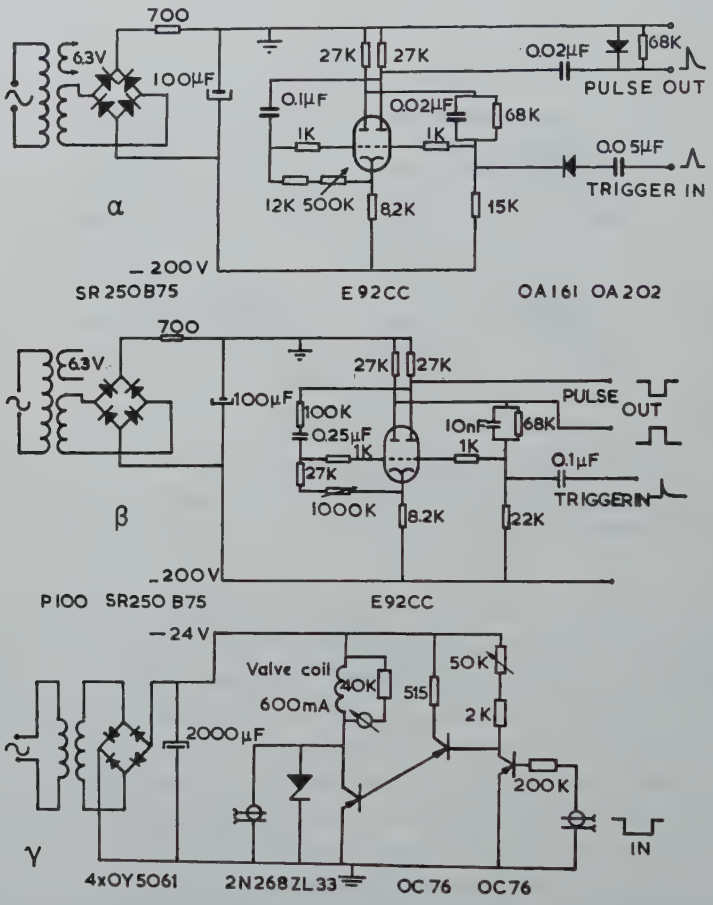

Fig. 8. Circuit of the expansion system. Each pulse-out serves as trigger for the subsequent unit. α effects an adjustable pulse delay and β forms the needed pulse shape for the switching unit γ.

time of expansion the exhaust line is connected to the space below the piston. Thus the piston receives the impact of the expanding air, which considerably reduces the time of expansion.

Chapter III

THE PHOTOGRAPHIC AND ILLUMINATION SYSTEMS.

§ 10. *Components of our optical system.* The whole construction of our bubble chamber is based on the use of an optical system, where the photographs are taken from the same side as the flash light illuminates the chamber. We put a spherical mirror at the bottom of our chamber so that the cameras receive light which is scattered by bubbles in forward direction. The light source is in the optical center of the mirror. Thus a converging light beam leaves the chamber in direction of the cameras, which are placed outside this light cone and receive only the scattered light (see fig. 3). The radius of curvature of the mirror is 1209 mm and the distance between the light source and the mirror is 1135 mm. The slight difference is due to the influence of the glass window and refraction by the liquid hydrogen, which cause a displacement of the optical center of the mirror.

The mirror itself is made from a brass plate, machined to spherical size, polished and covered with a chromium layer. Its surface is of minor quality as some scratches and pores are visible, but it has proved to give sufficient contrast.

The window was purchased from Schott in Mainz, Germany. It is made from tempered B.K.7 glass, 300 mm ⌀ and 35 mm thick.

The experience with the flash lamp will be described in § 13. Its actual position is not in the optical center of the mirror because we use a condensing system. An image of the light arc is formed in the optical center of the mirror. We call this image the effective light source.

The condensing system serves for different purposes, as will be described in § 12. It resembles an arrangement of optical components as normally used in lantern-slide projectors: there is a condenser (1 : 2), a "diapositive" and a projecting lens, the latter one placed where the condenser forms the effective light source. The diapositive is projected into a plane near the chamber. Besides other advantages this allows to have a sharply cut light cone in the neighborhood of the chamber in spite of the finite size of the light source. Thus the background is considerably improved.

We work with 3 cameras using unperforated 35 mm film. The objectives are placed on a circle with a diameter of 230 mm around the effective light source. They have a focus of 100 mm and are used with a stop between 20 and 30. The actual demagnification is $m = 10$ regarding the image of the mirror on the film.

All glass parts of our optical system are coated, including the chamber window. Special care was taken to avoid reflection of the blue light which is predominantly emitted by the used flash lamp General Electric FT 230. About 1.4% is still reflected at each surface.

§ 11. *Bubble and source images.* In this section we will compare the amount of light a bubble scatters into a camera with how much parasitic light comes there by reflection at the window surfaces. The considerations are related to our illumination and photographic system, but they apply to other arrangements of the optical components, too.

The relative refractive index between liquid hydrogen and the vapor inside the bubbles at 27°K is ca. 1.10. Consequently light is scattered mainly in the forward direction. Usually the angular distribution of the scattered light is described by $I(\vartheta, r, R) = (r/R)^2 G(\vartheta)\, I_0$, where I_0 is the intensity of the incoming light at the position of the bubble, R is the distance at which $I(\vartheta, r, R)$ is measured and r is the radius of the bubble. I_0 is assumed to be constant throughout the chamber volume. $G(\vartheta)$ is the distribution function which contains all physical informations. It can be calculated using geometrical theory, see ref. 13) and fig. 9. Conservation of light energy imposes the restriction on $G(\vartheta)$ that $\bar{G}^{\cos\vartheta} \leqslant \frac{1}{4}$. This follows from

$$I_0\, \pi r^2 \text{ (total incident light)} \geqslant$$

$$\int_0^\pi I(\vartheta, r, R) \sin\vartheta\; 2\pi R^2\, \mathrm{d}\vartheta \quad \text{(total scattered light)}$$

G has the constant value of $\frac{1}{4}$ if all the light which falls on a bubble is isotropically scattered. One sees from fig. 9 how much $G(\vartheta)$ actually exceeds this average value for small ϑ.

Our cameras view the bubbles at an angle $\vartheta_0 = 5.8°$ from the direction of the unscattered light. The distribution function has the value $G(5.8) = 15$.

In the following we use the approximation of paraxial rays. For simplicity it is assumed that the distance between film and objective in our cameras equals the focal length f. The light which a bubble scatters into the iris of a camera amounts to $(r/R)^2 G(\vartheta_0)(f/F)^2 I_0 \pi/4$.

F is the stop number of the objective and R its distance from the bubble. This light is focussed into the area $\pi r^2(f/R)^2$ on the film. Consequently the bubble image receives the light per unit area $G(\vartheta_0)I_0/(4F^2)$.

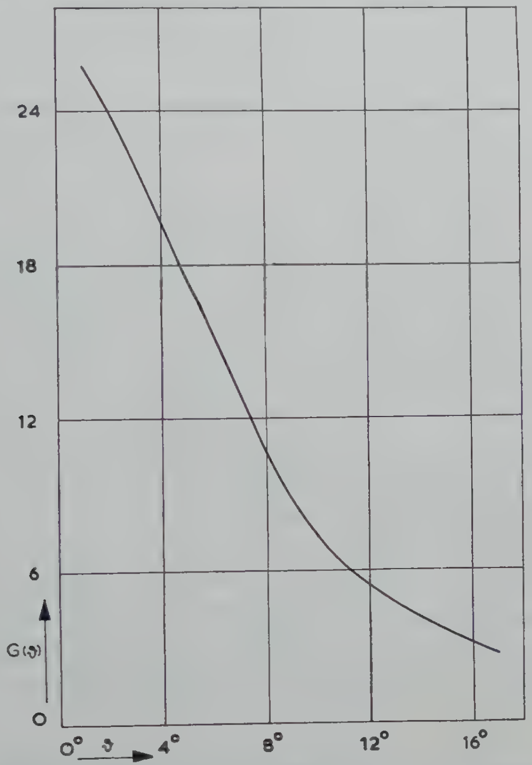

Fig. 9. Distribution function of light scattered by a spherical bubble in liquid hydrogen. The curve is calculated for $n_{\mathrm{rel}} = 1.1$ [8]).

On the film appear images of the light source, too. These are due to single or multiple reflection of light at the window surfaces. In general they do not represent sharp images because they are out of focus. We will derive an expression for the amount of light focussed into these source images. First two definitions: We use the word parasitic when the effects of light reflection by the window are meant. For example, a parasitic source image is formed by light, which has undergone at least one parasitic reflection by the window. Furthermore, the order n of a source image indicates how many parasitic reflections have taken place before the image is formed.

At each parasitic reflection the intensity decreases as only $\rho\%$ are reflected. ρ equals 4 without coating and ca. 1 with single coating. If the flash light is filtered and double coating applied, ρ can be reduced to about 0.1.

To a source image on the film corresponds a real or virtual image in the object space. The total light collected there is

$$(\rho\cdot 10^{-2})^{\mathrm{n}} I_0 \pi R^2_{\mathrm{glass}}\,.$$

$2R_{\mathrm{glass}}$ is the diameter of the window. The light sent through the iris of a camera amounts to

$$(\rho\cdot 10^{-2})^{\mathrm{n}}\,(r_{\mathrm{i}}/r_0)^2\,(R_0/R_{\mathrm{i}})^2\,(f/F)^2\,I_0\pi/4.$$

Here r_{i} is the radius of an image in the object space, R_{i} its distance from the camera, r_0 is the radius of the light source, i.e. the effective one in our case, and R_0 the distance between the light source and the window.

The source image on the film receives the light per unit area:

$$(\rho\cdot 10^{-2})^{\mathrm{n}}\,(R_0/r_0)^2\,I_0/4F^2.$$

As a matter of fact, with our illumination system one finds source images of every order as consequence of the use of a spherical mirror, unless they become invisible by lack of light intensity. Especially the brightest images with $n = 1$ are rather disturbing, as we will show by comparison with the bubble images. In chambers with two windows, where straight-through-illumination is used, no source images of uneven order can appear on the film. Therefore the question of how to avoid source images becomes less important in this case.

The achievable contrast between bubble and source images depends on the ratio k of the light per unit film area for both of them, $k = G(\vartheta_0)(\rho\cdot 10^{-2})^{-\mathrm{n}}\,(r_0/R_0)^2$. This equation shows that k assumes a higher value for larger $G(\vartheta_0)$ i.e. smaller ϑ_0, and for larger r_0/R_0. Thus for the contrast between bubble and source images it is advantageous to photograph at small ϑ_0 and to illuminate the chamber by an extended light source.

Taking the actual values of our design, $R_0 = 90$ cm and $r_0 = 1.2$ cm we obtain:

$k = 6.7 \times 10^{-2}$ for $n = 1$ and $\rho = 4$ (uncoated)
$k = 2.7 \times 10^{-1}$ for $n = 1$ and $\rho = 1$ (coated)
$k = 1.7$ for $n = 2$ and $\rho = 4$ (uncoated)
$k = 27$ for $n = 2$ and $\rho = 1$ (coated) etc.

It is desirable to distinguish a bubble image even if it coincides with a source image. It would be better if one could keep the source image completely invisible. Therefore k should have as high a value as possible but definitely $\geqslant 4$ for all parasitic source images which appear on the film. For example the Agfa films Agepe and Agepan can be used with a gradation of 3.7. This would be enough to suppress a source image when $k = 4$. In our practical case however, some source images overlap which makes the contrast worse. Therefore if a source image shall not disturb the photography of bubbles its k-value must be well above 4.

It is a characteristic feature of the used illumination system in our construction, that the brightness of source images of the first order is strongly reduced on the film. In § 12 a detailed description is given of this system.

As to source images of the second order the above table of k-values shows that coating of the chamber window reduces their brightness sufficiently to render them harmless. Our experience has confirmed this conclusion.

Higher order source images remain invisible by lack of light intensity. But there may occur source images due to reflection at glass surfaces other than of the chamber window. For example coating and tilting of the window on the vacuum tank where the flash light enters has helped considerably to suppress disturbing source images.

§ 12. *Illumination system.* In our illumination and photographic system two source images of the first order occur unless some special tricks are applied.

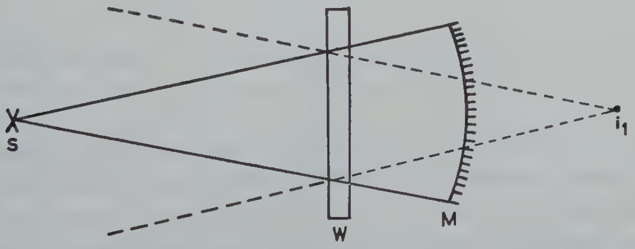

Fig. 10. The "first image" i_1 of the light source s. w means window and m mirror. Dashed lines indicate parasitic light, thin lines virtual light.

The first image is caused by a reflection of the incoming light at the window surface. A virtual 1 : 1 image is formed at twice the distance "window-light source", which is seen by the cameras (see fig. 10). In fact this virtual image occurs twice as both surfaces of the window are reflecting.

The second image is also caused by a single parasitic reflection, but this time the spherical mirror is involved, as shown in fig. 11. The light is first reflected by the mirror, then by the window and finally by the mirror again before it falls into the irises of the cameras. Or in the language of geometrical optics: the mirror forms an image of the light source which coincidences with the light source itself; by intervention of a parasitic reflection at the window this image is transformed into a virtual one behind the mirror; the mirror then transforms this parasitic image into a real one in front of the window. We refer to this last image i_2 as to the second image. Its distance from the cameras is about half the distance between the first parasitic image and the cameras, and its size is about half the size of the light source. Therefore the cameras see both images equally bright and large. Again, the second parasitic source image occurs twice, as light is reflected at both sides of the window.

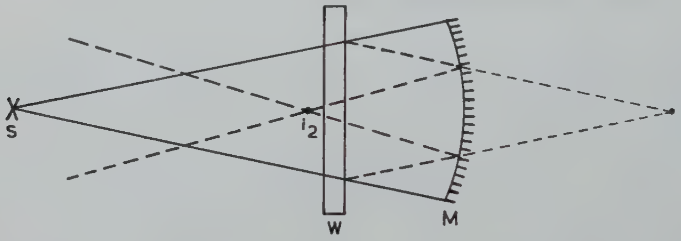

Fig. 11. The "second image" i_2 of the source s.

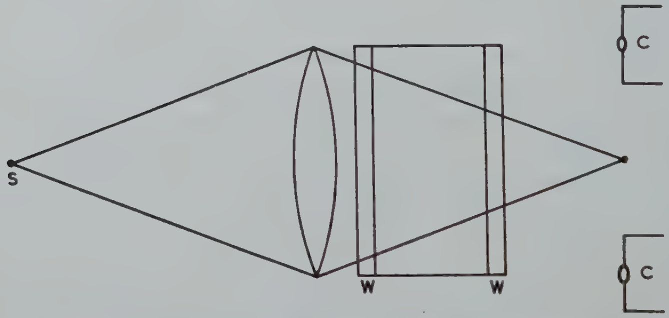

Fig. 12. Illumination of a bubble chamber by a convergent light beam. c stands for camera, s for light source and w for window.

A way to avoid parasitic source images of the first order was proposed by Courant 14). As an introduction we shall sketch two other illumination techniques used in bubble chamber work. In chambers with two vertical windows bubbles are normally photographed in a convergent light beam as shown in fig. 12. No source images of the first order appear on the film, only second order images whose brightness is reduced by coating the window.

Block *et al.*4) followed another method to obtain dark field illumination in their helium chamber. On one side of their chamber a diffuse light screen serves as a light source. A lens forms an image of the screen in a plane on the opposite side of the chamber where the cameras are placed. The relative positions of the screen, the lens, the chamber windows and the camera plane can be seen in fig. 13. The areas on the screen are blackened the images of which coincide with the irises of the cameras. Consequently no direct light falls into the cameras. There are still parasitic reflections, but because cameras and light source are on opposite sides of the chamber, only parasitic source images of the second and higher orders appear. They are barely visible on the film and cover a large area because an extended diffuse light source is used.

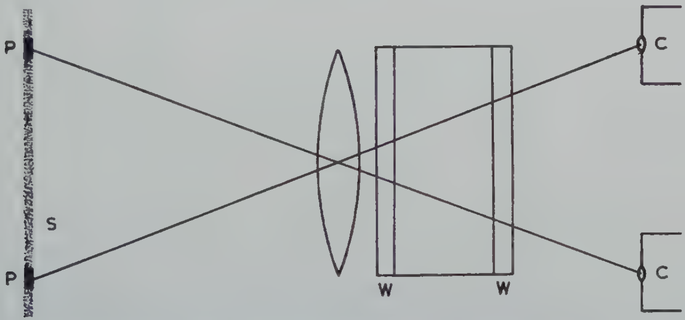

Fig. 13. Illumination of a bubble chamber by diffuse light. *p* indicates a black patch on the diffuse screen *s*, which serves as a light source. The image of *p* covers the iris of a camera *c*. *w* stands for window.

Now Courant proposes to combine these two systems in the following manner: 1. A pointlike source is used. By a condensing lens *co* its light is focussed into a real image *e* which is called the effective light source. A spherical mirror reprojects this effective source onto itself, as shown in fig. 14*a*. The cameras are arranged on a circle around the effective source. 2. A diapositive *d* is located in the light beam immediately after it has left the condensing system. Its function can be understood from fig. 14*b*. A projecting lens *o* is placed where the effective source appears. The projected light which is reflected at the window surface, forms an image of the diapositive in the camera plane. Parasitic light of the first order is kept off the cameras *c*, if the areas on the diapositive, whose images coincide with the camera irises, are blackened.

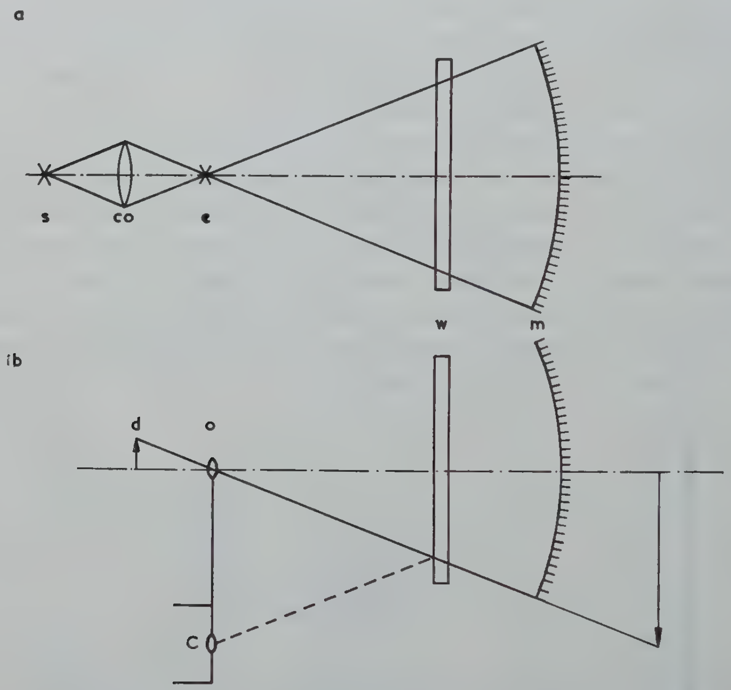

Fig. 14a and b. The direct light (a) and the parasitic light (b) in an illumination system with one window *w* and a mirror *m*, according to Courant 13). *s* means light source; *d* the diapositive of which the projecting lens *o* forms an image in the plane of the camera *c*. This image is a parasitic one of the first order as indicated by the dashed line. *co* stands for collimator.

In other words, a spherical mirror hinders the entrance of parasitic light of zero order (direct light) into the cameras in analogy to the illumination method using a convergent light beam. The Block method simultaneously prevents the appearence of parasitic source images of the first order on the film.

We adapted the proposal of Courant in our illumination system. The use of a simple spherical mirror at the bottom of the chamber makes some modifications and precautions necessary, which will now be discussed. So far as we know we are the first who have brought the ideas of Courant into practice.

Courant assumes in his paper that a rectrograde reflector such as the Berkeley coat hanger system [6]) is used which casts back the direct light but absorbs all scattered and parasitic light, that falls on it. Therefore he only deals with the first source image, whereas in our case two source images occur. We must twice apply the trick of Courant to get rid of the second source image on the film, too. This is done by using a thick diapositive, bearing one set of black patches on either side. Following the path of the parasitic light, one set of them is projected onto the camera irises just as described above. The other set renders harmless the parasitic light, which forms the second source image in front of the chamber window.

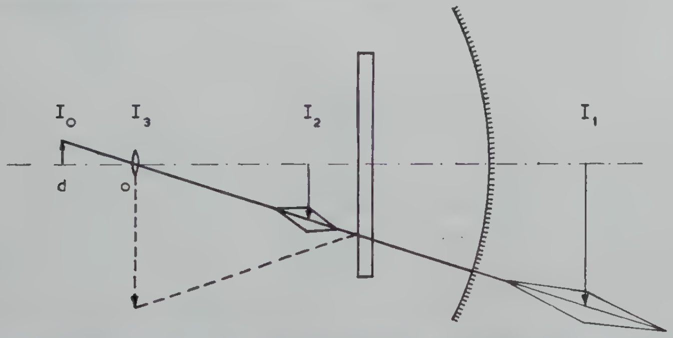

Fig. 15. First step to subdue parasitic source images. The light of the first source image which otherwise falls into the cameras, is extinguished by an absorbing patch I_0. Full lines indicate direct light, thin lines the light coming from virtual images and dashed lines the light after one parasitic reflection.

These facts are illustrated in figs. 15 and 16. The I_i and II_i represent one black patch or its images out of each set. The index $i = 0, 1, 2, 3$ denotes the plane in which I_i or II_i are situated. $i = 0$ is the plane of the diapositive, $i = 1$ and $i = 2$ the planes containing the first and the second source image respectively, and $i = 3$ the camera plane. The images of the black patches are surrounded by dark areas which resemble cigars. These are the regions where no direct light comes as the consequence of the shadowing effect of the black patches. They should not extend into the chamber volume and render certain regions there unusable.

We first describe the sequence of images I_0–I_1–I_2–I_3 as shown in fig. 15. I_1 is an image of the black patch I_0 formed by the projecting lens *o*. This image is virtual, as no light penetrates the spherical mirror. A part of the light undergoes a parasitic reflection by the window and forms I_3, but most of the light is reflected by the spherical mirror which transforms the virtual image into the real image I_2. I_3 coincides with the iris of a camera, and this is the only intended result. Everything else is incidental and must not disturb the illumination. I_1 and I_2 are situated outside the chamber. Working with a small stop in the projecting objective *o* and a large enough light source we can keep the unilluminated regions around I_1 and I_2 out of the chamber, too. I_1 and I_2 stand for three images each as we work with three cameras and need one I_3 per camera iris.

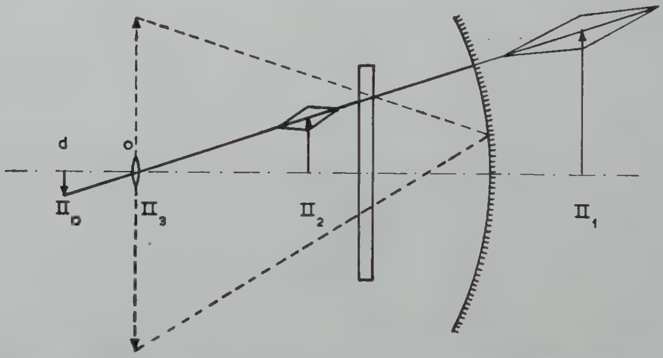

Fig. 16. Second step to subdue parasitic source images. The black patch II_0. absorbs the light of the second source image, which otherwise would fall into the cameras. Thin dashed lines mark the way of light from virtual parasitic source images, the other lines as in fig. 15.

Next we shall consider the sequence of the images II_0–II_1–II_2–II_3 as shown in fig. 16. Here II_2 is an image of II_0 formed by the objective *o*. Note that I_0 and II_0 lie on opposite surfaces of the ca. 15 mm thick diapositive. Therefore their images appear in very different planes. Now II_2 is transformed into the virtual image II_1 by the spherical mirror. Up to this point we only deal with the direct light, which is not seen by the cameras. The returning light, however, undergoes a parasitic reflection at the window. From II_1

this reflection forms a virtual image in the camera plane. The final step is that the spherical mirror produces the real image II_3 from the virtual one in the camera plane. II_3 is made to coincide with the iris of a camera. The consequence is that also the parasitic light which is successively reflected by the mirror, by the window, and by the mirror again, is kept off the cameras. II_1 and II_2 stand for the centers of three dark cigars each, so that in total there are twelve dark regions. All of them occur outside the chamber volume.

In practice the diapositive consists of a transparent polished lucite or glass window whereon arc segments are drawn with a pair of compasses, using black ink. These are the black patches mentioned above. Their right positions and thicknesses have been found by trial until the first order images of the light source on the films became nearly invisible.

The fact that a clear transparent diapositive is used instead of a diffuse one has the consequence, that the minimum effective stop of the objective *o* depends on the size of the effective light source *e*. In our practical case the maximum diameter of the iris of *o* equals the diameter of *e*.

Because of internal reflections in the objective *o* and due to parasitic reflections of the returning direct light at the diapositive *d*, at *o*, and at the window *p* on top of the vacuum tank (see fig. 17), the source images on the film at the place of the discussed first order source images cannot be totally extinguished. The art is to subdue their brightness by coating of the optical components and by tilting of *p* so that they do not disturb the photography of bubbles whose image on the film coincides with these source images.

For all details see the caption of fig. 17 which summarizes our actual design. In the drawing refraction effects in the glass windows and in the chamber liquid are omitted. In place of double images due to parasitic reflection at both window surfaces, simple images are drawn between the actual double images. When the lengths of the unilluminated regions were evaluated an enlargement due to this double occurrence was taken into account.

The diapositive plays another role as mentioned already. Because we work with an extended light source, it is impossible to have a sharply cut light cone projected into the chamber just by screening off the unwanted light with the help of an aperture between *e* and *p* (see fig. 17). We achieve homogeneous illumination of the chamber

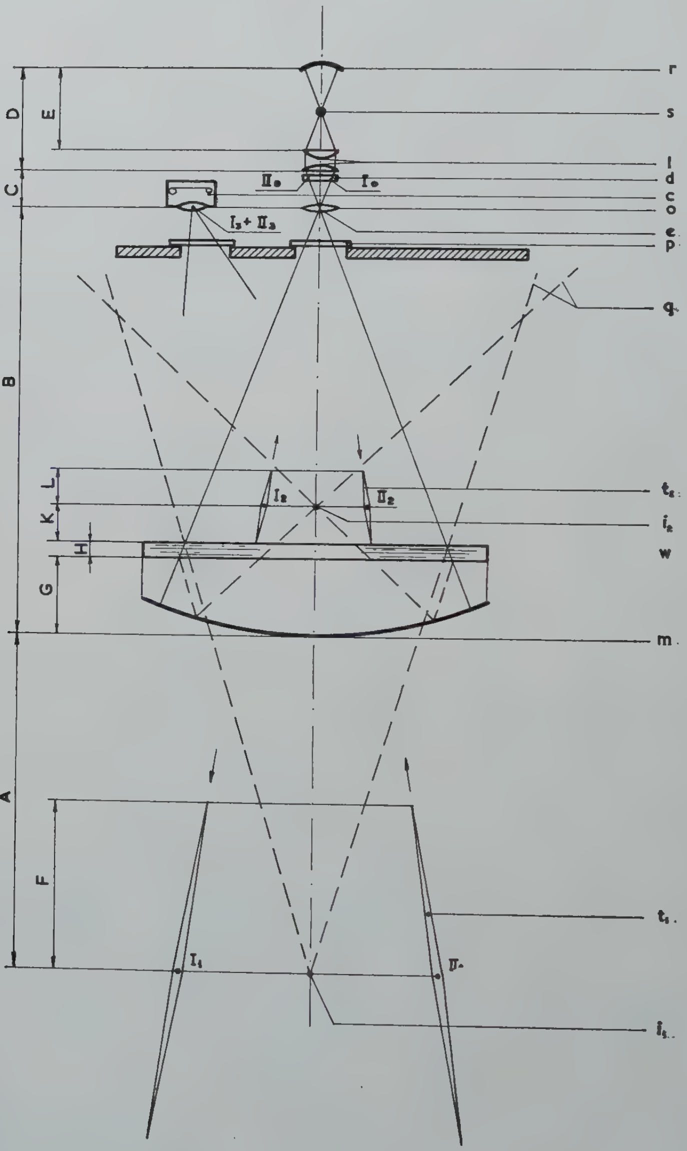
r
s
l
d
c
o
e
p
q
D
E
C
B
II_0
I_0
$I_3 + II_3$
L
K
H
G
I_2
II_2
t_2
i_2
w
m
A
F
I_1
II_1
t_1
i_1

Fig. 17. General arrangement of optical components of the Leiden-chamber. All distances parallel to the optical axis are 1/20th of the true dimensions, whereas perpendicular to the axis this ratio is 3/20. Effects due to the refractive index of the glass windows and of liquid hydrogen are neglected in the drawing. These effects cause the I_1 and the II_1 as well as the I_2 and the II_2 to fall in slightly different planes. Note that I_i and II_i stand for three images each.

r	reflector increasing the light efficiency; radius of curvature 59 mm, 54 mm ⌀.
s	flash lamp, G.E. FT 230, maximum loading 200 J, ca 12 mm arc diameter.
l	collimator, forming the 1 : 2 image e; two plane convex lenses of 47 mm ⌀, f = 118 mm and f = 60 mm.
d	diapositive, ca. 15 mm thick, with three black patches on either side.
c	camera. Boyer Aposaphir 1 : 10/100; used with a stop between 20 and 30; mounted on a Beatty film magazine. Three cameras are viewing the chamber, placed on a circle around e with 230 mm ⌀.
o	projecting objective, Schneider Radionar 1 : 4.5/105.
e	effective light source at the position of o.
p	glass windows at room temperature, on top of the vacuum tank; the central one is tilted.
q	cones of the parasitic light from the first and the second source image.
t_2	one of the six black tunnels (cigars) near the plane of the second image; the arrows on top of the cigars indicate, whether these regions of total shadow occur in the incident light (II_2) or in the light directed towards the cameras (I_2). Diameter amd length of these tunnels are 2.2 mm and 170 mm respectively. The length of tunnels is given taking into account reflection at both sides of the window. Actually two nearly coinciding tunnels are formed each time. Both of them fall inside the given t_i, i = 1,2.
i_2	second source image.
w	chamber window, 35 mm thick, tempered BK 7 glass, 300 mm ⌀, coated.
m	spherical mirror, radius of curvature 1209 mm, metallic.
t_1	one of the six virtual tunnels near the plane of the first source image.; diameter and length of these tunnels are 5 mm and 900 mm respectively.
i_1	first source image.

A = 770 mm
B = 1135 mm
C = 123 mm
D = 142.5 mm
E = 118 mm

F = 450 mm
G = 205 mm
H = 35 mm
K = 98 mm
L = 85 mm

without stray light outside the useful volume using the diapositive as aperture to limit the size of the light cone. This is possible because an image of this aperture is formed near the chamber.

§ 13. *Experiences with the flash lamp.* As a light source we use a General Electric FT 230. This lamp has the following specification:

design voltage	2 kV	electrode spacing	3.0–3.5 mm
minimum voltage	1 kV	filling gas	xenon
max. rating	200 J	flash duration ($\frac{1}{3}$ peak)	70 μs *)
trigger voltage	15 kV	flash rate	1/min *)
trigger energy	20 mJ	light colour	370mμ $<\lambda<$ 470 mμ *)
arc diameter	12 mm*)		

*) at maximum rating

Since a Hivolt-12 kV-unit and a thyratron 5C22 were at our disposal, we decided to design a trigger circuit utilizing these elements. The flash power is delivered by a Langham power unit working at 2200 V and 1450 V. The energy is stored in two TCC-Hiconol 33 μF capacitors which can be used in series or parallel or singly.

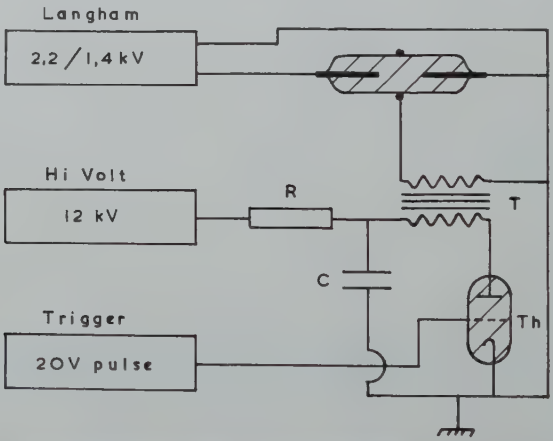

Fig. 18. The flash circuit. *Th* stands for thyratron, *C* for storage capacitor of the trigger pulse, *R* for the charging resistance and *T* for the pulse transformer.

The block scheme is given in fig. 18. The flash is started by a positive 20 V signal sent to the grid of the 5C22. It was not practicable to have a cathode follower as the last stage of the trigger unit, because then the discharge in the 5C22 worked back with fatal consequence for the valves. The discharge of C (see fig. 18) via the thyratron causes a voltage drop of the plate which is transformed by T into a positive pulse and sent to the trigger electrode of the flash lamp. The 1 : 1 transformer T is homemade and consists of twice ten windings wrapped around ferroxcube discs 25 mm in diameter. TV-cable is used for the windings.

The trigger electrode of the flash lamp is a simple copper wire twined around the glass bulb. It is necessary to use a positive triggering pulse higher than 12 kV if the flash lamp is placed in the dark and incidental photoelectrons are absent.

The needed flash energy was determined by experiment. In our illumination system we use only about 6% of the light per flash. 50 joules per flash were sufficient when the diaphragm of the photographic objectives were stopped to F = 22 and the Adox film KB 17 was used.

The FT 230 is a lamp with a very narrow gap between the electrodes. Consequently the resistance during the discharge is considerably smaller than in normal flash lamps. We have determined the discharge resistance to be about $7 \cdot 10^{-2}$ ohms by measuring the damping of a LC-circuit in which the lamp formed the principle load. During the flash the stored energy is dissipated in the lamp and in the cables leading to it, in the ratio of the relative resistances. The needed cables have a length of some meters and conduct several thousand amperes in the short time the flash lasts. The copper cross-section must be at least 15 mm^2.

Acknowledgements. The basic design idea of the described bubble chamber arose from discussions between Prof. Dr. K. W. Taconis, Mr. E. S. Prins and one of the authors (J.R.). The stimulating interest and essential suggestions of Prof. Dr. K. W. Taconis throughout the whole work are gratefully acknowledged. The technical realization of the project has been mainly on hands of Mr. E. S. Prins of the Kamerlingh Onnes Laboratory.

This work was a part of the research program of the "Stichting voor Fundamenteel Onderzoek der Materie" (F.O.M.) and was made possible by financial support from the "Stichting voor Zuiver Wetenschappelijk Onderzoek" (Z.W.O.).

Received 18th August 1961

REFERENCES

1) Glaser, D. A., Phys. Rev. **87** (1952) 665 (L).
Glaser, D. A., Nuovo Cimento **11** suppl. 2 (1954) 361.
Glaser, D. A., Phys. Rev. **91** (1953) 762 (L).
Glaser, D. A., Handbuch der Physik, Springer, Berlin 1958, p. 314.
2) Seitz, F., Phys. Fluids **1** (1958) 2.
3) Goldburg, W. I., Phys. Fluids **1** (1958) 353.
4) Block, M. M., W. M. Fairbank, E. M. Harth, T. Kikuchi, C. Meltzer and J. Leitner, Proc. Int. Conf. on High Energy Accelerators and Instrumentation CERN 1959.
5) Eisler, F., R. Plano, A. Prodell, N. Samios, M. Schwartz, J. Steinberger, P. Bassi, V. Borelli, G. Puppi, H. Tanaka, P. Waloschek, V. Zoboli, M. Conversi, P. Franzini, I. Mannelli, R. Santangelo and V. Silvestrini, Nuovo Cimento **10** (1958) 468.
6) Chelton, D. B., D. B. Mann and R. A. Byrns, Proc. Cryogenic Eng. Conf., Boulder, 1956.
Gow, J. D. and A. H. Rosenfeld, Proc. Int. Conf. on High Energy Accelerators and Instrumentation CERN 1959.
7) CERN-report 4790/e.
8) Riddiford, L., H. B. van de Raay, N. C. Barford, C. C. Butler, D. McMullan, A. Thetford, D. B. Thomas, W. T. Welford, A. Amery, W. H. Evans, M. J. Moore, P. Polak, H. W. B. Skinner, P. R. Williams, D. Shaw, A. G. Ashburn and M. Snowden, Proc. Int. Conf. on High Energy Accelerators and Instrumentation CERN 1959.
9) Donaldson, R. and R. Watt, UCRL Eng. Note 4311–17/M19.
10) Budde, R., A. Burger, H. Filthuth, Y. Goldtschmidt-Clermont, H. M. Mayer, D. R. O. Morrison, Chr. Peyrou and J. Trembley, Nuovo Cimento **11** (1959) 778.
11) Derado, I., and N. Schmitz, Nuovo Cimento **11** (1959) 887.
12) Miner-Seastone, Handbook of Engineering Materials, John Wiley & Son, 1955, p. 4–145.
13) Davis, G. E., J.O.S.A. **45** (1955) 572.
14) Courant, H., Proc. Int. Conf. on High Energy Accelerators and Instrumentation CERN 1959.
15) Bradner, H., UCRL-report 9199 *).
16) Bugg, D. V., Progress in Nuclear Physics Vol. 7, Pergamon Press, London, 1959 *).

---

*) Recent general articles on bubble chambers, not cited in the text.

Appl. sci. Res. Section B, Vol. **9**

DEFORMATION OF PIEZOELECTRIC PLATES

by H. S. PAUL

Department of Mathematics Indian Institute of Technology, Kharagpur, India

Summary

General equations in two-dimensional statical problems of piezoeletricity have been deduced by introducing the Airy stress function and the electric potential. Particular solutions for quartz plates have been obtained in two problems. The first problem is that of lateral bending by shearing forces at one edge while the second one is concerned with the deformation due to uniformly distributed normal forces.

§ 1. *Introduction.* Although much experimental work on piezoelectric material has already been done 1)2), theoretical work on it, from a strictly mathematical point of view, has got fresh impetus only in recent years. A detailed reference to it may be found in a paper by Paria 3). Later on Jerrad 4) has also solved a problem of vibration of quartz crystal plates. The particular cases of statical problems are comparatively easy to solve, especially when quartz plates are concerned.

In this paper, general equations in two-dimensional statical problems have been formulated in terms of the Airy stress function and the electrical potential. The solutions of these equations have been obtained in two special problems of quartz plates. The first one is that of bending of plates by shearing forces applied at one end with the other end clamped. The second problem is concerned with determining the deformation in a plate produced by a uniformly distributed load on the upper edge when it is supported by shearing forces. The corresponding results for non-piezoelectric isotropic material 5) have been deduced as particular cases.

§ 2. *Basic equations.* We consider the deformation of the thin rectangular plate of piezoelectric material when mechanical forces are applied to its edges. We choose the axis of z along a normal to the plate while the axes of x and y are parallel to the edges. If the deformations are parallel to the plane of the plate, the relevant stress components are T_1, T_2 and T_6 (p. 69 [2])), and these satisfy the equations of equilibrium

$$\begin{aligned} \frac{\partial T_1}{\partial x} + \frac{\partial T_6}{\partial y} &= 0, \\ \frac{\partial T_6}{\partial x} + \frac{\partial T_2}{\partial y} &= 0. \end{aligned} \tag{2.1}$$

The electrical displacements D_1 and D_2 parallel to the axes of x and y satisfy the Gauss's equation

$$\frac{\partial D_1}{\partial x} + \frac{\partial D_2}{\partial y} = 0. \tag{2.2}$$

The corresponding strain components s_1, s_2 and s_6 satisfy the compatibility equation

$$\frac{\partial^2 s_1}{\partial y^2} + \frac{\partial^2 s_2}{\partial x^2} = \frac{\partial^2 s_6}{\partial x \partial y}. \tag{2.3}$$

The electric field components E_1 and E_2 are assumed to be derivable from a potential φ so that

$$E_1 = -\frac{\partial \varphi}{\partial x}, \quad E_2 = -\frac{\partial \varphi}{\partial y}. \tag{2.4}$$

The piezoelectric relations [6]) required in the present case are

$$\begin{aligned} s_1 &= s_{11}^E T_1 + s_{12}^E T_2 + s_{16}^E T_6 + d_{11} E_1 + d_{21} E_2, \\ s_2 &= s_{12}^E T_1 + s_{22}^E T_2 + s_{26}^E T_6 + d_{12} E_1 + d_{22} E_2, \\ s_6 &= s_{16}^E T_1 + s_{26}^E T_2 + s_{66}^E T_6 + d_{16} E_1 + d_{26} E_2, \\ D_1 &= d_{11} T_1 + d_{12} T_2 + d_{16} T_6 + \varepsilon_{11}^T E_1 + \varepsilon_{12}^T E_2, \\ D_2 &= d_{21} T_1 + d_{22} T_2 + d_{26} T_6 + \varepsilon_{21}^T E_1 + \varepsilon_{22}^T E_2, \end{aligned} \tag{2.5}$$

where the coefficients have their usual meaning.

Equations (2.1) are satisfied if

$$T_1 = \frac{\partial^2 \chi}{\partial y^2}, \quad T_2 = \frac{\partial^2 \chi}{\partial x^2}, \quad T_6 = -\frac{\partial^2 \chi}{\partial x \partial y}. \tag{2.6}$$

By substituting from (2.4) and (2.6) in the first three equations of (2.5), we find expression for s_1, s_2 and s_6 in terms of χ and φ. When these are used in (2.3), there results the equation

$$L(\chi) = M(\varphi), \tag{2.7}$$

where the operators L and M are defined as

$$L = s_{22}^E \frac{\partial^4}{\partial x^4} - 2s_{26}^E \frac{\partial^4}{\partial x^3 \partial y} + (2s_{12}^E + s_{66}^E) \frac{\partial^4}{\partial x^2 \partial y^2} - \\ - 2s_{16}^E \frac{\partial^4}{\partial x \partial y^3} + s_{11}^E \frac{\partial^4}{\partial y^4}, \tag{2.8}$$

$$M = d_{12} \frac{\partial^3}{\partial x^3} + (d_{22} - d_{16}) \frac{\partial^3}{\partial x^2 \partial y} + (d_{11} - d_{26}) \frac{\partial^3}{\partial x \partial y^2} + d_{21} \frac{\partial^3}{\partial y^3}. \tag{2.9}$$

Similarly, if D_1 and D_2 in (2.5) are expressed in terms of χ and φ with the help of (2.4) and (2.6), the equation (2.2) gives

$$M(\chi) = N(\varphi), \tag{2.10}$$

where the operator N is defined as

$$N = \varepsilon_{11}^T \frac{\partial^2}{\partial x^2} + 2\varepsilon_{12}^T \frac{\partial^2}{\partial x \partial y} + \varepsilon_{22}^T \frac{\partial^2}{\partial y^2}. \tag{2.11}$$

Equations (2.7) and (2.10) show that χ and φ satisfy the same differential equation, that is

$$(LN - M^2)(\chi, \varphi) = 0, \tag{2.12}$$

where the operator $LN - M^2$ is given by

$$LN - M^2 =$$

$$= (\varepsilon_{11}^T s_{22}^E - d_{12}^2) \frac{\partial^6}{\partial x^6} + 2(\varepsilon_{12}^T s_{22}^E - \varepsilon_{11}^T s_{26}^E - d_{12} d_{22} + d_{12} d_{16}) \frac{\partial^6}{\partial x^5 \partial y}$$

$$+ [\varepsilon_{11}^T (2s_{12}^E + s_{66}^E) - 4\varepsilon_{12}^T s_{26}^E + \varepsilon_{22}^T s_{22}^E - 2d_{12}(d_{11} - d_{26}) - (d_{22} - d_{16})^2] \frac{\partial^6}{\partial x^4 \partial y^2}$$

$$+ 2[\varepsilon_{12}^T (2s_{12}^E + s_{66}^E) - \varepsilon_{11}^T s_{16}^E - \varepsilon_{22}^T s_{26}^E - d_{12} d_{21} - (d_{11} - d_{26})(d_{22} - d_{16})] \frac{\partial^6}{\partial x^3 \partial y^3}$$

$$+ [s_{11}^E \varepsilon_{11}^T - 4\varepsilon_{12}^T s_{16}^E + \varepsilon_{22}^T (2s_{12}^E + s_{66}^E) - 2d_{21}(d_{22} - d_{16}) - (d_{11} - d_{26})^2] \frac{\partial^6}{\partial x^2 \partial y^4}$$

$$+ 2(\varepsilon_{12}^T s_{11}^E - \varepsilon_{22}^T s_{16}^E - d_{21} d_{11} + d_{21} d_{26}) \frac{\partial^6}{\partial x \partial y^5} + (\varepsilon_{22}^T s_{11}^E - d_{21}^2) \frac{\partial^6}{\partial y^6}.$$

Solutions of (2.12) consistent with either (2.7) or (2.10) and satisfying prescribed mechanical and electrical boundary conditions determine χ and φ.

§ 3. *Quartz plate.* If the plate is cut from a quartz crystal, we have (p. 54, 191, 162 [1]))

$$\begin{gathered} s^E_{11} = s^E_{22},\ s^E_{16} = s^E_{26} = 0,\ s^E_{66} = 2(s^E_{11} - s^E_{12}), \\ d_{11} = -\,d_{12} = -\,\tfrac{1}{2}d_{26},\ d_{22} = d_{16} = d_{21} = 0, \\ \varepsilon^T_{11} = \varepsilon^T_{22},\ \varepsilon^T_{12} = 0. \end{gathered} \tag{3.1}$$

In this case (2.7), (2.10) and (2.12) reduce respectively to

$$\frac{\partial^4\chi}{\partial x^4} + 2\,\frac{\partial^4\chi}{\partial x^2\partial y^2} + \frac{\partial^4\chi}{\partial y^4} = \frac{d_{11}}{s^E_{11}}\left(3\,\frac{\partial^3\varphi}{\partial x\partial y^2} - \frac{\partial^3\varphi}{\partial x^3}\right), \tag{3.2}$$

$$\frac{d_{11}}{\varepsilon^T_{11}}\left(3\,\frac{\partial^3\chi}{\partial x\partial y^2} - \frac{\partial^3\chi}{\partial x^3}\right) = \frac{\partial^2\varphi}{\partial x^2} + \frac{\partial^2\varphi}{\partial y^2}\,, \tag{3.3}$$

$$\left[(1-k^2)\,\frac{\partial^6}{\partial x^6} + 3(1+2k^2)\,\frac{\partial^6}{\partial x^4\partial y^2} + \right. \\ \left. + 3(1-3k^2)\,\frac{\partial^6}{\partial x^2\partial y^4} + \frac{\partial^6}{\partial y^6}\right](\chi,\varphi) = 0, \tag{3.4}$$

where

$$k^2 = \frac{d^2_{11}}{\varepsilon^T_{11}s^E_{11}}\,. \tag{3.5}$$

The dimensionless constant k^2 is the electromechanical coupling factor. In purely elastic problems we have $k^2 = 0$.

In the following section we shall solve some special problems by utilizing (3.2), (3.3) and (3.4).

§ 4. *Rectangular plate with one end fixed.* We consider a rectangular plate of small thickness $2h$. Let the edges of the plate be given by $x = 0$, $x = l$, $y = \pm\, c$. We take the edge $x = 0$ to be fixed. The stress function χ [5]), given by

$$\chi = \frac{W}{8c^3h}\,(xy^3 - ly^3 - 3c^2xy), \tag{4.1}$$

corresponds to the stresses

$$T_1 = -\frac{3W}{4c^3h}y(l-x), \quad T_2 = 0, \quad T_6 = \frac{3W}{8c^3h}(c^2-y^2). \tag{4.2}$$

Evidently the edges $y = \pm c$ are free from stresses, while on the edge $x = l$ the normal stress T_1 is zero and the shear stress T_6 has a resultant W. It can be easily verified that (4.1) is a solution of (3.4); substituting from (4.1) in (3.2) and (3.3) we obtain

$$3\frac{\partial^3\varphi}{\partial x\partial y^2} - \frac{\partial^3\varphi}{\partial x^3} = 0, \tag{4.3}$$

$$\frac{\partial^2\varphi}{\partial x^2} + \frac{\partial^2\varphi}{\partial y^2} = \frac{9Wd_{11}}{4\varepsilon_{11}^T c^3h}y. \tag{4.4}$$

Differentiating (4.4) with respect to x and using (4.3), we obtain

$$\frac{\partial^3\varphi}{\partial x^3} = 0, \quad \frac{\partial^3\varphi}{\partial x\partial y} = 0. \tag{4.5}$$

The first equation gives

$$\varphi = \tfrac{1}{2}x^2f_1(y) + xf_2(y) + f_3(y), \tag{4.6}$$

which when substituted in the second equation implies that

$$xf_1'' + f_2'' = 0,$$

that is

$$f_1 = A_1y + B_1, \; f_2 = A_2y + B_2. \tag{4.7}$$

Substitution from (4.6) and (4.7) in (4.4) determines f_3 as

$$f_3 = \frac{3d_{11}W}{8\varepsilon_{11}^T c^3h}y^3 - \tfrac{1}{6}A_1y^3 - \tfrac{1}{2}B_1y^2 + A_3y + B_3. \tag{4.8}$$

Thus

$$\varphi = \tfrac{1}{2}x^2(A_1y + B_1) + x(A_2y + B_2) + \\ + \left(\frac{3d_{11}W}{8\varepsilon_{11}^T c^3h} - \frac{1}{6}A_1\right)y^3 - \tfrac{1}{2}B_1y^2 + A_3y + B_3. \tag{4.9}$$

If the edges $y = \pm c$ are kept at constant potentials φ_2 and φ_1

respectively, then from (4.9) it follows that

$$\begin{aligned} A_1 &= A_2 = B_1 = B_2 = 0, \\ A_3 &= \frac{1}{2c}(\varphi_2 - \varphi_1) - \frac{3d_{11}W}{8\varepsilon_{11}^T ch}, \\ B_3 &= \tfrac{1}{2}(\varphi_2 + \varphi_1). \end{aligned} \tag{4.10}$$

Hence

$$\varphi = \frac{3d_{11}W}{8\varepsilon_{11}^T c^3 h} y^3 + \left[\frac{1}{2c}(\varphi_2 - \varphi_1) - \frac{3d_{11}W}{8\varepsilon_{11}^T ch}\right] y + \tfrac{1}{2}(\varphi_2 + \varphi_1). \tag{4.11}$$

The electric field components are

$$\begin{aligned} E_1 &= 0, \\ E_2 &= -\frac{9d_{11}W}{8\varepsilon_{11}^T c^3 h} y^2 - \frac{1}{2c}(\varphi_2 - \varphi_1) + \frac{3d_{11}W}{8\varepsilon_{11}^T ch}. \end{aligned} \tag{4.12}$$

From (2.5) it follows that the strain components are

$$\begin{aligned} s_1 &= -\frac{3s_{11}^E W}{4c^3 h} y(l - x), \\ s_2 &= -\frac{3s_{12}^E W}{4c^3 h} y(l - x), \\ s_6 &= -\frac{3}{4}\left(s_{11}^E - s_{12}^E - 3\frac{d_{11}^2}{\varepsilon_{11}^T}\right)\frac{W}{c^3 h} y^2 + \\ &\quad + \frac{3}{4}\left(s_{11}^E - s_{12}^E - \frac{d_{11}^2}{\varepsilon_{11}^T}\right)\frac{W}{ch} + \frac{d_{11}}{c}(\varphi_2 - \varphi_1), \end{aligned} \tag{4.13}$$

while the electric displacement components are

$$\begin{aligned} D_1 &= -\frac{3d_{11}W}{4c^3 h} y(l - x), \\ D_2 &= -\frac{3d_{11}W}{8c^3 h} y^2 - \frac{3d_{11}W}{8ch} - \frac{\varepsilon_{11}^T}{2c}(\varphi_2 - \varphi_1). \end{aligned} \tag{4.14}$$

The piezoelectric displacement components u, v can be obtained by integrating the strain components

$$s_1 = \frac{\partial u}{\partial x}, \quad s_2 = \frac{\partial v}{\partial y}, \quad s_6 = \frac{\partial v}{\partial x} + \frac{\partial u}{\partial y}.$$

Integrating both sides of the first two equations of (4.13) with respect to x and y respectively, we obtain

$$
\begin{aligned}
u &= -\frac{3s_{11}^E W}{4c^3h}\,xy(l-\tfrac{1}{2}x) + F_1(y),\\
v &= -\frac{3s_{12}^E W}{8c^3h}\,y^2(l-x) + F_2(x),
\end{aligned}
\tag{4.15}
$$

which, when substituted in the last equation of (4.13), yield

$$
\frac{dF_1}{dy} + \frac{3}{8}\left(2s_{11}^E - s_{12}^E - 6\frac{d_{11}^2}{\varepsilon_{11}^T}\right)\frac{W}{c^3h}\,y^2 + \frac{dF_2}{dx} - \frac{3s_{11}^E W}{4c^3h}\,x(l-\tfrac{1}{2}x) =
$$

$$
= \frac{3}{4}\left(s_{11}^E - s_{12}^E - \frac{d_{11}^2}{\varepsilon_{11}^T}\right)\frac{W}{ch} + \frac{d_{11}}{c}(\varphi_2-\varphi_1).
$$

The above equation is satisfied by taking

$$
\frac{dF_2}{dx} = \frac{3s_{11}^E W}{4c^3h}\,x(l-\tfrac{1}{2}x) + b_1,
$$

$$
\frac{dF_1}{dy} = -\frac{3W}{8c^3h}\left(2s_{11}^E - s_{12}^E - 6\frac{d_{11}^2}{\varepsilon_{11}^T}\right)y^2 + a_1,
$$

where

$$
a_1 + b_1 = \frac{3}{4}\left(s_{11}^E - s_{12}^E - \frac{d_{11}^2}{\varepsilon_{11}^T}\right)\frac{W}{ch} + \frac{d_{11}}{c}(\varphi_2-\varphi_1).
$$

Hence

$$
F_1(y) = -\frac{3}{24}\left(2s_{11}^E - s_{12}^E - \frac{6d_{11}^2}{\varepsilon_{11}^T}\right)\frac{W}{c^3h}\,y^3 + a_1y + a_2,
$$

$$
F_2(x) = \frac{3s_{11}^E W}{8c^3h}\,x^2(l-\tfrac{1}{3}x) + b_1x + b_2.
$$

The constants a_2 and b_2 represent rigid body displacements and hence can be neglected. We also use the condition that the slope of the deflected central line of the plate vanishes at the fixed edge, that is $\partial v/\partial x = 0$ at $x = 0$, $y = 0$. This condition gives $b_1 = 0$.

Thus finally

$$u = -\frac{3s_{11}^E W}{4c^3h} xy(l - \tfrac{1}{2}x) - \frac{3}{24}\left(2s_{11}^E - s_{12}^E - \frac{6d_{11}^2}{\varepsilon_{11}^T}\right)\frac{W}{c^3h} y^3$$

$$+ \left[\frac{3}{4}\left(s_{11}^E - s_{12}^E - \frac{d_{11}^2}{\varepsilon_{11}^T}\right)\frac{W}{ch} + \frac{d_{11}}{c}(\varphi_2 - \varphi_1)\right] y, \quad (4.16)$$

$$v = -\frac{3s_{12}^E W}{8c^3h} y^2(l - x) + \frac{3s_{12}^E W}{8c^3h} x^2(l - \tfrac{1}{3}x).$$

It is seen from (4.13) and (4.16) that the piezoelectric effect modifies only the strain component s_6 and the displacement u. Only one component E_2 of the electric field has a non-vanishing value, while both the components D_1 and D_2 of the electric displacement are present.

For the non-piezoelectric isotropic case

$$d_{11} = 0, \quad s_{11}^E = \frac{1}{E}, \quad s_{12}^E = -\frac{\sigma}{E},$$

and the displacement components take the known values [5]).

$$u = -\frac{3W}{4c^3hE} xy(l - \tfrac{1}{2}x) - \frac{3(2+\sigma)W}{24c^3hE} y^3 + \frac{3(1+\sigma)W}{4chE} y,$$

$$v = \frac{3\sigma W}{8c^3hE} y^2(l - x) + \frac{3W}{8c^3hE} x^2(l - \tfrac{1}{3}x).$$

§ 5. *Rectangular plate with two ends supported.* We consider a rectangular plate of unit thickness placed in a vertical plane [5]). We choose the origin at the centroid with the x and y axes in the horizontal and vertical direction respectively. Let a distributed load q per unit length act on the upper edge $y = -c$. Equilibrium is maintained by supports on the edges $x = \pm l$. The stress function χ, given by

$$\chi = \frac{q}{4c^3}\left[\tfrac{1}{10}y^5 - \tfrac{1}{2}x^2y^3 + \tfrac{1}{2}(l^2 - \tfrac{2}{5}c^2)y^3 + \tfrac{3}{2}c^2x^2y - c^3x^2\right], \quad (5.1)$$

corresponds to the stresses

$$\begin{aligned} T_1 &= \frac{3q}{4c^3}\,[\tfrac{2}{3}y^3 - x^2y + (l^2 - \tfrac{2}{5}c^2)y], \\ T_2 &= -\frac{3q}{4c^3}\,(\tfrac{1}{3}y^3 - c^2y + \tfrac{2}{3}c^3), \\ T_6 &= \frac{3q}{4c^3}\,(xy^2 - c^2x). \end{aligned} \tag{5.2}$$

The mechanical conditions at the upper and lower edges of the plate are

$$(T_6)_{y=\pm c} = 0, \quad (T_2)_{y=c} = 0, \quad (T_2)_{y=-c} = -q.$$

The mechanical conditions at the ends $x = \pm l$ are

$$\int_{-c}^{c} T_6\,\mathrm{d}y = \mp ql, \quad \int_{-c}^{c} T_1\,\mathrm{d}y = 0, \quad \int_{-c}^{c} T_1 y\,\mathrm{d}y = 0.$$

It can be easily verified that (5.1) is a solution (3.4). Substitution from (5.1) in (3.2) and (3.3) gives

$$3\,\frac{\partial^3\varphi}{\partial x\partial y^2} - \frac{\partial^3\varphi}{\partial x^3} = 0, \tag{5.3}$$

$$\frac{\partial^2\varphi}{\partial x^2} + \frac{\partial^2\varphi}{\partial y^2} = -\frac{9d_{11}q}{2\varepsilon_{11}^T c^3}\,xy. \tag{5.4}$$

Differentiating (5.4) with respect to x and using (5.3), we obtain

$$\frac{\partial^3\varphi}{\partial x^3} = -\frac{27qd_{11}}{8c^3\varepsilon_{11}^T}\,y, \qquad \frac{\partial^3\varphi}{\partial x\partial y^2} = -\frac{9qd_{11}}{8c^3\varepsilon_{11}^T}\,y. \tag{5.5}$$

The first equation gives

$$\varphi = -\frac{9d_{11}q}{16\varepsilon_{11}^T c^3}\,x^3y + \tfrac{1}{2}x^2f_1(y) + xf_2(y) + f_3(y), \tag{5.6}$$

which, when substituted in the second equation of (5.5), implies that

$$xf_1'' + f_2'' = -\frac{9d_{11}q}{8\varepsilon_{11}^T c^3}\,y.$$

This is satisfied if

$$\begin{aligned} f_1 &= A_1y + B_1, \\ f_2 &= -\frac{3d_{11}q}{16\varepsilon_{11}^T c^3}\,y^3 + A_2y + B_2 \end{aligned} \tag{5.7}$$

Substitution from (5.6) and (5.7) in (5.4) determines f_3 as

$$f_3 = -\tfrac{1}{6}A_1y^3 - \tfrac{1}{2}B_1y^2 + A_3y + B_3. \tag{5.8}$$

Thus

$$\varphi = \left(-\frac{9d_{11}q}{16\varepsilon_{11}^Tc^3}x^3 + \tfrac{1}{2}A_1x^2 + A_2x + A_3\right)y - \\ - \left(\frac{3d_{11}q}{16\varepsilon_{11}^Tc^3}x + \tfrac{1}{6}A_1\right)y^3 + \tfrac{1}{2}B_1(x^2 - y^2) + B_2x + B_3. \tag{5.9}$$

The condition that the edge $x = l$ is kept at a constant potential φ_1 is satisfied if

$$A_1 = -\frac{9qd_{11}}{8c^3\varepsilon_{11}^T}l, \quad B_1 = 0,$$

$$A_2l + A_3 = \frac{9qd_{11}}{8c^3\varepsilon_{11}^T}l^3, \quad B_2l + B_3 = \varphi_1.$$

Let φ_2 and φ_3 be the average values of φ on the edges $x = -l$ and $y = c$ respectively, that is,

$$\varphi_2 = \frac{1}{2c}\int_{-c}^{c}(\varphi)_{x=-l}\,dy,$$

$$\varphi_3 = \frac{1}{2l}\int_{-l}^{l}(\varphi)_{y=c}\,dx.$$

If the above two conditions are used, then

$$\varphi_2 = -B_2l + B_3,$$

$$\varphi_3 = A_3c + B_3 - \frac{3qd_{11}}{16c^2\varepsilon_{11}^T}l(l^2 - c^2).$$

Thus we finally obtained the coefficients as

$$A_1 = -\frac{9qd_{11}}{8c^3\varepsilon_{11}^T}l, \quad B_1 = 0, \tag{5.10}$$

$$A_2 = \frac{3qd_{11}}{16c^3\varepsilon_{11}^T}(5l^2 + c^2) + \frac{1}{2lc}(\varphi_1 + \varphi_2 - 2\varphi_3), \; B_2 = \frac{1}{2l}(\varphi_1 - \varphi_2),$$

$$A_3 = \frac{3qd_{11}}{16c^3\varepsilon_{11}^T}l(l^2 - c^2) - \frac{1}{2c}(\varphi_1 + \varphi_2 - 2\varphi_3), \; B_3 = \tfrac{1}{2}(\varphi_1 + \varphi_2).$$

Hence

$$\begin{aligned}\varphi = &-\frac{3d_{11}q}{16\varepsilon_{11}^{T}c^{3}}[(x-l)y^{2}+3x^{3}+3lx^{2}-(5l^{2}+c^{2})x-l(l^{2}-c^{2})]y \\ &+\frac{1}{2lc}(\varphi_{1}+\varphi_{2}-2\varphi_{3})(x-l)y+\frac{1}{2l}(\varphi_{1}-\varphi_{2})x+\tfrac{1}{2}(\varphi_{1}+\varphi_{2}).\end{aligned} \tag{5.11}$$

The electric field components are

$$\begin{aligned}E_{1} &= \frac{3d_{11}q}{16\varepsilon_{11}^{T}c^{3}}(y^{2}+9x^{2}+6lx-5l^{2}-c^{2})y- \\ &\qquad -\frac{1}{2lc}(\varphi_{1}+\varphi_{2}-2\varphi_{3})y-\frac{1}{2l}(\varphi_{1}-\varphi_{2}), \\ E_{2} &= \frac{3d_{11}q}{16\varepsilon_{11}^{T}c^{3}}[3(x-l)y^{2}+3x^{3}+3lx^{2}-(5l^{2}+c^{2})x-l(l^{2}-c^{2})]- \\ &\qquad -\frac{1}{2lc}(\varphi_{1}+\varphi_{2}-2\varphi_{3})(x-l).\end{aligned} \tag{5.12}$$

From (2.5), the strain components are

$$\begin{aligned}s_{1} = &\frac{3q}{4c^{3}}\left[\left(\tfrac{2}{3}s_{11}^{E}-\tfrac{1}{3}s_{12}^{E}+\frac{d_{11}^{2}}{4\varepsilon_{11}^{T}}\right)y^{3}+\left(\frac{9d_{11}^{2}}{4\varepsilon_{11}^{T}}-s_{11}^{E}\right)x^{2}y+\frac{3d_{11}^{2}}{2\varepsilon_{11}^{T}}lxy\right] \\ &+\Bigg[\frac{3q}{4c^{3}}\left(l^{2}s_{11}^{E}-\tfrac{2}{5}s_{11}^{E}c^{2}+c^{2}s_{12}^{E}-\frac{5d_{11}^{2}}{4\varepsilon_{11}^{T}}l^{2}-\frac{d_{11}^{2}}{4\varepsilon_{11}^{T}}c^{2}\right)- \\ &-\frac{d_{11}}{2lc}(\varphi_{1}+\varphi_{2}-2\varphi_{3})\Bigg]y-\frac{1}{2}\left[s_{12}^{E}q+\frac{d_{11}}{l}(\varphi_{1}-\varphi_{2})\right], \\ s_{2}= &\frac{3q}{4c^{3}}\left[\left(\tfrac{2}{3}s_{12}^{E}-\tfrac{1}{3}s_{11}^{E}-\frac{d_{11}^{2}}{4\varepsilon_{11}^{T}}\right)y^{3}-\left(\frac{9d_{11}^{2}}{4\varepsilon_{11}^{T}}+s_{12}^{E}\right)x^{2}y-\frac{3d_{11}^{2}}{2\varepsilon_{11}^{T}}lxy\right] \\ &+\Bigg[\frac{3q}{4c^{3}}\left(l^{2}s_{12}^{E}-\tfrac{2}{5}c^{2}s_{12}^{E}+c^{2}s_{11}^{E}+\frac{5d_{11}^{2}}{4\varepsilon_{11}^{T}}l^{2}+\frac{c^{2}d_{11}^{2}}{4\varepsilon_{11}^{T}}\right)+ \\ &+\frac{d_{11}}{2lc}(\varphi_{1}+\varphi_{2}-2\varphi_{3})\Bigg]y-\frac{1}{2}\left[s_{11}^{E}q-\frac{d_{11}}{l}(\varphi_{1}-\varphi_{2})\right], \\ s_{6}= &\frac{3q}{2c^{3}}(s_{11}^{E}-s_{12}^{E})(xy^{2}-c^{2}x)-\frac{3qd_{11}^{2}}{8c^{3}\varepsilon_{11}^{T}}[3(x-l)y^{2}+3x^{3}+3lx^{2}- \\ &-(5l^{2}+c^{2})x-l(l^{2}-c^{2})]+\frac{d_{11}}{cl}(\varphi_{1}+\varphi_{2}-2\varphi_{3})(x-l),\end{aligned} \tag{5.13}$$

while the electric displacement components are

$$
\begin{aligned}
D_1 &= \frac{3qd_{11}}{16c^3}\,[5y^3 + 5x^2y + 6lx] - \left[\frac{3qd_{11}}{16c^3}\left(l^2 + \frac{33}{5}c^2\right) + \right.\\
&\quad \left. + \frac{\varepsilon_{11}^T}{2lc}\,(\varphi_1 + \varphi_2 - 2\varphi_3)\right] y + \frac{1}{2}\left[d_{11}q - \frac{\varepsilon_{11}}{l}\,(\varphi_1 - \varphi_2)\right],\\
D_2 &= \frac{3qd_{11}}{16c^3}\,[3x^3 - 5xy^2 + 3l(x^2 - y^2) - (5l^2 - 7c^2)x - l(l^2 - c^2)] - \\
&\quad - \frac{\varepsilon_{11}^T}{2cl}\,(\varphi_1 + \varphi_2 - 2\varphi_3)(x - l).
\end{aligned}
\tag{5.14}
$$

The piezoelectric displacement components u, v can be obtained by integrating the strain components

$$
s_1 = \frac{\partial u}{\partial x}\,, \quad s_2 = \frac{\partial v}{\partial y}\,, \quad s_6 = \frac{\partial v}{\partial x} + \frac{\partial u}{\partial y}\,.
$$

Integrating both sides of the first two equations of (5.13) with respect to x and y respectively, we obtain

$$
\begin{aligned}
u &= \frac{3q}{4c^3}\left[\left(\tfrac{2}{3}s_{11}^E - \tfrac{1}{3}s_{12}^E + \frac{1d_{11}^2}{4\varepsilon_{11}^T}\right)xy^3 + \left(\frac{3d_{11}^2}{4\varepsilon_{11}^T} - \tfrac{1}{3}s_{11}^E x\right)x^3y + \right.\\
&\quad \left. + \frac{3d_{11}^2}{4\varepsilon_{11}^T}\,lx^2y\right] + \left[\frac{3q}{4c^3}\left(l^2s_{11}^E - \tfrac{2}{5}c^2s_{11}^E + c^2s_{12}^E - \right.\right.\\
&\quad \left.\left. - \frac{5d_{11}^2}{4\varepsilon_{11}^T}\,l^2 - \frac{c^2d_{11}^2}{4\varepsilon_{11}^T}\right) - \frac{d_{11}}{2lc}\,(\varphi_1 + \varphi_2 - 2\varphi_3)\right] xy - \\
&\quad - \frac{1}{2}\left[s_{12}^E q + \frac{d_{11}}{l}\,(\varphi_1 - \varphi_2)\right] x + F_1(y),\\
v &= \frac{3q}{16c^3}\left[\left(\tfrac{2}{3}s_{12}^E - \tfrac{1}{3}s_{11}^E - \frac{d_{11}^2}{4\varepsilon_{11}^T}\right)y^4 - \left(\frac{9d_{11}^2}{2\varepsilon_{11}^T} + 2s_{12}^E\right)x^2y^2 - \right.\\
&\quad \left. - 3\,\frac{d_{11}^2}{\varepsilon_{11}^T}\,lxy^2\right] + \left[\frac{3q}{8c^3}\left(l^2s_{12}^E - \tfrac{3}{5}c^2s_{12}^E + c^2s_{11}^E + \right.\right.\\
&\quad \left.\left. + \frac{5d_{11}^2}{4\varepsilon_{11}^T}\,l^2 + \frac{c^2d_{11}^2}{4\varepsilon_{11}^T}\right) + \frac{d_{11}}{4cl}\,(\varphi_1 + \varphi_2 - 2\varphi_3)\right] y^2 - \\
&\quad - \frac{1}{2}\left[s_{11}^E q - \frac{d_{11}}{l}\,(\varphi_1 - \varphi_2)\right] y + F_2(x),
\end{aligned}
\tag{5.15}
$$

which, when substituted in the last equation of (5.13), yield

$$\frac{dF_2}{dx} + \frac{dF_1}{dy} = \frac{3q}{4c^3}\left(\tfrac{1}{3} s^E_{11} - \frac{9d^2_{11}}{4\varepsilon^T_{11}}\right)x^3 - \frac{27qd^2_{11}}{16c^3\varepsilon^T_{11}} lx^2 +$$
$$+ \left[\frac{3q}{4c^3}\left(c^2 s^E_{12} - l^2 s^E_{11} - \tfrac{8}{5} c^2 s^E_{11} + \frac{15l^2 d^2_{11}}{4\varepsilon^T_{11}} + \frac{3c^2 d^2_{11}}{4\varepsilon^T_{11}}\right) + \right.$$
$$\left. + \frac{3d_{11}}{2cl}(\varphi_1 + \varphi_2 - 2\varphi_3)\right] x +$$
$$+ \frac{27qd^2_{11}}{16c^3\varepsilon^T_{11}} ly^2 + \frac{3qd^2_{11}}{8c^3\varepsilon^T_{11}} l(l^2 - c^2) - \frac{d_{11}}{c}(\varphi_1 + \varphi_2 - 2\varphi_3).$$

The above equation is satisfied by taking

$$\frac{dF_2}{dx} = \frac{3q}{4c^3}\left(\tfrac{1}{3} s^E_{11} - \frac{9d^2_{11}}{4\varepsilon^T_{11}}\right)x^3 - \frac{27qd^2_{11}}{16c^3\varepsilon^T_{11}} lx^2 +$$
$$+ \left[\frac{3q}{4c^3}\left(c^2 s^E_{12} - l^2 s^E_{11} - \tfrac{8}{5} c^2 s^E_{11} + \frac{15l^2 d^2_{11}}{4\varepsilon^T_{11}} + \frac{3c^2 d^2_{11}}{4\varepsilon^T_{11}}\right) + \right.$$
$$\left. + \frac{3d_{11}}{2cl}(\varphi_1 + \varphi_2 - 2\varphi_3)\right] x + b_1,$$

$$\frac{dF_1}{dy} = \frac{27qd^2_{11}}{16c^3\varepsilon^T_{11}} ly^2 + a_1$$

where

$$a_1 + b_1 = \frac{3qd^2_{11}}{8c^3\varepsilon^T_{11}} l(l^2 - c^2) - \frac{d_{11}}{c}(\varphi_1 + \varphi_2 - 2\varphi_3).$$

Hence

$$F_1(y) = \frac{9qd^2_{11}}{16c^3\varepsilon^T_{11}} ly^3 + a_1 y + a_2,$$

$$F_2(x) = \frac{3q}{16c^3}\left(\tfrac{1}{3} s^E_{11} - \frac{9d^2_{11}}{4\varepsilon^T_{11}}\right)x^4 - \frac{9qd^2_{11}}{16c^3\varepsilon^T_{11}} lx^3 +$$
$$+ \left[\frac{3q}{8c^3}\left(c^2 s^E_{12} - l^2 s^E_{11} - \tfrac{8}{5} c^2 s^E_{11} + \frac{15l^2 d^2_{11}}{4\varepsilon^T_{11}} + \frac{3c^2 d^2_{11}}{4\varepsilon^T_{11}}\right) + \right.$$
$$\left. + \frac{3d_{11}}{4lc}(\varphi_1 + \varphi_2 - 2\varphi_3)\right] x^2 + b_1 x + b_2.$$

At the centroid of the middle cross-section ($x = 0$, $y = 0$) the horizontal displacement u is zero and the vertical displacement v is equal to the deflection b_2. If we assume that the deflection is zero at the ends $x = \pm l$ of the central line $y = 0$, we must have

$$
\begin{aligned}
a_2 &= 0, \quad b_1 = \frac{9qd_{11}^2}{16c^3\varepsilon_{11}^T} l^3, \\
a_1 &= -\frac{3qd_{11}^2}{8c^3\varepsilon_{11}^T} l(\tfrac{1}{2}l^2 + c^2) - \frac{d_{11}}{c}(\varphi_1 + \varphi_2 - 2\varphi_3), \\
b_2 &= -\frac{3q}{16c^3}\left(\tfrac{1}{3}s_{11}^E - \frac{9d_{11}^2}{4\varepsilon_{11}^T}\right) l^4 - \left[\frac{3q}{8c^3}\left(c^2 s_{12}^E - l^2 s_{11}^E - \tfrac{8}{5}c^2 s_{11}^E + \right.\right. \\
&\qquad \left.\left. + \frac{15l^2 d_{11}^2}{4\varepsilon_{11}^T} + \frac{3c^2 d_{11}^2}{\varepsilon_{11}^T}\right) + \frac{3d_{11}}{4cl}(\varphi_1 + \varphi_2 - 2\varphi_3)\right] l^2.
\end{aligned}
$$

Thus finally

$$
\begin{aligned}
u = \frac{3q}{4c^3}&\left[\left(\tfrac{2}{3}s_{11}^E - \tfrac{1}{3}s_{12}^E + \frac{d_{11}^2}{4\varepsilon_{11}^T}\right) xy^3 + \right. \\
&\left. + \left(\frac{3d_{11}^2}{4\varepsilon_{11}^T} - \tfrac{1}{3}s_{11}^E\right) x^3 y + \frac{3d_{11}^2}{4\varepsilon_{11}^T} l x^2 y\right] + \\
&+ \left[\frac{3q}{4c^3}\left(l^2 s_{11}^E - \tfrac{2}{5}c^2 s_{11}^E + c^2 s_{12}^E - \frac{5l^2 d_{11}^2}{4\varepsilon_{11}^T} - \frac{c^2 d_{11}^2}{4\varepsilon_{11}^T}\right) - \right. \\
&\left. - \frac{d_{11}}{2cl}(\varphi_1 + \varphi_2 - 2\varphi_3)\right] xy - \frac{1}{2}\left[s_{12}^E q + \frac{d_{11}}{l}(\varphi_1 - \varphi_2)\right] x + \\
&+ \frac{9qd_{11}^2}{16c^3\varepsilon_{11}^T} l y^3 - \left[\frac{3qd_{11}^2}{8c^3\varepsilon_{11}^T} l(\tfrac{1}{2}l^2 + c^2) + \frac{d_{11}}{c}(\varphi_1 + \varphi_2 - 2\varphi_3)\right] y,
\end{aligned}
\tag{5.16}
$$

$$
\begin{aligned}
v = \frac{3q}{16c^3}&\left[\left(\tfrac{2}{3}s_{12}^E - \tfrac{1}{3}s_{11}^E - \frac{d_{11}^2}{4\varepsilon_{11}^T}\right) y^4 - \left(\frac{9d_{11}^2}{2\varepsilon_{11}^T} + 2s_{12}^E\right) x^2 y^2 - 3\frac{d_{11}^2}{\varepsilon_{11}^T} l x y^2\right] + \\
&+ \left[\frac{3q}{8c^3}\left(l^2 s_{12}^E - \tfrac{2}{5}c^2 s_{12}^E + c^2 s_{11}^E + \frac{5l^2 d_{11}^2}{4\varepsilon_{11}^T} + \frac{c^2 d_{11}^2}{4\varepsilon_{11}^T}\right) + \right. \\
&\left. + \frac{d_{11}}{4cl}(\varphi_1 + \varphi_2 - 2\varphi_3)\right] y^2 - \frac{1}{2}\left[s_{11}^E q - \frac{d_{11}}{l}(\varphi_1 - \varphi_2)\right] y + \\
&+ \frac{3q}{16c^3}\left(\tfrac{1}{3}s_{11}^E - \frac{9d_{11}^2}{4\varepsilon_{11}^T}\right)(x^4 - l^4) - \frac{9qd_{11}^2}{16c^3\varepsilon_{11}^T} l x^3 + \\
&+ \left[\frac{3q}{8c^3}\left(c^2 s_{12}^E - l^2 s_{11}^E - \tfrac{8}{5}c^2 s_{11}^E + \frac{15l^2 d_{11}^2}{4\varepsilon_{11}^T} + \frac{3c^2 d_{11}^2}{4\varepsilon_{11}^T}\right) + \right. \\
&\left. + \frac{3d_{11}}{4lc}(\varphi_1 + \varphi_2 - 2\varphi_3)\right](x^2 - l^2) + \frac{9qd_{11}^2}{16c^3\varepsilon_{11}^T} l^3 x.
\end{aligned}
$$

It is seen from (5.13) and (5.16) that the piezoelectric effect modifies all the three strain components and the two displacement components. The electric field components E_1, E_2 and the electric displacement components D_1, D_2 are all present in this case.

For the non-piezoelectric isotropic case

$$d_{11} = 0, \quad s_{11}^{E} = \frac{1}{E}, \quad s_{12}^{E} = -\frac{\sigma}{E},$$

and the displacement components take the known values 5)

$$u = \frac{3q}{4c^3E}\left[(l^2x - \tfrac{1}{3}x^3)y + x(\tfrac{2}{3}y^3 - \tfrac{2}{5}c^2y) + \sigma x(\tfrac{1}{3}y^3 - c^2y + \tfrac{2}{3}c^3)\right],$$

$$v = -\frac{3q}{4c^3E}\left\{\tfrac{1}{12}y^4 - \tfrac{1}{2}c^2y^2 + \tfrac{2}{3}c^2y + \sigma[(l^2 - x^2)\tfrac{1}{2}y^2 + \tfrac{1}{6}y^4 - \tfrac{1}{5}c^2y^2]\right\} -$$

$$- \frac{3q}{4c^3E}\left[\tfrac{1}{2}l^2x^2 - \tfrac{1}{12}x^4 - \tfrac{1}{5}c^2x^2 + (1 + \tfrac{1}{2}\sigma)c^2x^2\right] +$$

$$+ \frac{15ql^4}{48c^3E}\left[1 + \frac{12c^2}{5l^2}(\tfrac{4}{5} + \tfrac{1}{2}\sigma)\right].$$

Acknowledgment. I wish to express my sincere thanks to Dr. G. Paria for his valuable help in the preparation of this paper.

Received 27th May, 1961.

REFERENCES

1) Cady, W. G., Piezoelectricity. McGraw-Hill Book Co. Inc., New York 1946.
2) Mason, W. P., Piezoelectric crystals and their application to Ultrasonics, D. Van Nostrand Co. Inc., New York 1950.
3) Paria, G., J. Sci. Engng. Res. Kharagpur **4** (1960) 386.
4) Jerrad, R. P., Quart. Appl. Math. **18** (1960) 173.
5) Timoshenko, S. and J. N. Goodier, Theory of Elasticity McGraw-Hill Book Co. Inc. (Asian Students' Edition) 1951, p. 35–43.
6) Standard on Piezoelectric crystals, Proc. Instn. Radio Engrs. **37** (1949) 1378.

Appl. sci. Res. Section B, Vol. **9**

LAMINAR FLOW IN CHANNELS WITH POROUS WALLS IN THE PRESENCE OF A TRANSVERSE MAGNETIC FIELD

by U. SURYAPRAKASARAO

Department of Applied Mathematics, Indian Institute of Technology, Kharagpur, India

Summary

The steady two dimensional laminar flow of a viscous incompressible and electrically conducting fluid through a channel of rectangular cross-section in the presence of a transverse magnetic field is discussed when the fluid is being withdrawn through both the walls of the channel at the same rate. It is assumed that the suction Reynolds number and the magnetic Reynolds number are both small. Approximate expressions for the velocity components and pressure are obtained. It is found that the pressure drop in the major flow direction decreases with the increase in suction and increases with the increase in the strength of the magnetic field. Also, the skin friction decreases with the increase in the suction or the magnetic field.

§ 1. *Introduction.* The steady two-dimensional flow of a viscous incompressible fluid through a channel of rectangular cross-section has been discussed by Berman [1]) and Yuan [2]) when the fluid is being withdrawn through the channel walls at the same rate. Whereas Berman has studied this problem for small values of suction Reynolds number, Yuan has discussed it for large values. In this paper we are discussing the steady two-dimensional laminar flow of a viscous incompressible and electrically conducting fluid through a channel of rectangular cross section in the presence of a transverse magnetic field. The problem is treated for small values of suction Reynolds number, neglecting the induced magnetic field produced by the motion of the electrically conducting fluid.

§ 2. *Basic equations.* Let us consider a channel of rectangular cross-section one side of which, representing the distance between the porous walls, is much smaller than the other. Let the y axis be perpendicular to the channel walls and the x axis be in a plane parallel to the channel walls with the origin at the centre of the channel. Let L be the length of the channel and $2h$ the distance between the walls. The components of velocity in the x and y directions are represented by u and v. A constant magnetic field of strength H_0 is applied perpendicular to the walls and fixed relative to them.

The equation of continuity is

$$\frac{\partial u}{\partial x} + \frac{\partial v}{\partial y} = 0. \tag{1}$$

The equations of momentum are

$$\rho\left(u\frac{\partial u}{\partial x} + v\frac{\partial u}{\partial y}\right) = -\frac{\partial p}{\partial x} + \mu\left(\frac{\partial^2 u}{\partial x^2} + \frac{\partial^2 u}{\partial y^2}\right) - \sigma_e B_0{}^2 u, \tag{2}$$

$$\rho\left(u\frac{\partial v}{\partial x} + v\frac{\partial v}{\partial y}\right) = -\frac{\partial p}{\partial y} + \mu\left(\frac{\partial^2 v}{\partial x^2} + \frac{\partial^2 v}{\partial y^2}\right), \tag{3}$$

where ρ is the density of the fluid, μ the coefficient of viscosity, p the pressure, σ_e the electrical conductivity, $B_0 = \mu_e H_0 =$ the electromagnetic induction, μ_e being the magnetic permeability. In (2) and (3), the secondary effects of magnetic induction are ignored [3]). Also, we shall assume that the electric field is zero; this assumption is justified since no external electric field is applied and the effect of polarisation of the ionized fluid is negligible [4]). In view of these assumptions Maxwell's equations become superfluous.

Introducing $\lambda = y/h$, the equations (1)–(3) become

$$\frac{\partial u}{\partial x} + \frac{1}{h}\frac{\partial v}{\partial \lambda} = 0, \tag{4}$$

$$u\frac{\partial u}{\partial x} + \frac{v}{h}\frac{\partial u}{\partial \lambda} = -\frac{1}{\rho}\frac{\partial p}{\partial x} + \nu\left(\frac{\partial^2 u}{\partial x^2} + \frac{1}{h^2}\frac{\partial^2 u}{\partial \lambda^2}\right) - \frac{\sigma_e B_0{}^2 u}{\rho}, \tag{5}$$

$$u\frac{\partial v}{\partial x} + \frac{v}{h}\frac{\partial v}{\partial \lambda} = -\frac{1}{h\rho}\frac{\partial p}{\partial \lambda} + \nu\left(\frac{\partial^2 v}{\partial x^2} + \frac{1}{h^2}\frac{\partial^2 v}{\partial \lambda^2}\right), \tag{6}$$

where ν is the kinematic viscosity.

The boundary conditions on u and v are

$$u(x, \pm 1) = 0, \tag{7}$$

$$v(x, \pm 1) = \pm v_0, \tag{8}$$

where v_0 is the velocity of suction at the walls of the channel.

It is evident that a stream function ψ satisfying (4) exists such that

$$u(x, \lambda) = \frac{1}{h}\frac{\partial \psi}{\partial \lambda}, \tag{9}$$

$$v(x, \lambda) = -\frac{\partial \psi}{\partial x}. \tag{10}$$

Following Berman, we shall choose the stream function as

$$\psi(x, \lambda) = (h\bar{u}_0 - v_0 x)\, f(\lambda). \tag{11}$$

Then the velocity components (9) and (10) are given by

$$u = \left(\bar{u}_0 - v_0 \frac{x}{h}\right) f'(\lambda), \tag{12}$$

$$v = v_0 f(\lambda), \tag{13}$$

where $\bar{u}_0$ is the average axial component of velocity at $x = 0$, and is given by

$$\bar{u}_0 = \int_0^1 u(0, \lambda)\, d\lambda. \tag{14}$$

It may be noted here that $f(\lambda)$ is an arbitrary function of λ. Since the fluid is being withdrawn at constant rate from both the walls, v is independent of x. The dashes in (12) and future discussion denote differentiation with respect to λ.

Substituting (12) and (13) in (5) and (6) we get

$$-\frac{1}{\rho}\frac{\partial p}{\partial x} = \left(\bar{u}_0 - v_0 \frac{x}{h}\right)\left[\frac{v_0}{h}(ff'' - f'^2) - \frac{\nu}{h^2} f''' + \frac{\sigma_e B_0^2}{\rho} f'\right], \tag{15}$$

$$-\frac{1}{h\rho}\frac{\partial p}{\partial \lambda} = \frac{v_0^2}{h} ff' - \frac{\nu v_0}{h^2} f''. \tag{16}$$

Differentiating (16) with respect to x, we get

$$\frac{\partial^2 p}{\partial x \partial \lambda} = 0. \tag{17}$$

Differentiating (15) with respect to λ and using (17) we get

$$\left(\bar{u}_0 - v_0 \frac{x}{h}\right) \frac{\mathrm{d}}{\mathrm{d}\lambda} \left[\frac{v_0}{h}(ff'' - f'^2) - \frac{\nu}{h^2} f''' + \frac{\sigma_e B_0^2}{\rho} f'\right] = 0. \tag{18}$$

Since (18) must be satisfied for all values of x, we have

$$\frac{\mathrm{d}}{\mathrm{d}\lambda} \left[\frac{v_0}{h}(ff'' - f'^2) - \frac{\nu}{h^2} f''' + \frac{\sigma_e B_0^2}{\rho} f'\right] = 0. \tag{19}$$

Let us define the dimensionless numbers

R = suction Reynolds number = hv_0/ν,
R_M = magnetic Reynolds number = $\mu_e \sigma_e h v_0$,
P_M = magnetic pressure number = $\mu_e H_0^2/\rho v_0^2$.

Integrating (19) and re-arranging the terms we get

$$f''' + R(f'^2 - ff'' - af') = K, \tag{20}$$

where K is an arbitrary constant, and $a = P_M R_M$. The boundary conditions on $f(\lambda)$ are

$$f(\pm 1) = \pm 1, \; f'(\pm 1) = 0. \tag{21}$$

The exact solution of the equations of motion and continuity is given by the third-order non-linear differential equation (20), subject to the boundary conditions (21).

§ 3. *Perturbation solution.* We shall assume that the suction Reynolds number R is small. Following Berman, let us assume that

$$\left.\begin{aligned} f(\lambda) &= f_0(\lambda) + Rf_1(\lambda) + R^2 f_2(\lambda) + \dots, \\ K &= K_0 + K_1 R + K_2 R^2 + \dots, \end{aligned}\right\} \tag{22}$$

where the f_n's and K_n's are independent of R. Substituting (22) in (20) and equating the same powers of R, we get

$$f_0''' = K_0, \tag{23}$$

$$f_1''' + f_0'^2 - f_0 f_0'' - af_0' = K_1, \tag{24}$$

$$f_2''' + 2f_0' f_1' - f_0 f_1'' - f_0'' f_1 - af_1' = K_2, \tag{25}$$

and so on. The boundary conditions on $f_n(\lambda)$ are given by

$$\left.\begin{aligned} f_0(\pm 1) = \pm 1, \; f_n(\pm 1) = 0 \text{ for } n \geq 1 \\ f_n'(\pm 1) = 0 \text{ for all } n. \end{aligned}\right\} \tag{26}$$

The solutions of (23) and (24) subject to (26) are

$$f_0(\lambda) = \tfrac{1}{2}\lambda(3 - \lambda^2), \tag{27}$$

$$f_1(\lambda) = \tfrac{1}{280}(3\lambda^3 - 2\lambda - \lambda^7) + \frac{a}{40}(2\lambda^3 - \lambda - \lambda^5). \tag{28}$$

It is also found that

$$K_0 = -3, K_1 = \tfrac{81}{35} - \tfrac{6}{5}a. \tag{29}$$

Hence the first-order perturbation solution for $f(\lambda)$ and K is

$$f^{(1)}(\lambda) = \tfrac{1}{2}\lambda(3 - \lambda^2) + \frac{R}{280}(3\lambda^3 - 2\lambda - \lambda^7) + \\ + \frac{aR}{40}(2\lambda^3 - \lambda - \lambda^5), \tag{30}$$

$$K^{(1)} = -3 + \left(\tfrac{81}{35} - \frac{6a}{5}\right)R. \tag{31}$$

Since the coefficient of R in (31) is large, a second-order perturbation calculation is done and it is found that K_2 varies with a as shown in table I.

TABLE I

a	0 or 9	1 or 8	2 or 7	3 or 6	4 or 5	10
K_2	−0.017	−0.063	−0.097	−0.12	−0.13	0.04

Hence the first-order expressions for the velocity components are

$$u(x, \lambda) = \left(\bar{u}_0 - v_0\frac{x}{h}\right)\tfrac{3}{2}(1 - \lambda^2)\left[1 - \frac{R}{420}(2 - 7\lambda^2 - 7\lambda^4) + \\ + \frac{aR}{60}(1 - 5\lambda^2)\right], \tag{32}$$

$$v(\lambda) = v_0\left[\tfrac{1}{2}\lambda(3 - \lambda^2) + \frac{R}{280}(3\lambda^3 - 2\lambda - \lambda^7) + \\ + \frac{aR}{40}(2\lambda^3 - \lambda - \lambda^5)\right]. \tag{33}$$

It is evident from (28) that f_1 is an odd function of λ, and hence the symmetry of the flow about the x axis is not disturbed due to the presence of the magnetic field. It may also be noted that these results are the same as those of Berman when $a = 0$.

Multiplying both sides of (15) by $(-h^2/\nu)$ and using (20), we get

$$\frac{\partial p}{\partial x} = \frac{K\mu}{h^2}\left(\bar{u}_0 - v_0\frac{x}{h}\right). \tag{34}$$

Also we have from (16)

$$\frac{\partial p}{\partial \lambda} = \frac{\mu v_0}{h} f'' - \rho v_0{}^2 f f'. \tag{35}$$

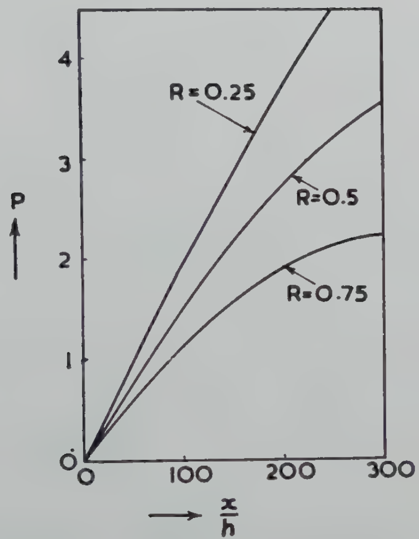

Fig. 1. Pressure drop in channels with rectangular cross-section, parameter R.

Integrating (34) and (35), we get

$$p(x, \lambda) = p(0, 0) - \tfrac{1}{2}\rho v_0{}^2 f^2(\lambda) + \frac{K\mu}{h^2}\left(x\bar{u}_0 - \frac{v_0 x^2}{2h}\right) + \\ + \frac{\mu v_0}{h}[f'(\lambda) - f'(0)]. \tag{36}$$

Using the first-order results for $f(\lambda)$ and its derivative, we can easily find the pressure distribution. The pressure drop in the major flow direction is given by

$$p(0, \lambda) - p(x, \lambda) = \frac{K\mu}{h^2}\left(\frac{v_0 x^2}{2h} - x\bar{u}_0\right). \tag{37}$$

Let us now define the entrance Reynolds number Re by

$$Re = \frac{4h\bar{u}_0}{\nu}.$$

Hence using the first order results for K, the pressure drop in the major flow direction in the dimensionless form is

$$P = \frac{p(0,\lambda) - p(x,\lambda)}{\frac{1}{2}\rho\bar{u}_0{}^2} = \frac{x}{hR_e}\left(1 - \frac{2xR}{hR_e}\right)(24 - \tfrac{648}{35}R + \tfrac{48}{5}aR). \tag{38}$$

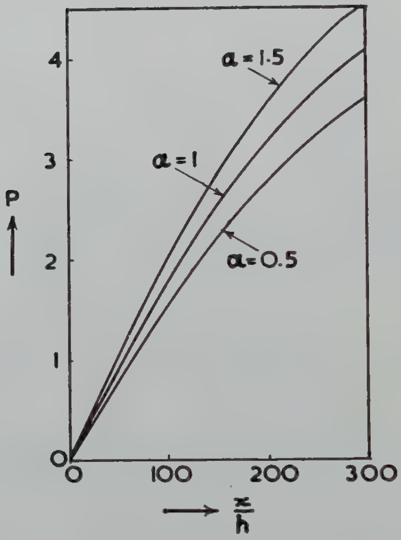

Fig. 2. Pressure drop in channels with rectangular cross-section parameter *a*.

The variation of pressure drop P with R is shown in fig. 1 for $Re = 1000$ and $a = 0.5$; and the variation of pressure drop P with a is shown in fig. 2 for $Re = 1000$ and $R = 0.5$.

The skin friction at the wall $\lambda = -1$ is given by

$$\begin{aligned}\tau_w &= \left[\mu\left(\frac{\partial v}{\partial x} + \frac{\partial u}{\partial y}\right)\right]_{y=-h} = \frac{\mu}{h}\left(\frac{\partial u}{\partial \lambda}\right)_{\lambda=-1} \\ &= \frac{3\mu}{h}\left(\bar{u}_0 - v_0\frac{x}{h}\right)\left(1 + \frac{R}{35} - \frac{aR}{15}\right).\end{aligned} \tag{39}$$

Hence the skin friction in dimensionless form is given by

$$\bar{\tau}_w = \frac{\tau_w}{\frac{1}{2}\rho\bar{u}_0^2} = \frac{24}{R_e}\left(1 - \frac{4R}{R_e}\,\frac{x}{h}\right)\left(1 + \frac{R}{35} - \frac{aR}{15}\right). \qquad (40)$$

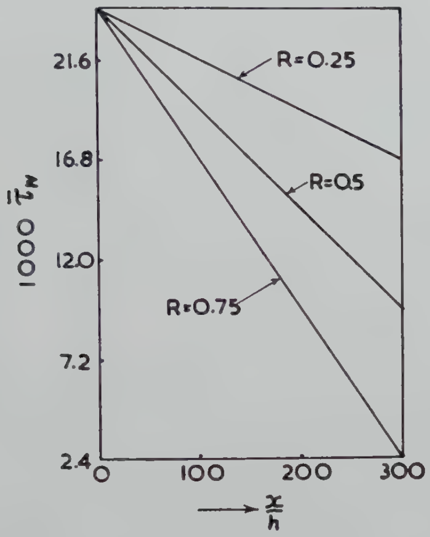

Fig. 3. Skin friction in channels with rectangular cross-section, parameter R.

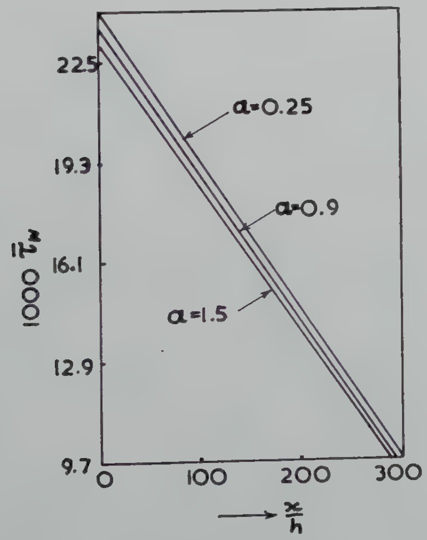

Fig. 3. Skin friction in channels with rectangular cross-section, parameter *a*.

The variation of skin friction with R is shown in fig. 3 for $Re = 1000$, $a = 3/7$; and its variation with the magnetic field is shown in fig. 4 for $Re = 1000$, $R = 0.5$.

Acknowledgement. I thank Dr. A. S. Gupta for suggesting this problem and for his help in the preparation of this paper. I am extremely grateful to Prof. B. R. Seth and Dr. G. Bandyopadhyay for their encouragement.

Received 4th April, 1961.

REFERENCES

1) Berman, A. S., J. Appl. Phys. **24** (1953) 1232.
2) Yuan, S. W., J. Appl. Phys. **27** (1956) 267.
3) Rossow, V. J., NACA Report TN 3971, 1957.
4) Meyer, R. C., J. Aero Space Sci. **25** (1958) 661.

Appl. sci. Res. Section B, Vol. 9

TWO-DIMENSIONAL FLOW OF CONDUCTING LIQUID PAST A MAGNETIZED CIRCULAR CYLINDER

by G. POWER and ANNE TUNBRIDGE

Department of Mathematics The University, Nottingham, England

Summary

The steady two-dimensional flow of an inviscid incompressible conducting fluid past a fixed circular cylinder of arbitrary conductivity is here considered when a dipole is assumed at the centre of the cross-section of the cylinder. Various approximate results are obtained which are independent of the conductivity of the cylinder, provided that this conductivity is finite. The case of infinite conductivity is also briefly discussed.

§ 1. *Introduction.* Recently a great deal of attention has been devoted to the study of the effects of a magnetic field on the flow of conducting fluid past a fixed finite body. Usually the magnetic field is applied externally, but it is also of interest to consider cases in which the field originates in the body, and in 1960 Ludford and Murray 1) discussed the steady flow of an infinite inviscid incompressible fluid past a sphere of arbitrary conductivity with a dipole situated at its centre.

We here consider the corresponding two-dimensional problem in which an inviscid incompressible fluid flows steadily past a fixed infinite circular cylinder again of arbitrary conductivity. A general distribution is first considered, and a fair approximation is obtained when a two-dimensional dipole is situated at the centre of the cylinder.

Results are found to be independent of the conductivity of the cylinder, provided that this conductivity is not infinite. For infinite conductivity, the field is permanently fixed in the cylinder, and results for this case are somewhat different.

§ 2. *Equations of motion.* The fundamental equations governing the steady flow of an infinite inviscid incompressible conducting fluid in the presence of a magnetic field are in the usual notation:

$$\nabla\cdot\boldsymbol{v}' = 0, \tag{1a}$$

$$(\nabla\times\boldsymbol{v}')\times\boldsymbol{v}' = -\nabla(p'/\rho_0 + \tfrac{1}{2}v'^2) + \mu/\rho_0(\nabla\times\boldsymbol{H}')\times\boldsymbol{H}', \tag{1b}$$

$$\boldsymbol{J} = \nabla\times\boldsymbol{H}' = \sigma(\boldsymbol{E} + \mu\boldsymbol{v}'\times\boldsymbol{H}'), \tag{1c}$$

$$\nabla\times\boldsymbol{E} = 0, \tag{1d}$$

$$\nabla\cdot\boldsymbol{H}' = 0. \tag{1e}$$

where $\boldsymbol{v}'$, $\boldsymbol{H}'$, $\boldsymbol{J}$, $\boldsymbol{E}$, p' represent respectively the fluid velocity, magnetic intensity, current density, electric and pressure fields. The fluid density ρ_0, the permeability μ and conductivity σ are assumed constant.

For our two-dimensional problem (1*c*) shows that the electric intensity $\boldsymbol{E}$ has only one component which is perpendicular to the plane of flow. From (1*d*) it follows that this component is constant, and (1*c*) at infinity immediately shows that this constant is zero.

For flow past a circular cylinder of radius a, we now refer the above equations to a dimensionless system of coordinates defined by

$$\boldsymbol{v} = \boldsymbol{v}'/u,\ \boldsymbol{H} = \boldsymbol{H}'/h,\ r = r'/a,\ p = p'/\rho_0 u^2$$

where u is the velocity of the fluid at infinity, h a representative magnetic intensity, and r' is distance measured from the centre of the circular cross-section. For the dipole case, we take $h = M/a^2$, where M is the moment of the dipole.

Equations (1) now become

$$\nabla\cdot\boldsymbol{v} = 0, \tag{2a}$$

$$(\nabla\times\boldsymbol{v})\times\boldsymbol{v} = -\nabla P + s(\nabla\times\boldsymbol{H})\times\boldsymbol{H}, \tag{2b}$$

$$\nabla\times\boldsymbol{H} = R_M\boldsymbol{v}\times\boldsymbol{H}, \tag{2c}$$

$$\nabla\cdot\boldsymbol{H} = 0, \tag{2d}$$

with $P = p + \frac{1}{2}v^2$, $s = \mu h^2/\rho_0 u^2$ the pressure number, $R_M = ua\mu\sigma$ the Reynolds magnetic number. We note that if there is no magnetic field $s = 0$.

Using the well-known circle theorem we have

$$\boldsymbol{v} = \boldsymbol{v}_0 = \left[\left(1 - \frac{1}{r^2}\right)\cos\theta, -\left(1 + \frac{1}{r^2}\right)\sin\theta\right], \tag{3}$$

which gives the uniform stream $[\cos\theta, -\sin\theta]$ at infinity. We can now expand in powers of s for weak magnetic fields in the form

$$\boldsymbol{v} = \boldsymbol{v}_0 + s\boldsymbol{v}_1 + \dots, \boldsymbol{H} = \boldsymbol{H}_0 + s\boldsymbol{H}_1 + \dots, p = p_0 + sp_1 + \dots.$$

From equations (2*c*) and (2*d*) $\boldsymbol{H}_0$ satisfies

$$\nabla \times \boldsymbol{H}_0 = R_M(\boldsymbol{v}_0 \times \boldsymbol{H}_0), \tag{4b}$$

$$\nabla \cdot \boldsymbol{H}_0 = 0, \tag{4b}$$

and from (2*a*) and (2*b*) $\boldsymbol{v}_1$, p_1 satisfy

$$(\nabla \times \boldsymbol{v}_1) \times \boldsymbol{v}_0 = -\nabla P_1 + (\nabla \times \boldsymbol{H}_0) \times \boldsymbol{H}_0, \tag{5a}$$

$$\nabla \cdot \boldsymbol{v}_1 = 0, \tag{5b}$$

where $P_1 = p_1 + \boldsymbol{v}_0 \cdot \boldsymbol{v}_1$, $\boldsymbol{v}_0$ being given by (3).

At each stage in the approximations the terms in p and $\boldsymbol{v}$ are evaluated before that in $\boldsymbol{H}$. It is, however, sufficient for our present problem to restrict calculations to $\boldsymbol{H}_0$, $\boldsymbol{v}_1$ and p_1.

§ 3. *Calculation of* $\boldsymbol{H}_0$. If $\boldsymbol{H}_0 = [H_r, H_\theta]$, then (4*a*) and (4*b*) are satisfied by

$$H_r = \frac{1}{r}\frac{\partial F}{\partial \theta}, \quad H_\theta = -\frac{\partial F}{\partial r}, \tag{6}$$

where F is given by

$$\frac{\partial^2 F}{\partial r^2} + \frac{1}{r}\frac{\partial F}{\partial r} + \frac{1}{r^2}\frac{\partial^2 F}{\partial \theta^2} = \\ = R_M\left[\left(1 - \frac{1}{r^2}\right)\cos\theta\frac{\partial F}{\partial r} - \left(1 + \frac{1}{r^2}\right)\frac{\sin\theta}{r}\frac{\partial F}{\partial \theta}\right]. \tag{7}$$

Now assume that $F = \exp[-\frac{1}{2}\alpha(1 - \cos\theta)]\, f$, where $\alpha = rR_M$, chosen so that perturbation expansion remains regular on $\theta = 0$ and finite at infinity. Thus f satisfies the equation

$$\frac{\partial^2 f}{\partial \alpha^2} + \frac{1}{\alpha}\frac{\partial f}{\partial \alpha} + \frac{1}{\alpha^2}\frac{\partial^2 f}{\partial \theta^2} - \frac{\partial f}{\partial \alpha} - \frac{f}{2\alpha} = \\ = -R_M{}^2\left[\frac{\cos\theta}{\alpha^2}\frac{\partial f}{\partial \alpha} + \frac{\sin\theta}{\alpha^3}\frac{\partial f}{\partial \theta} + \frac{(\cos 2\theta - \cos\theta)\, f}{2\alpha^2}\right] \tag{8}$$

When $R_M = 0$, (8) has the product type-solutions

$$f = e^{\frac{1}{2}\alpha} K_n(\alpha/2) \sin n\theta, \tag{9}$$

with the usual notation ,K_n representing a Bessel function.

A suitable approximation can now be made by taking a combination of the solutions $n = 1, 2$. Thus we take

$$f = AR_M\left(\frac{1}{2} + \frac{1}{\alpha}\right)\sin\theta + BR_M{}^3\left(\frac{1}{\alpha^2} + \frac{1}{2\alpha} + \frac{1}{16}\right)\sin 2\theta, \tag{10}$$

with A, B constants, yielding

$$F = \exp\left[-\frac{R_M}{2}\, r(1-\cos\theta)\right]\left[\frac{A\sin\theta}{r} + \right.$$
$$\left. + R_M\left(\frac{A\sin\theta}{2} + \frac{B\sin 2\theta}{r^2}\right)\right], \tag{11}$$

correct to $O(R_M{}^2)$. Substitution of F, as given by equation (11), into the differential equation (7) verifies that this is the correct order of approximation. These results of course hold for the region outside the cylinder.

Again, inside the cylinder, $\boldsymbol{E}=0$ and $\nabla\times\boldsymbol{H}$ and $\nabla\cdot\boldsymbol{H}$ are both zero. Hence inside we may take

$$F = \frac{\sin\theta}{r} + Cr\sin\theta + R_M D r^2 \sin 2\theta, \tag{12}$$

the first term being due to the dipole and the other terms representing the regular irrotational disturbance field with C, D constants yet to be determined.

We now find the constants A, B, C, D so that the boundary conditions on the cylinder are satisfied to $O(R_M{}^2)$. The continuity of the tangential component of $\boldsymbol{H}_0$ requires

$$A = 1 - C,\ B = -D,$$

and the continuity of the normal component of magnetic induction requires

$$\mu A = \mu'(1 + C),\ \mu(2B + \tfrac{1}{2}A) = 2\mu' D,$$

where μ' is the permeability of the cylinder, and thus

$$A = \frac{2\mu'}{\mu + \mu'},\ -B = D = \frac{\mu\mu'}{2(\mu+\mu')^2},\ C = \frac{\mu - \mu'}{\mu + \mu'}. \tag{13}$$

From (6), (11) the components of the magnetic field are given by

$$\begin{aligned} H_r &= \exp\left[-\frac{R_M}{2}r(1-\cos\theta)\right]\left\{\frac{A}{r^2}(1+\tfrac{1}{2}R_M r)\cos\theta + \right. \\ &\qquad\qquad \left. + \frac{R_M}{r^3}(2B\cos 2\theta - \tfrac{1}{2}Ar^2\sin {}^2\theta)\right\}, \\ H_\theta &= \exp\left[-\frac{R_M}{2}r(1-\cos\theta)\right]\left\{\frac{A}{r^2}(1+\tfrac{1}{2}R_M r)\sin\theta \right. \\ &\qquad\qquad \left. + \frac{R_M}{r^3}(2B - \tfrac{1}{4}Ar^2)\sin 2\theta\right\}, \end{aligned} \tag{14}$$

with A, B given by (13).

§ 4. *Vorticity and velocity*. The vorticity vector $\nabla\times\boldsymbol{v}_1$ is perpendicular to the plane of flow and hence has only one component of magnitude ω, say. From (5*a*) ω satisfies

$$\omega\left(1+\frac{1}{r^2}\right)\sin\theta = -\frac{\partial P_1}{\partial r} + G_r$$

and (15)

$$\omega\left(1-\frac{1}{r^2}\right)\cos\theta = -\frac{1}{r}\frac{\partial P_1}{\partial\theta} + G_\theta,$$

where

$$\boldsymbol{G} = [G_r, G_\theta] = (\nabla\times\boldsymbol{H}_0)\times\boldsymbol{H}_0 = R_M(\boldsymbol{v}_0\times\boldsymbol{H}_0)\times\boldsymbol{H}_0,$$

so that, correct to $O(R_M{}^3)$,

$$\begin{aligned} G_r &= \exp[-R_M r\,(1-\cos\theta)]\left\{-\frac{2A^2}{r^4}R_M(1+R_M r)\sin^2\theta\cos\theta\right. \\ &+ \frac{AR_M{}^2}{r^7}\sin^2\theta\left[2B(r^2[1-8\cos^2\theta]+1) + \right. \\ &\qquad \left.\left. + A\left(\frac{1}{2}r^4+\frac{1}{2}r^2+r^4\cos^2\theta - r^2\cos^2\theta\right)\right]\right\}, \end{aligned} \tag{16}$$

$$\begin{aligned} G_\theta &= \exp[-R_M r(1-\cos\theta)]\left\{\frac{2A^2}{r^4}R_M(1+R_M r)\sin\theta\cos^2\theta + \right. \\ &\qquad + \frac{AR_M{}^2}{r^7}\sin\theta\cos\theta\left[2B(r^2[8\cos^2\theta-3]-1) + \right. \\ &\qquad\qquad \left.\left. + A\left(-\frac{1}{2}r^4+\frac{1}{2}r^2 - r^4\sin^2\theta - r^2\sin^2\theta\right)\right]\right\}. \end{aligned}$$

Eliminating P_1 from (15), we get

$$\left(r-\frac{1}{r}\right)\cos\theta\,\frac{\partial\omega}{\partial r}-\left(1+\frac{1}{r^2}\right)\sin\theta\,\frac{\partial\omega}{\partial\theta}=g(r,\theta), \tag{17}$$

where

$$g(r,\theta)=\frac{\partial}{\partial r}(rG_\theta)-\frac{\partial G_r}{\partial\theta}, \tag{18}$$

with G_r, G_θ given by (16) above. If

$$v_r=-\frac{1}{r}\frac{\partial\psi}{\partial\theta},\quad v_\theta=\frac{\partial\psi}{\partial r}, \tag{19}$$

where ψ is the stream function, then ψ satisfies

$$\frac{\partial^2\psi}{\partial r^2}+\frac{1}{r}\frac{\partial\psi}{\partial r}+\frac{1}{r^2}\frac{\partial^2\psi}{\partial\theta^2}=\omega. \tag{20}$$

Now when $\omega=0$, (20) has the product-type solutions

$$\psi=(A_nr^n+B_nr^{-n})\sin n\theta.$$

It therefore appears reasonable to expand ω in the form

$$\omega=\sum_{n=1}^{\infty}\omega_n(r)\sin n\theta \tag{21}$$

and correspondingly

$$g(r,\theta)=\sum_{n=1}^{\infty}g_n(r)\sin n\theta. \tag{22}$$

The substitution of (21), (22) into (17) yields the recurrence relation

$$\left(r-\frac{1}{r}\right)\omega'_{n+1}(r)+(n+1)\left(1+\frac{1}{r^2}\right)\omega_{n+1}(r)$$
$$+\left(r-\frac{1}{r}\right)\omega'_{n-1}(r)-(n-1)\left(1+\frac{1}{r^2}\right)\omega_{n-1}(r)=2g_n(r),$$

which in its integrated form becomes

$$\left(\frac{r^2-1}{r}\right)^{n+1}\omega_{n+1}(r)=\int_1^r\left(\frac{\rho^2-1}{\rho}\right)^n\left[2g_n(\rho)-\left(\rho-\frac{1}{\rho}\right)\omega'_{n-1}(\rho)+\right.$$
$$\left.+(n-1)\left(1+\frac{1}{\rho^2}\right)\omega_{n-1}(\rho)\right]d\rho,$$

the lower limit of integration being due to the requirement that ω_n should not be infinite when $r = 1$. When $n = 1$,

$$\omega_2(r) = \left(\frac{r}{r^2 - 1}\right)^2 \int_1^r \frac{2(\rho^2 - 1)}{\rho} g_1(\rho)\, d\rho. \tag{23}$$

The terms g_n may be evaluated from (18), (22), and $\omega_4, \omega_6, \ldots$ follow successively. Again ω_1 must be chosen before $\omega_3, \omega_5, \ldots$ can be found. These must be such that the complete series (21) tends to zero at infinitely large distances upstream. However, for the present problem it is sufficient to know ω_2.

The stream function is expanded as

$$\psi = \sum_{n=1}^{\infty} \psi_n(r) \sin n\theta \tag{24}$$

and substituting (24), (21) in (20), we obtain

$$\psi_n''(r) + \frac{1}{r}\psi_n'(r) - \frac{n^2}{r^2}\psi_n(r) = \omega_n(r).$$

Solutions of this equation vanishing on $r = 1$ are

$$\psi_n(r) = \frac{1}{2n}\int_1^r \left(\frac{r^n}{\beta^{n-1}} - \frac{\beta^{n+1}}{r^n}\right) \omega_n(\beta)\, d\beta + A_n\left(r^n - \frac{1}{r^n}\right),$$

with

$$A_n = \frac{-1}{2n}\int_1^{\infty} \frac{\omega_n(\beta)}{\beta^{n-1}}\, d\beta,$$

chosen so that $\psi_n(r)$ remains finite at infinite distances.

Once the ψ_n have been determined, the velocity field follows from (19), and in particular

$$v_\theta = \sum_n^{\infty} v_n(r) \sin n\theta,\ v_n(r) = \psi'_n(r).$$

For the drag (see § 5) the only requirement is

$$v_2(1) = 4A_2 = -\int_1^{\infty} \frac{\omega_2(\beta)}{\beta}\, d\beta$$

$$= -\int_1^\infty \frac{\beta}{(\beta^2-1)^2}\left(\int_1^\beta \frac{2(\rho^2-1)}{\rho}\, g_1(\rho)\, d\rho\right) d\beta$$

$$= -\int_1^\infty \frac{g_1(\beta)}{\beta}\, d\beta. \tag{25}$$

§ 5. *The drag.* The force exerted on the cylinder is made up of two parts, the first due to the fluid pressure and the other due to the Maxwell stress.

We assume that G_θ, G_r may be expanded as

$$G_\theta = \sum_{n=1}^\infty n a_n(r) \sin n\theta, \quad G_r = \sum_{n=1}^\infty b_n(r) \cos n\theta. \tag{26}$$

Thus from (15)

$$P_1 = p_1 + \boldsymbol{v}_0 \cdot \boldsymbol{v}_1 = -\sum_{n=0}^\infty a_n(1) \cos n\theta,$$

where $a_0(1)$ is an undetermined constant of integration.

The total drag due to the pressure is $\rho_0 u^2 a D_p$ where

$$D_p = -s\int_0^{2\pi} p_1 \cos\theta\, d\theta = \pi s[a_1(1) - v_2(1)].$$

From (18) we see that

$$g_n(r) = n[a_n(r) + b_n(r) + r a_n'(r)],$$

and hence (25) becomes

$$v_2(1) = -\int_1^\infty \frac{[a_1(\beta) + b_1(\beta)]}{\beta}\, d\beta + a_1(1),$$

so that

$$D_p = \pi s \int_1^\infty \frac{[a_1(\beta) + b_1(\beta)]}{\beta}\, d\beta. \tag{27}$$

For a dipole, from (26)

$$a_1(r) + b_1(r) = \frac{1}{\pi}\int_0^{2\pi} (G_\theta \sin\theta + G_r \cos\theta)\, d\theta,$$

where from (16)

$$G_\theta \sin\theta + G_r \cos\theta = \frac{AR_M{}^2}{r^7} \cos\theta \sin^2\theta\, (Ar^4 \cos 2\theta - 4Br^2),$$

setting $R_M = 0$ in the exponential, since this leads only to an error of $O(R_M{}^3)$. Hence $a_1(r) + b_1(r) = 0$ to this order, so that

$$D_p = sO(R_M{}^3).$$

The drag due to the Maxwell stress $\mu H_i H_j - \frac{1}{2}\mu H^2 \delta_{ij}$ on a surface element of the cylinder has components

$$\mu h^2[\tfrac{1}{2}(H_r{}^2 - H_\theta{}^2),\, H_r H_\theta].$$

The total contribution is a force $\rho_0 u^2 a D_M$ with

$$D_M = s\int_0^{2\pi} [\tfrac{1}{2}(H_r{}^2 - H_\theta{}^2)\cos\theta - H_r H_\theta \sin\theta]\, d\theta. \tag{28}$$

For a dipole the square bracket in the above integral is

$$\begin{aligned} &\tfrac{1}{2}A^2(1 + R_M)(1 - 4\sin^2\theta)\cos\theta + 2ABR_M(1 - 8\cos^2\theta \sin{}^2\theta) - \\ &-\tfrac{1}{2}A^2R_M(1 - \cos\theta)(1 - 4\sin^2\theta)\cos\theta + \tfrac{1}{2}A^2R_M \sin{}^2\theta + \\ &\qquad\qquad\qquad\qquad\qquad\qquad\qquad + O(R_M{}^2). \end{aligned}$$

On integrating (28) we get

$$D_M = \frac{\pi A^2 s R_M}{2} = \frac{2\pi\mu'^2 s R_M}{(\mu + \mu')^2}, \tag{29}$$

and this expression gives therefore the drag coefficient to the first order in R_M.

§ 6. *Perfectly conducting cylinder.* The previous results hold for a cylinder of arbitrary finite conductivity, but when the conductivity is infinite, the magnetic field is frozen into the cylinder. For a dipole using solutions corresponding to $n = 1, 2$ as in § 3

$$F = \exp\left[-\frac{R_M r}{2}(1 - \cos\theta)\right]\left\{\frac{\mu'}{\mu}\left[\frac{\sin\theta}{r} + R_M\left(\frac{\sin\theta}{2} - \frac{\sin^2\theta}{4r^2}\right)\right]\right\}. \tag{30}$$

On the cylinder, $F = (\mu'/\mu)\sin\theta$ to the order R_M, so that the normal component of magnetic induction has the same value as that for the dipole frozen into the sphere. There is no requirement on the tangential component.

Results can immediately be obtained from our previous work by noting that (39) can be obtained from (11) by setting

$$A = -4B = \mu'/\mu.$$

As before the total drag is $\rho_0 u^2 a D_M$ where from (29)

$$D_M = \frac{\pi}{2}\left(\frac{\mu'}{\mu}\right)^2 sR_M.$$

From this it is seen that when a cylinder of high conductivity is considered perfectly conducting the drag is in error by a factor $4\mu^2/(\mu + \mu')^2$.

We finally remark that all results may be obtained, perhaps more easily, by expanding in terms of R_M instead of s. Both methods of expansion can still be used even when the dipole is inclined at a general angle to the field, the procedure, although more complicated, being virtually the same.

Since submitting this article, the authors have found similar results published elsewhere 2).

Received 12th May, 1961.

REFERENCES

1) Ludford, G. S. and J. D. Murray, J. Fluid Mech. **7** (1960) 516.
2) Murray, J. D. and L. Chi, Mathematika **7** (1960) 64.

FILED IN STACKS